TU Delft

Delft University of Technology

Statistical analysis of the relation between metallic microstructures and mechanical properties

Vittorietti, Martina

DOI
10.4233/uuid:6d5208ff-9f95-4a93-9ccf-d85ee0145cd4

Publication date
2020

Document Version
Final published version

Citation (APA)
Vittorietti, M. (2020). *Statistical analysis of the relation between metallic microstructures and mechanical properties*. [Dissertation (TU Delft), Delft University of Technology]. https://doi.org/10.4233/uuid:6d5208ff-9f95-4a93-9ccf-d85ee0145cd4

Important note
To cite this publication, please use the final published version (if applicable).
Please check the document version above.

Copyright
Other than for strictly personal use, it is not permitted to download, forward or distribute the text or part of it, without the consent of the author(s) and/or copyright holder(s), unless the work is under an open content license such as Creative Commons.

Takedown policy
Please contact us and provide details if you believe this document breaches copyrights.
We will remove access to the work immediately and investigate your claim.

This work is downloaded from Delft University of Technology.
For technical reasons the number of authors shown on this cover page is limited to a maximum of 10.

STATISTICAL ANALYSIS OF THE RELATION BETWEEN METALLIC MICROSTRUCTURES AND MECHANICAL PROPERTIES

STATISTICAL ANALYSIS OF THE RELATION BETWEEN METALLIC MICROSTRUCTURES AND MECHANICAL PROPERTIES

Dissertation

for the purpose of obtaining the degree of doctor
at Delft University of Technology
by the authority of the Rector Magnificus,
prof. dr. ir. T.H.J.J. van der Hagen,
chair of the Board for Doctorates
to be defended publicly on
Friday 17, July 2020 at 15:00 o'clock

by

Martina VITTORIETTI

Master of Science in Statistics
Università degli Studi di Palermo, Palermo, Italy,
born in Palermo, Italy.

This dissertation has been approved by the promotors

Composition of the doctoral committee:

Rector Magnificus,	chairperson
Prof. dr. ir. G. Jongbloed,	Delft University of Technology, promotor
Prof. dr. ir. J. Sietsma,	Delft University of Technology, promotor
Independent members:	
Prof. dr. ir. L. Kestens	Ghent University
Prof. dr. F.H.J. Redig	Delft University of Technology
Dr. V Robins	Australian National University
Dr. A.J. Cabo	Delft University of Technology
Dr. P.J.J. Kok	Tata Steel



Keywords: statistics, metal microstructures, mechanical properties, digital twin, isotonic regression, hypothesis testing, ssimulations

Printed by: GVO drukkers & vormgevers B.V.

Front & Back: Martina Vittorietti

ISBN 978-94-6332-642-1

An electronic version of this dissertation is available at
http://repository.tudelft.nl/.

Look up at the stars and not down at your feet.
Try to make sense of what you see,
and wonder about what makes the universe exist.
Be curious.

Stephen Hawking

CONTENTS

Preface ix

List of Figures xi

List of Tables xvii

1 Introduction 1

I MIC 9

2 3D Poisson-Voronoi Diagrams 11
2.1 Introduction . . . 12
2.2 Basic concepts . . . 13
2.3 Distribution of the geometrical characteristics . . . 15
2.4 Non-parametric approach . . . 17
2.5 Parametric approach . . . 21
2.6 Application . . . 25
2.7 Conclusions . . . 27

3 Poisson-Voronoi hypothesis testing 29
3.1 Introduction . . . 30
3.2 Basic concepts . . . 31
3.3 Distribution of the geometrical characteristics . . . 32
3.4 Model tests . . . 35
3.5 Quantiles of the model tests . . . 42
3.6 Power of the model tests . . . 49
3.7 Application . . . 51
3.8 Conclusions . . . 58

4 Digital Material Representation 61
4.1 Introduction . . . 62
4.2 Representative Volume Element . . . 65
4.3 Statistically Similar Representative Volume Element . . . 68
4.3.1 Multi-Level Voronoi tessellation . . . 68
4.4 Conclusions . . . 75

II MEC 77

5 Mechanical property investigation from 2D images 79
5.1 Introduction . . . 80
5.2 Isotonic Regression . . . 81

5.3 Estimating restricted means in the normal case . . . 82
5.4 Likelihood Ratio Test: constant μ against monotonicity . . . 85
5.5 Bootstrap approach . . . 89
5.6 Application . . . 91
5.7 Conclusions . . . 93

6 3D Virtual Experiments **95**
6.1 Introduction . . . 96
6.2 Virtual Tensile Test . . . 97
6.3 Stress–Strain Diagram . . . 101
6.4 Segmented approach . . . 104
6.5 Functional Data Analysis . . . 109
6.6 Conclusions . . . 114

7 Conclusions **119**

A Appendix **123**

B Appendix **127**

Bibliography **131**

Summary **143**

Samenvatting **145**

Acknowledgements **147**

Curriculum Vitæ **151**

List of Publications **153**

PREFACE

The present thesis is written under the project MICtoMEC: Extensive quantification of microstructure features and statistical relations with mechanical behaviour –from statistical relations to physical understanding–.
This research was carried out under project number S41.5.14547b in the framework of the Partnership Program of the Materials innovation institute M2i (www.m2i.nl) and the Technology Foundation TTW (www.stw.nl), which is part of the Netherlands Organization for Scientific Research (www.nwo.nl).
The project was initiated with the idea of bringing together material scientists and mathematicians to closely work on the structure-properties relation problem for metals.
I was appointed for facing the mathematical/statistical side of the problem and, though I found the project particularly interesting, my knowledge about materials and especially metals was quite poor.
During my research, the collaboration with materials scientists and with people from industry such as Tata Steel, was fundamental for broadening my knowledge in this field.
At the same time, the variety of data and statistical problems that one can encounter studying materials allowed me to move into different statistical areas. From topics closely related to geometry and topology, to regression models and functional approaches, I always tried to find a way for solving problems with advanced tools but that can still be easily understandable and reproducible.
I do not know if it is better to develop knowledge vertically or horizontally, but I definitely learned much more than I expected.
This project deepened my knowledge in both fields, but I still remain loyal to my first love: Statistics.
This thesis is, in fact, written by a statistician's perspective and it addresses statisticians and material scientists. I describe problems and methodologies in a language that is understandable for both audiences and so my apologies, if some concepts or definitions can be redundant for one of the two fields.
It was fascinating to find out that Statistics can help to solve several Materials Science problems and at the same time Materials Science problems can give rise to challenging Statistical questions.

Martina Vittorietti
Delft, March 2020

LIST OF FIGURES

1.1 (a) Single-phase steel microstructure (b) AISI stainless steel with $M_{23}C_6$ carbides precipitation (c) Multi-phase steel microstructure 2
1.2 Images at different macroscopic plastic strains for the same region of AIS 420 steel (a) 0% strain (b) 3.5% strain (c) 6.6% strain (d) 13.9% strain (scale 5μm) 5

2.1 (a) Kernel density estimate (Epanechnikov kernel, cross validation bandwidth $h = 0.05$) and (b) empirical cumulative distribution function of volume of 1 000 000 Poisson-Voronoi typical cells, $\lambda = 1$ 18
2.2 (a) Kernel density estimate (Epanechnikov kernel, cross validation bandwidth $h = 0.25$) and (b) empirical cumulative distribution function of surface area of 1 000 000 Poisson-Voronoi typical cells, $\lambda = 1$ 19
2.3 (a) Relative frequencies and (b) empirical cumulative distribution function of number of faces of 1 000 000 Poisson-Voronoi typical cells, $\lambda = 1$ 19
2.4 Comparison of parametric approximations to the volume distribution of 1 000 000 Poisson-Voronoi typical cells, $\lambda = 1$ 23
2.5 (a) QQplot and (b) cumulative distribution function comparison of parametric approximations to the volume distribution of 1 000 000 Poisson-Voronoi typical cells, $\lambda = 1$ 23
2.6 Comparison of parametric approximations to the surface area distribution of 1 000 000 Poisson-Voronoi typical cells, $\lambda = 1$ 24
2.7 (a) QQplot and (b) cumulative distribution function comparison of parametric approximations to the surface area of 1 000 000 Poisson-Voronoi typical cells, $\lambda = 1$ 24
2.8 Kernel density estimate (Epanechnikov kernel, cross validation bandwidth $h = 21735.28$) 25
2.9 Comparison of parametric approximations to the real volume distribution (Epanechnikov kernel, cross validation bandwidth $h = 0.057$, black line), $\lambda = 1$ 26
2.10 (a) QQplot and (b) cumulative distribution function comparison of Generalized Gamma distribution to the real volume distribution, $\lambda = 1$ 26
2.11 Cumulative distribution function comparison of Generalized Gamma distribution to the highest values of volume distribution $\lambda = 1$ 27

3.1 (a) Boundary corrected Kernel density estimate (Epanechnikov kernel, linear combination correction, $h = 0.2$ [67]) and (b) empirical cumulative distribution function of the area of 36 480 600 (originating from the 1 000 000 slices with periodic boundary conditions) 2D sectional cells, $\lambda = 1$ 34

3.2 (a) Boundary corrected Kernel density estimate (Epanechnikov kernel, linear combination correction, $h = 0.1$ [67]) and (b) empirical cumulative distribution function of the perimeter of 36 480 600 (originating from the 1 000 000 slices with periodic boundary conditions) 2D sectional cells, $\lambda = 1$ 34
3.3 (a) Relative frequencies and (b) empirical cumulative distribution function of the number of edges of 36 480 600 (originating from the 1 000 000 slices with periodic boundary conditions) 2D sectional cells, $\lambda = 1$ 35
3.4 (a) Boundary corrected Kernel density estimate (Epanechnikov kernel, linear combination correction, $h = 0.1$ [67]) and (b) empirical cumulative distribution function of the area of 500 000 (originating from the 10 000 slices with non periodic boundary conditions) 2D sectional cells, $\lambda = 0.2$ 36
3.5 (a) Boundary corrected Kernel density estimate (Epanechnikov kernel, linear combination correction, $h = 0.1$ [67]) and (b) empirical cumulative distribution function of the perimeter of 500 000 (originating from the 10 000 slices with non periodic boundary conditions) 2D sectional cells, $\lambda = 0.2$. 36
3.6 (a) Relative frequencies and (b) empirical cumulative distribution function of the number of 500 000 (originating from the 10 000 slices with non periodic boundary conditions) 2D sectional cells, $\lambda = 0.2$ 37
3.7 (a) Set of points $\mathbf{X}$ (b) Voronoi Diagram (dashed) and Delaunay Triangulation (solid) (c) Circles with radius 0.47 around the points of $\mathbf{X}$; the Alpha complex $\alpha_r(\mathbf{X})$ consists of the individual points of $\mathbf{X}$ and the one edge corresponding to the two touching circles (d) Alpha complex for $r = 1.32$ (e) Alpha complex, $r = 1.35$ (f) Alpha complex, $r = 1.66$ (g) Alpha complex, $r = 2.76$ (h) Alpha complex, $r = 3.61$ (i) Alpha complex, $r = 3.68$ 41
3.8 Persistence Diagram. The black dots indicate the birth- and death time of connected components and the red triangles the birth- and death times of the holes. The data are the same as those used for Figure 3.7. 42
3.9 Rank function for connected components (a) and holes (b) Persistence Landscapes for connected components (c) and holes (d) 43
3.10 Monte Carlo approximation of $P(N_{2D} = 50|N_{3D} = k)$ 45
3.11 Cumulative distribution function of the coefficient of variation of the 2D sectional cells area conditioned on $N_{2D} = 50$ (black line; green dotted lines are obtained using the upper and lower limit of the confidence set for $\hat{\lambda} = 0.2$) and unconditioned (red line) 46
3.12 Cumulative distribution function of the 2D sectional cells area conditioned on $N_{2D} = 50$ (black line; green dotted lines are obtained using the upper and lower limit of the confidence set for $\hat{\lambda} = 0.2$) and unconditioned (red line) 47
3.13 Cumulative distribution function of the empirical CDF test of the 2D sectional cells area conditioned on $N_{2D} = 50$ (black line; green dotted lines are obtained using the upper and lower limit of the confidence set for $\hat{\lambda} = 0.2$) and unconditioned (red line) 47
3.14 k Weighted mean landscapes (connected components) for sections with exactly 50 2D sectional cells, ($\hat{\lambda} = 0.2$) 48

3.15 k Weighted mean landscapes (holes) for sections with exactly 50 2D sectional cells, ($\hat{\lambda} = 0.2$) 48
3.16 Max weighted mean landscape (connected components) for sections with exactly 50 2D sectional cells (black line; green dotted lines are obtained using the upper and lower limit of the confidence set for $\hat{\lambda} = 0.2$) 49
3.17 Max weighted mean landscape (holes) for sections with exactly 50 2D sectional cells (black line; green dotted lines are obtained using the upper and lower limit of the confidence set for $\hat{\lambda} = 0.2$) 49
3.18 Cumulative distribution function of the test based on the L_2 distance between persistence landscapes L_0, (3.4.6), of the 2D sectional cells area conditioned on $N_{2D} = 50$ (black line; green dotted lines are obtained using the upper and lower limit of the confidence set for $\hat{\lambda} = 0.2$) and unconditioned (red line) 50
3.19 Cumulative distribution function of the test based on the L_2 distance between persistence landscapes L_1, (3.4.6), of the 2D sectional cells area conditioned on $N_{2D} = 50$ (black line; green dotted lines are obtained using the upper and lower limit of the confidence set for $\hat{\lambda} = 0.2$) and unconditioned (red line) 50
3.20 (a) 2D Poisson-Voronoi diagram (b) 2D Sectional Poisson-Voronoi Diagram, $N_{2D} = 50$ 51
3.21 Histograms of the results of the coefficient of variation test (a), of the empirical CDF test (b), of the test based on the L_2 distance between persistence landscape L_0 (c) and L_1 (d) for 7000 2D Poisson-Voronoi diagram. Red dotted lines identify the quantile of the conditional distribution of the test for $N_{2D} = 50$ 52
3.22 Schemes as planar tessellations of plane sections of alumina ceramics: preprocessing (a) Hahn&Lorz ([50]), (b) Cut of the plane sections with exactly 50 cells 53
3.23 Cumulative distribution function comparison of the cells area of the schemes of plane sections of alumina ceramics (Fig.3.22 1 (a) black line, 2 (a) yellow line, 3 (a) green line) and of the 2D Sectional Poisson-Voronoi cells area (red line) 54
3.24 From left to right centers of mass of the schemes of plane sections of alumina ceramics (Fig.3.22 1 (a), 2 (a), 3 (a)) 54
3.25 From left to right persistence diagrams of the centres of mass of the schemes of plane sections of alumina ceramics (Fig.3.22 1 (a), 2 (a), 3 (a)) 55
3.26 From left to right persistence landscapes (connected components) of the schemes of plane sections of alumina ceramics (Fig.3.22 1 (a), 2 (a), 3 (a)) 55
3.27 From left to right persistence landscapes (holes) of the schemes of plane sections of alumina ceramics (Fig.3.22 1 (a), 2 (a), 3 (a)) 55
3.28 Cumulative distribution function comparison of the cuts of the sections of alumina ceramics with exactly 50 cells (Fig.3.22 1(b) black line, 2(b) yellow line, 3(b) green line) and of the 2D Sectional Poisson-Voronoi cells area conditioned on $N_{2D} = 50$ (red line) 56

3.29 From left to right centres of mass of the cuts of the sections of alumina ceramics with exactly 50 cells (Fig.3.22 1 (b), 2 (b), 3 (b)) 56

3.30 From left to right persistence diagrams of the centers of mass of the cuts of the sections of alumina ceramics with exactly 50 cells (Fig.3.22 1 (b), 2 (b), 3 (b)) 57

3.31 From left to right persistence landscapes (connected components) of the cuts of the sections of alumina ceramics with exactly 50 cells (Fig.3.22 1 (b), 2 (b), 3 (b)) 57

3.32 From left to right persistence landscapes (holes) of the cuts of the sections of alumina ceramics with exactly 50 cells (Fig.3.22 1 (b), 2 (b), 3 (b)) 57

4.1 Schematic version of methods for Digital Material Representation. The middle column indicates important aspect of the representation. The left- and right column state how these aspects are dealt with in both approaches 63

4.2 Secondary electron SEM image of $AISI420$ with $M_{23}C_6$ carbides (smaller particles) in which rolling direction (RD) and normal direction (ND) is indicated. 66

4.3 (a) EBSD phase map overlapped on image quality map in which white lines delimit ferrite grains with boundary angles higher than 10°. (b) ND inverse pole figure map for ferrite phase; black regions represent $M_{23}C_6$ carbides . 66

4.4 (a) Ferrite grain size distribution (b) Carbide size distribution 67

4.5 Two RVEs with different resolution and number of grains: (a) $50 \times 50 \times 50$ voxels, 502 ferrite grains and 174 carbides (b) $100 \times 100 \times 100$ voxels, 268 ferrite grains and 109 carbides 68

4.6 (a) 3D Multi-Level Poisson-Voronoi diagram and corresponding (b) 2D sectional Multi-Level Poisson-Voronoi diagram with $\lambda_1 = 0.3$ and $\lambda_2 = 0.1$ (c) 3D Multi-Level Poisson-Voronoi diagram and corresponding (d) 2D sectional Multi-Level Poisson-Voronoi diagram with $\lambda_1 = 3$ and $\lambda_2 = 0.1$ . . . 70

4.7 Histogram of the volume of the first level cells and of the second level grains of a 3D Multi-Level Poisson-Voronoi diagram with $\lambda_1 = 0.3$ and $\lambda_2 = 0.1$ (a)-(b) and of a 3D Multi-Level Poisson-Voronoi diagram with h $\lambda_1 = 3$ and $\lambda_2 = 0.1$(c)-(d) 71

4.8 Histogram of the surface area of the first level cells and of the second level grains of a 3D Multi-Level Poisson-Voronoi diagram with $\lambda_1 = 0.3$ and $\lambda_2 = 0.1$ (a)-(b) and of a 3D Multi-Level Poisson-Voronoi diagram with h $\lambda_1 = 3$ and $\lambda_2 = 0.1$(c)-(d) 72

4.9 Empirical Cumulative Distribution comparison between the volume distributions of 100 grains (a) and the volume distributions of the second level grains (b) of a 3D Multi-Level Poisson-Voronoi diagram with $\lambda_1 = 0.3$ and $\lambda_2 = 0.1$ (red line) of a 3D Multi-Level Poisson-Voronoi diagram with h $\lambda_1 = 3$ and $\lambda_2 = 0.1$ (black line) 73

4.10 Empirical Cumulative Distribution comparison between the area distributions of the first level cells (a) and the area distributions of the second level grains (b) of a 2D section of a 3D Multi-Level Poisson-Voronoi diagram with $\lambda_1 = 0.3$ and $\lambda_2 = 0.1$ (red line) and of a 3D Multi-Level Poisson-Voronoi diagram with h $\lambda_1 = 3$ and $\lambda_2 = 0.1$ (black line) 73
4.11 Two SSRVEs with the same number of ferrite grains (λ_2) but different carbides volume fractions (λ_1^c) generated in a volume $10\times10\times10$: (a) 3D Multi-Level Poisson Voronoi diagram and corresponding (b) 2D sectional Multi-Level Poisson Voronoi diagram with $\lambda_1 = 3$ ($\lambda_1^c = 0.03$) and $\lambda_2 = 0.5$ (c) 3D Multi-Level Poisson Voronoi diagram and corresponding (b) 2D sectional Multi-Level Poisson Voronoi diagram with $\lambda_1 = 3$ ($\lambda_1^c = 0.11$) and $\lambda_2 = 0.5$. The blue particles are cells of the first level tessellation for which a different phase (carbide) is assigned 74

5.1 Tensile testing machine 92
5.2 Microstructure image showing the KAM at strain level 13.9 % (overlapped grid of 25×25). 92
5.3 Plot of KAM and Number of carbides for the 625 squared areas of Figure 5.2 93

6.1 3D Multi-Level Poisson Voronoi diagrams with increasing level of λ_1^c: (a) $\lambda_1^c = 0$, (b) $\lambda_1^c = 0.01$, (c) $\lambda_1^c = 0.03$, (d) $\lambda_1^c = 0.05$, (e) $\lambda_1^c = 0.07$, (f) $\lambda_1^c = 0.09$, (g) $\lambda_1^c = 0.11$ 97
6.2 Experimental (hollow symbol) and simulated (red line) stress–strain obtained at constant deformation rate of 0.0001 s^{-1} 100
6.3 Stress–Strain curves. Different colours indicating different values of the intensity parameter of the carbides, different symbols indicating different textures. 101
6.4 Stress–Strain Diagram 102
6.5 Log-log plot for one stress–strain curve excluding the first linear part of the function 105
6.6 Plot of the fitted segmented function for the 70 different stress–strain curves. Different colours indicating the three different segments in Eq. (6.4.2) . . . 106
6.7 Comparison between the observed stress—strain values (black dots) and the estimated piecewise function for one of the 70 stress–strain curve. . . 107
6.8 Plot of the estimated change points, ϵ_1 (a) and ϵ_2 (b), and the observed volume fraction of carbides for the 70 different microstructures (different symbols indicating different textures). 107
6.9 Plot of the estimated model parameters and the observed volume fraction of carbides for the 70 different microstructures (different symbols indicating different textures). 108
6.10 Mean stress–strain curve for microstructure without carbides (red line). Different colours indicating different textures. 111
6.11 Stress–strain centred to the expected stress–strain for microstructure without carbides. Different colours indicating different values of the intensity parameter of the carbides, different symbols indicating different textures. 111

6.12 First two eigenfunctions obtained with the modified FPCA performed on the 70 stress–strain curves. 112
6.13 Plot of the two FPCA scores obtained for the 70 stress–strain curves. Different colours indicating different values of the intensity parameter of the carbides, different symbols indicating different textures. 112
6.14 Plot of the FPCA scores correspondent to first functional principal component ϕ_1 and the observed values of carbide intensity λ_1^c for the 70 stress–strain curves.Different colours indicating different values of the intensity parameter of the carbides, different symbols indicating different textures. 113
6.15 Observed first principal component scores, A_1, versus fitted values of linear mixed model (Eq. 6.5.6) 114
6.16 Fitted stress–strain functions using model 6.5.7. Different colours indicating different values of the intensity parameter of the carbides, different symbols indicating different textures. 115
6.17 Comparison between observed (filled circles) and fitted (empty circles) stress–strain functions. Different colours indicating different values of the intensity parameter of the carbides. 116
6.18 Effect of texture in the stress-strain curves. 116
6.19 Effect of carbides volume fraction in the stress-strain curves. Different symbols indicating different textures. 117

B.1 Estimated E parameter of the first segment of function (6.4.1) versus fitted values of a linear mixed model with random intercepts for the different textures and explanatory variable given by the observed carbide volume fraction 128
B.2 Estimated n_1 parameter parameter of the second segment of function (6.4.1) versus fitted values of a linear mixed model with random intercepts for the different textures and explanatory variable given by the observed carbide volume fraction 128
B.3 Estimated n_2 parameter of the third segment of function (6.4.1) versus fitted values of a linear mixed model with random intercepts for the different textures and explanatory variable given by the observed carbide volume fraction 129

LIST OF TABLES

2.1 Estimated moments of the geometrical features of 1 000 000 Poisson-Voronoi typical cells, λ=1 . . . 18
2.2 Distribution of the number of faces (F) of 1 000 000 Poisson-Voronoi typical cell, $\lambda = 1$ . . . 20
2.3 Estimated Generalized Gamma parameters for volume distribution approximation, $\lambda = 1$ . . . 22
2.4 Estimated Generalized Gamma parameters for surface area distribution approximation, $\lambda = 1$ . . . 22
2.5 Comparison of Gamma-, Generalized Gamma- and Lognormal approximations for volume distribution in terms of Supremum- and Total Variation distance . . . 23
2.6 Comparison of Gamma-, Generalized Gamma- and Lognormal approximations for surface area distribution in terms of Supremum- and Total Variation distance . . . 23

3.1 Estimated moments of the geometrical features of 36 480 600 2D sectional cells, $\lambda = 1$ . . . 33
3.2 Estimated moments of the geometrical features of 500 000 (originating from the 10 000 slices with non periodic boundary conditions) 2D sectional cells, $\lambda = 0.2$ . . . 37
3.3 Quantiles of the conditional distribution of the coefficient of variation of the 2D sectional cells area given that $N_{2D} = 50$, ($\lambda = 0.2$) . . . 45
3.4 Quantiles of the conditional distribution of the test based on the difference between cumulative distribution functions of the 2D sectional cells area given that $N_{2D} = 50$, ($\hat{\lambda} = 0.2$) . . . 48
3.5 Quantiles of the conditional distribution of the test based on the difference between the observed landscapes and the conditional mean landscapes (connected components) of the 2D sectional cells area given that $N_{2D} = 50$, ($\hat{\lambda} = 0.2$) . . . 48
3.6 Quantiles of the conditional distribution of the test based on the difference between the observed landscapes and the conditional mean landscapes (holes) of the 2D sectional cells area given that $N_{2D} = 50$, ($\hat{\lambda} = 0.2$) . . . 49
3.7 Values of the different model tests for the schemes of plane sections of alumina ceramics (Fig.3.22 1 (a), 2 (a), 3 (a)) . . . 58
3.8 Values of the different model tests for the cuts of the sections of alumina ceramics with exactly 50 cells (Fig.3.22 1 (b), 2 (b), 3 (b)) . . . 58

4.1 Estimated moments of the geometrical features of 1000 grains obtained by EBSD measurements 67

5.1 Values of estimated means and variances of the KAM conditioned on the number of carbides visible in a square of a grid 25×25 according to different order restrictions assumptions (13.9% Strain) 94
5.2 Estimated values for the four different likelihood ratio test with the corresponding parametric and non-parametric p-values 94

6.1 Materials parameter for DAMASK model implementation 99
6.2 Estimated values of the parameters of the linear mixed model 113

B.1 Estimated values of the parameters of the linear mixed model 127

1

INTRODUCTION

During the production of metallic alloys there are various procedures one can employ for enhancing the quality of the final product. Cooling, heating, bending, stressing, quenching for different durations and at different intensity levels are examples of the processes that can influence the nature of the material. Variations in brittleness, ductility, elasticity, hardness, plasticity, tensile strength, in general in the chemical, physical and mechanical properties of the materials, are the visible modifications that the processing causes. In fact, the treatments cause not immediately visible modifications that occur in a microstructural, nanostuctural and even in an atomic level. These structural modifications cause the changes in properties.

The great interest in steel derives mainly from the possibility of generating, by solid-state transformations during processing, a huge variety of microstructures [13] with different mechanical behaviour.

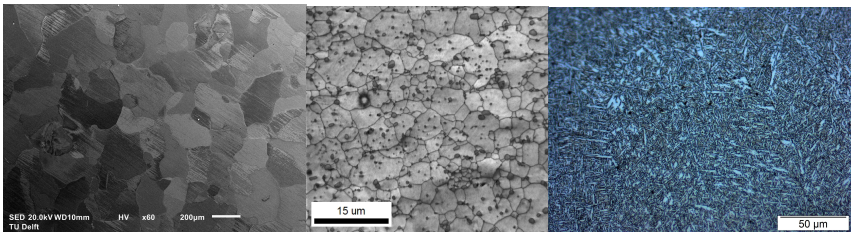
The concept of microstructure is not easily definable and it depends on the specific observational scale. Starting from the atomic scale, metals can be described as a regular aggregation of atoms held together by "metallic bonds" [132]. The atoms form a symmetrical three-dimensional aggregation, characterised by a unit cell. Unit cells in which atoms are identically packed form a crystal, also called grain, of a specific phase. Metallic microstructures usually contain more than one crystal, of one or multiple phases, with a specific orientation and possible imperfections or defects.

Loosely speaking, one can say that the microstructure forms the DNA of the material and hence contains all the necessary information determining the properties of the metals. Ideally, we would like to genetically modify the DNA of the material to obtain a product with the desired properties. More specifically, we would like to fully control and tune different microstructural parameters, one at the time, pairwise or jointly, perform various experiments and see what the macro effect on the performance of the material is.

In reality, the impossibility of controlling different factors individually, makes the quantitative identification of the relation between microstructural features and mechanical properties very hard.

The study of the relation between microstructural features and mechanical properties

presents different problems that can be tackled or partially tackled with the help of physics, stereology, geometry, computer science and also statistics.
One of the main problems regards the data.
Several techniques have been developed to obtain microstructure data. Methods for obtaining 3D microstructure images are rapidly arising, but time and costs make data not easily accessible yet. The most common way of gathering microstructural information is analysing 2D images taken using suitable tools such as optical microscopes or electron microscopes.
This means that an intrinsically three-dimensional object is reduced to a two-dimensional plane. This 'one-step-back' is the subject of stereological studies [18].
This issue can also be viewed as a statistical problem, considering that the 2D picture must be a representative sample of the 3D microstructure.
Choices of scale and dimension are then crucial for obtaining an accurate representation of the material microstructure.
In fact, the aim is to gather in one 2D image all the characteristic features of the microstructure and then relate them to the original 3D structure.
Information about phases, morphology (arrangement, size, orientation, defects), chemical composition of grains/crystals should be collected for appropriately quantifying microstructures. Metallic microstructures are complex objects, showing different features at different scales. Examples of different microstructures are shown in Figure 1.1. The



(a) (b) (c)

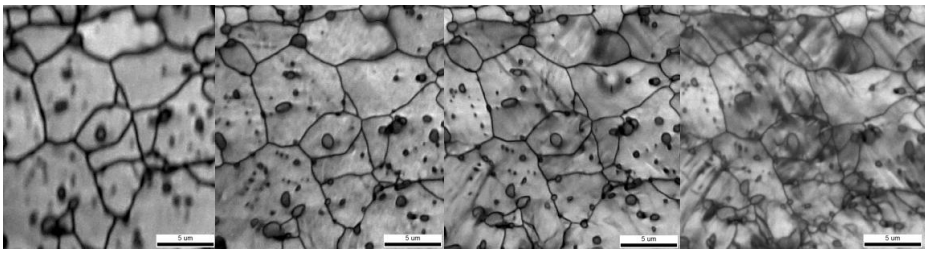
Figure 1.1: (a) Single-phase steel microstructure (b) AISI stainless steel with $M_{23}C_6$ carbides precipitation (c) Multi-phase steel microstructure

first feature about which we want to gather data is the grain.
A grain is usually defined as a single crystal with a simil-polygonal shape. But, as shown in Figure 1.1 (c), its polygonal shape is not always easily recognisable and in some cases even not present. Information on grain size (grain volume in 3D, grain area in 2D, grain surface area (3D), grain perimeter (2D), number of grain faces (3D), number of grain edges (2D), number of neighbours), grain phase, grain orientation and grain boundaries are necessary for an accurate representation of the microstructure at the scale of the grain.
As said before, a microstructure, more specifically a polycrystalline microstructure, is the arrangement of multiple grains, including possible features within the grains.
Several models and procedures have been proposed in the literature for describing grain growth and the geometrical aggregation of grains [102].

For a schematic representation, one common assumption, reasonable mainly for single-phase microstructures, is that during formation the grains start to grow at the same time in a finite volume until they reach a space-filling configuration. This assumption pertains to the relatively poorly understood nucleation process. Geometrically speaking this process can be addressed as a "tessellation of space"-process.
Voronoi tessellation constitutes one the most used and most flexible classes of models for microstructure characterisation [103].
Poisson-Voronoi diagrams are the most basic Voronoi tessellation and they have been commonly employed for representing single-phase steel microstructures [88]. Intuitively, for defining a 3D Poisson-Voronoi diagram, a random set of points (generator points or sites) is generated in a finite volume and spheres having them as centres are grown at the same time and with the same velocity; once two spheres touch, a face between them appears. This results in a space-filling configuration made of convex polyhedra, also called cells or grains.
A challenging statistical question to be answered is whether Poisson-Voronoi diagrams or a more general model for a microstructure is adequate, given measured data.
Interesting analogies can be found between the distribution of the main geometrical features of the theoretical and observed structures. But as previously stated, recovering 3D real microstructure data can be troublesome, pushing researchers to use Voronoi diagrams even in cases in which they might be inappropriate.
Therefore, recalling the 2D-3D problem, an important question to be answered is: in view of a 2D microstructure image, is the Poisson-Voronoi diagram (or another specific model) a good model for describing the intrinsically 3D microstructure?
A clear limitation of Poisson-Voronoi diagrams, and also of other tessellations based on classical point processes, is that the resulting grains are always convex. As is seen in Figure 1.1 (a) even for single-phase steel this assumption can sometimes be inadequate. Moreover, when the microstructure under study presents multiple phases (different colours in Fig. 1.1 (c)) or intermediate phases such as carbides (smaller grains with a different colour in Fig. 1.1 (b)), one must resort to modifications of the classical models or to completely different models. In fact, grains belonging to different phases present different crystal structures, that need to be modelled in a different way [31].
Extensions of the classical Voronoi model such as Johnson-Mehl Voronoi tessellations [89], Laguerre Voronoi tessellations [87], Controlled Poisson-Voronoi tessellations [165] and Multi-Level Voronoi tessellations [72, 161] are relatively flexible approaches used for modelling more complex microstructures. Also more general grain growth models such as Cellular Automata or Monte Carlo Potts models are choices frequently used in the literature [108, 114].
Also the other aspects of the microstructure, such as grain boundaries, texture (crystallographic orientations), phases and defects play an important role for an accurate representation of the microstructure. Methods such as Electron Backscatter Diffraction (EBSD) allow to measure crystallographic orientations/misorientations and phases of steel specimens. The method is based on obtaining maps of Electron Back-Scatter Patterns (EBSP) of individual crystalline regions inside grains, at a scale of typically 50nm. The EBSP is solved/indexed to find the orientation of the crystal under the beam. This results in a measurement of the phase and orientation on one specific specimen loca-

tion and the process is repeated for many points on a regular grid (either rectangular or hexagonal). The grain orientation is then usually expressed by a triplet of Euler angles (ϕ_1, Φ, ϕ_2) [116].
Characterisation of the defects is also of paramount importance. All real crystals contain imperfections that can be zero dimensional (point defects), one dimensional (line defects also called dislocations), two dimensional (interface) and three dimensional (volume defects). Many of the physical, chemical and mechanical properties of metals are strongly related to those imperfections [61].
Taking into account all these factors and the underlying relations among them, implies a great difficulty in finding a model to represent metal microstructure.
The difficulty level increases when the complex nature of microstructures has to be related to the mechanical behaviour of the material. For understanding how the different microstructural parameters relate to the mechanical performance of the material, various approaches can be followed.
A common approach is investigating the mechanical performance of the material based on statistics obtained from 2D images. Examples can clarify the general idea behind this. One of the best-known relations between microstructure features and a mechanical property is the so-called Hall-Petch relation [51, 109]. In particular, the Hall-Petch equation describes the negative dependence of yield stress[1] on grain size of the material. Loosely speaking, the smaller grains are, the stronger the material is. The classical form of the relation involves just the mean grain size as characterising feature but adding more information gathered from the 2D microstructure images, such as grain size distribution or dislocations density can lead to more accurate descriptions.
One of the most common ways for investigating strength and ductility of metallic materials is by performing a tensile test. A tensile test is an experiment in which force (stress) is applied to the test sample causing deformation of the material, temporarily (elastic behaviour), permanently (plastic behaviour) and eventually its fracture. During a tensile test, dislocations, necessary to allocate the stress applied during the experiment, form in the microstructure. Observing the 2D images taken at different levels of strain (Figure 1.2), it is indeed possible to identify features in the microstructure that are related to these line defects which contribute to the hardening of the material. Understanding which are the microstructural features that favour or obstacle the dislocations motion and formation, is then a first step for material strengthening comprehension.
Building a model based on the observation of 2D microstructure images is a good starting point for understanding the 3D mechanical behaviour of the material. However, experimental inaccuracy and the impossibility of controlling all possible changes occurring in the microstructure during the experiments, make this kind of model just a good preliminary inspection from which mainly qualitative conclusions can be drawn.
In order to manipulate and supervise the modifications that occur in the microstructure and how they affect the mechanical behaviour of the material, a fully simulation-based approach can be adopted.
It starts with the creation of a "digital twin" microstructure. The term "digital twin" was coined by [134] in NASA's integrated technology roadmap under Technology Area 11: Modelling, Simulation, Information Technology and Processing and the following defi-

[1] The yield stress is defined as the minimal stress at which the material starts to deform permanently.



(a) (b) (c) (d)

Figure 1.2: Images at different macroscopic plastic strains for the same region of AIS 420 steel (a) 0% strain (b) 3.5% strain (c) 6.6% strain (d) 13.9% strain (scale 5μm)

nition is given: "A digital twin is an integrated multi-physics, multi-scale simulation of a vehicle or system that uses the best available physical models, sensor updated, fleet history etc. to mirror the life of its corresponding flying twin". Readapting this sentence for the case under study, a statistically based digital twin metal microstructure can be defined as: "an integrated multiscale simulation of a metal microstructure that uses the best available physics-based models, scaling properties, parameters optimisation, physical relations etc. to mirror the mechanical behaviour of its corresponding steel twin". In the Materials Science field, this procedure has a specific name: "Digital Material Representation (DMR)" [88]. DMR has as main goal mimicking the morphology of the material both from the geometrical and the physical point of view, constructing a "Representative Volume Element" (RVE) or a Statistically Similar RVEs (SSRVEs). The idea behind the two structures is the same: they have to be smaller than real volume elements but sufficiently large to incorporate the relevant information about the material microstructural features and properties. The difference is in the way of constructing them. The RVE is mostly based on empirical sectioning of the materials or on finite element reconstruction from tomographic measurements and mechanical tests [19]. The SSRVE and similar constructs, such as statistically equivalent representative volume element (SERVE) [148] and statistically similar volume elements (SSVEs) [19], incorporate stereological and physical parameters in a volume, geometrically partitioned by one of the tessellation models previously discussed.

After the digital twin microstructure is ready, the virtual experiment can be performed. The Düsseldorf Advanced Material Simulation Toolkit (DAMASK) [123] is an open source freeware package developed by the Max-Planck Institute für Eisenforschung for conducting advanced microstructure-based simulations of mechanical behaviour. It uses models coming from Crystal Plasticity theory, based on the behaviour of a single crystal, which have been successfully used in understanding and predicting the evolution of the underlying microstructure and the corresponding stress–strain response in polycrystalline metals [42]. With DAMASK, it is indeed possible, for example, to perform large scale simulations, to model damage or fracture [135] and to model the local strain development in the microstructure under deformation [150].

This virtual approach allows to predict the mechanical performance of potential microstructures with a drastic reduction of mechanical tests and experiments before creat-

ing new materials.

The aim of this thesis is to develop and present statistical methods for tackling some of the problems occurring in the identification of the relation between microstructural features and mechanical problems.

In particular, beginning with the microstructure representation problem, we first focus on the geometrical arrangement of the grains and in particular on the use of Poisson-Voronoi diagrams. Providing an accurate representation of the distribution of the main geometrical characteristics of the 3D Poisson-Voronoi cells, using parametric and non-parametric approaches on vast simulation results, will help to obtain insights into the appropriateness of the use of this model for approximating the geometrical microstructure of (single-phase) steels. However, given that commonly the choice of the model is based on 2D microstructure images, a general testing framework for the comparison of 2D Sectional Poisson-Voronoi diagrams and 2D metallic sections is needed. The usual statistical tests employed in this context, are further extended including more accurate measures based on recently developed tools provided by Topological Data Analysis. In cases in which the Poisson-Voronoi diagram hypothesis is rejected, alternative, more complex models are studied and discussed.

The geometrical arrangement of the grains will be then used as a basis for the construction of a statistically based digital twin microstructure. Phases and grain orientations must also be included for a digital representation of the microstructure.

For the mechanical problem counterpart, first, models based on the analysis of mechanical properties from 2D microstructure images are presented. Methods from classical multivariate regression, to LASSO and isotonic regression are applied to gain insight into the relation between microstructural features and mechanical properties. Finally, a virtual experiment is performed. This illustrates the use of statistical methods from the generation of digital twin microstructure to a functional model for understanding the influence of specific microstructural parameters on the strengthening of the material.

OUTLINE

The thesis is divided in two parts: Microstructure (MIC) and Mechanical properties (MEC), corresponding to the acronym of the project: “MICtoMEC: Extensive quantification of microstructure features and statistical relations with mechanical behaviour –from statistical relations to physical understanding–”. In the “MIC” part, some of the microstructure related problems are faced. The focus is mainly on the representation of the geometrical arrangement of the grains.

In Chapter 2, after having reviewed the main mathematical properties of Poisson-Voronoi diagram, the effect of the scaling property of the underlying Poisson process on the distribution of the main geometrical properties of a typical Poisson-Voronoi cell is shown. Moreover, as in the literature no analytical expression has been derived for the main geometrical properties of a Poisson-Voronoi cell, accurate representations, parametric and non-parametric, based on an extensive simulation approach, are given. A first comparison between the volume distribution of the theoretical and a real 3D microstructure is made.

In Chapter 3, methods to formally test whether a real steel microstructure can be approximated by a specific stochastic model are presented. More specifically, a general

framework for testing the Poisson-Voronoi assumption based on images of 2D sections of real metals is proposed. Following two different approaches, according to the use or not of periodic boundary conditions, three different model tests are discussed. The first two are based on the coefficient of variation and the cumulative distribution function of the cells area. The third exploits tools from Topological Data Analysis, such as persistence landscapes.
In Chapter 4, two different digital representation methods are presented. More specifically, a Representative Volume Element (RVE) and a Statistical Similar RVE are produced for the digital representation of a microstructure that present more than one phase (i.e including precipitations). In particular, the arrangement of the grains is represented by Multi-Level Voronoi diagrams.
The second part "MEC" is dedicated to the investigation of the relation between microstructural features and mechanical properties.
In Chapter 5, an approach to study the relation between microstructural parameters and mechanical behaviour of the material based on 2D microstructure images inspection is presented. More specifically, the relation between Geometrically Necessary Dislocations and density of microstructural precipitates is studied in an isotonic regression framework. Already known physics-inspired qualitative relations between 2D microstructure characteristics and 3D mechanical properties act as the starting point of the investigation. Isotonic regression allows to take into account ordering relations and leads to more efficient and accurate results when the underlying assumptions actually hold. The statistical estimation procedure is described considering three different scenarios according to the knowledge of the variances: known variance ratio, completely unknown variances, variances under order restrictions. New likelihood ratio tests are developed in the last two cases. Both parametric and non-parametric bootstrap approaches are developed for finding the distribution of the test statistics under the null hypothesis.
In Chapter 6, a completely simulation-based approach is employed. It begins with the creation of digital twins of different microstructures, or more specifically of SSRVEs, for stainless steel microstructures with an increasing fraction of precipitates, namely carbides $M_{23}C_6$. The resulting virtual microstructures will subsequently be used as samples for virtual tensile tests performed via DAMASK. The resulting stress-strain curves are analysed for understanding the contribution of carbides in the strengthening of the material.

I

MIC

2

3D Poisson-Voronoi Diagrams

For a full comprehension of the relation between the complex materials microstructure and materials properties, it is fundamental to be able to describe the main characteristics of the 3-dimensional microstructure. The most basic model used for approximating steel microstructure is the Poisson-Voronoi diagram. Poisson-Voronoi diagrams have interesting mathematical properties, and they are considered a good model, especially for single-phase materials. Exploiting the scaling property of the underlying Poisson process, the distribution of the main geometrical features of the grains for every value of the intensity parameter are derived. Moreover, a sophisticated simulation program is used to construct a close Monte Carlo based approximation for the distributions of interest. Using this, the closest approximating distributions within the mentioned frequently used parametric classes of distributions is determined. Finally, a 3D volume dataset is considered and the real volume distribution is compared to what is expected under the Poisson-Voronoi model.

Where there is matter, there is geometry.

Johannes Kepler

Parts of this chapter have been published in Computational Materials Science **166**, 111–118 (2019).

2.1. INTRODUCTION

Investigating 3-dimensional structures is a fundamental aspect for many disciplines; especially for those related to materials study, but also for more abstract discipline such as mathematics and statistics. One of the most outstanding aims is to understand fully the intriguing relationship between microstructures and mechanical properties of the materials. The very first step for achieving this objective is quantifying 3D microstructures. From the materials science point of view this means examining and understanding the different nature and variety of microstructures. From the statistics point of view means looking for the characterisation of the 3D virtual microstructures under specific mathematical models.

In the past few years the use of Voronoi diagrams has rapidly increased. These diagrams represent an appealing structure, especially because they describe various natural processes quite well. In [103] an extensive list of fields in which Voronoi diagrams are adopted can be found. Among the many areas of applications of this model, the field of materials science stands out. In fact, Voronoi diagrams are now among the most used mathematical models for microstructure characterisation and depending on the specific kind of materials, it is possible to use a proper category of Voronoi diagrams.

In this Chapter, we discuss the most basic instance of the model: Poisson-Voronoi diagrams. Intuitively, for defining a 3D Poisson-Voronoi diagram, a random set of points (also called generator points, sites or nuclei) is generated in a finite volume and spheres having them as centres are grown at the same time and with the same speed; once two spheres touch a face between them appears. This results in a space-filling configuration made of convex polyhedra, also called cells or grains.

In this framework the nuclei or sites are generated by a homogeneous Poisson process with intensity parameter λ.

Although many interesting mathematical properties of Poisson-Voronoi diagrams are known, there is still much to be discovered about the distributions of the geometrical characteristics of its grains. Through simulations, many authors were able to obtain numerical approximations of the moments of the distribution of the volume, of the surface area, of the number of faces and many other geometrical characteristics of the grains. Nevertheless, analytic expressions of the distributions of many of these important features are not known, others are only known via complicated numerically intractable characterisations. Therefore, various proposals to obtain close approximations to the real distributions were put forward by several authors e.g. Lognormal-, Generalized Gamma- and Rayleigh distributions. But as far as we know, there is no theoretical support for preferring one of these distributions.

In this Chapter, after explaining that λ, the intensity parameter of the Poisson process, is the only parameter determining all distributional properties of the geometrical structure of the grain, we show that if we have the distribution of a given geometrical characteristic for $\lambda = 1$, the distribution of the same quantity for every value of $\lambda > 0$ can be obtained by rescaling. More precisely, we consider volume, surface area and number of faces of the grain, but the approach can be extended to other characteristics. Then, we find a close Monte Carlo based approximation for the previously mentioned geometrical characteristics of the grains and using it we determine the most closely approximating distribution within the mentioned frequently used parametric classes of distributions.

As said before, several well known probability distributions were used for approximating the grain geometrical characteristics distributions, but in this study we determine the 'best' of these.
After reviewing the basic concepts of Voronoi diagrams and the Poisson process in Section 2.2, in Section 2.3 we explain the scaling property of the Voronoi structure in terms of the intensity parameter and how it can be useful for studying distributional properties of the grain features. Since the intensity parameter λ is the only parameter involved in generating a specific structure, it governs the distribution of all the geometrical characteristics of the Poisson-Voronoi typical cell. Later, we explain how the scaling acts on the different geometrical features and we show an empirical example of what happens changing the scale parameter. Section 2.4 describes the present simulation approach and produces an accurate Monte Carlo approximation for the distribution of the grain volume and the grain surface area. In fact, we provide the approximate distributions of the volume and of the grain surface area for $\lambda = 1$ and we can adapt it for the other values of λ using the aforementioned scaling properties. In Section 2.5, we study how well the true distributions of the geometrical characteristics can be approximated by some well-known and frequently used probability distributions in this context: the Gamma, Generalized Gamma- and Lognormal distribution. Fitting these three distributions and comparing them through statistical measures, such as the supremum distance between the Monte Carlo empirical distribution and its parametric approximations and Total Variation distance, we are not only able to identify the best approximation but also to give a measure of error for each of these parametric approximations.
In Section 2.6 an application to real data is illustrated. Finally, we introduce the possibility to extend our approach according to different Voronoi Diagrams cases, such as Multi-level Voronoi and/or Laguerre Voronoi Diagrams later deepened in Chapter 4. For the 3D Voronoi diagrams generation we use Tata Steel software and for data analysis the statistical software R.

2.2. BASIC CONCEPTS

We begin by reviewing the generic definition and the basic properties of the Poisson-Voronoi Diagram. Given a denumerable set of distinct points in $\mathbb{R}^d$, $\mathbf{X} = \{x_i : i \geq 1\}$, the Voronoi diagram of $\mathbb{R}^d$ with nuclei $\{x_i\}$ (also called sites or generator points) is a partition of $\mathbb{R}^d$ consisting of cells

$$C_i = \{y \in \mathbb{R}^d : \|x_i - y\| \leq \|x_j - y\|,\ j \neq i\},\ \ i = 1, 2, \ldots \tag{2.2.1}$$

where $\|\cdot\|$ is the usual Euclidean distance. This means that given a set of two or more but finitely many distinct points, we associate all locations in that space with the closest member(s) of the point set with respect to the Euclidean distance.
If we assume that $\mathbf{X} = \Phi = \{x_i\}$ is the realisation of a homogeneous Poisson point process, we will refer to the resulting structure as the Poisson-Voronoi diagram, $\mathcal{V}_\Phi$.
We find useful to remind briefly what a Poisson process is and which are its basic properties. For readers that aim to a formal definition, in [71] more details are provided.
Let S be a measurable set in $\mathbb{R}^d$. Moreover, denote $N(A) = \#\{i : x_i \in A\}$. $N(A)$ represents the total number of 'events' that occur in A. A Poisson process on S is then a random countable subset Φ of S, such that

- for every finite family of disjoint bounded subsets $A_1, A_2, \ldots, A_n$ of S, the random variables $N(A_1), N(A_2), \ldots, N(A_n)$ are independent
- $N(A)$ has Poisson distribution $\mathscr{P}(\lambda)$, where $\lambda = \mu(A) \in [0, \infty)$.

From this it immediately follows that

$$\mu(A) = \mathbb{E}\{N(A)\}.$$

Therefore the measure μ on S is often called the mean measure of the Poisson process Φ. When $S = \mathbb{R}^d$, the mean measure is in most interesting cases given in terms of its intensity. This is a nonnegative measurable function λ on S, in terms of which μ is given by integrating λ with respect to d-dimensional Lebesgue measure:

$$\mu(A) = \int_A \lambda(x) \mathrm{d}x. \tag{2.2.2}$$

If λ is continuous at x, then Eq. 2.2.2 implies that for small neighbourhoods A of x,

$$\mu(A) \approx \lambda(x)|A|,$$

where $|A|$ denotes the Lebesgue measure (length if $d = 1$, area if $d = 2$, volume if $d = 3$) of A. Thus $\lambda(x)|A|$ is the approximate probability of a point of Φ falling in the small set A, and it is larger in regions where λ is large than in those where λ is small. In the special case when λ is a constant, so that

$$\mu(A) = \lambda|A| \tag{2.2.3}$$

we speak of a uniform or homogeneous Poisson process.
In this Chapter, we assume that the sites of the Poisson-Voronoi diagrams are generated according to the particular case described by Eq. 2.2.3.
As mentioned before, our aim is to find the distribution of the geometrical characteristics of the grains. In order to approximate these distributions, we generate a large sample of independent and identically distributed cells, more specifically typical cells. A typical Voronoi cell refers to a random polytope which loosely speaking has the same distribution as a randomly chosen cell from the diagram selected in such a way that every cell has the same chance of being sampled. Moreover, the distribution of the typical Poisson-Voronoi cell is by Slivnyak-Mecke formula [95] the same as the Voronoi cell containing the origin, obtained when the origin is added to the point process Φ. This formally corresponds to

$$\mathscr{C} = \{y \in \mathbb{R}^d : \|y\| \leq \|y - x\|, \ x \in \Phi\}.$$

Okabe et al. [103] synthesise previous research activity about the properties of Poisson Diagrams. Despite the fact that distributions of several geometrical characteristics are already known in 2D, the distributions of the main features in higher dimensions, e.g. in 3D, are not. We describe a simulation approach to approximate these distributions in the next Section.

2.3. DISTRIBUTION OF THE GEOMETRICAL CHARACTERISTICS

Given the complexity of finding explicit formulae for the distributions of the Poisson-Voronoi diagram geometrical characteristics, especially in 3D, many authors used Monte Carlo methods to approximate these. Among them Kiang [70], Kumar and Kurtz [74], Lorz and Hahn [83], Møller [95], Tanemura [149] obtained numerical results for the moments of the distribution of volume, surface area, and number of faces of the grains in 3D. They also give histogram estimates of these distributions and suggest approximations for them using various well known probability distributions. For instance, for the volume distribution, before 1990 most authors used the Lognormal distribution for approximating the grain size distribution in polycrystals. Nowadays, more flexible distributions such as Gamma or Generalized Gamma are commonly used (e.g. [74, 149]). The use of Gamma type distribution has also a geometrical root. In fact, it can be related to the distribution of the volume of the typical cell of the Poisson-Delaunay triangulation (dual graph of the poisson-Voronoi diagram) studied first by R. Miles [92] and more recently by the authors in [34]. Although these models fit the observed data rather well (as we will see in the next Section) our approach allows to find an accurate representation of the true distribution and the parametric distribution that optimally fits the data.
The main idea is that, given a Poisson-Voronoi diagram generated by a Poisson point process Φ with intensity parameter λ, this λ is the only parameter determining the distributions of the geometrical features of the grains. Furthermore, the dependence of the distributions on the intensity parameter is via simple scaling of a 'parent distribution', due to the following important scaling property of the Poisson process.

Lemma 2.3.1 (Scaling Property)**.** *Let $\Phi = \{X_1, X_2, \ldots\}$ be a Poisson process on $\mathbb{R}^d$ with intensity $\lambda = 1$. Choose $\lambda > 0$ and define $\Phi_\lambda = \{X_1/\lambda^{1/d}, X_2/\lambda^{1/d}, \ldots\}$. Then Φ_λ is a Poisson process with intensity λ.*

Proof. The fact that Φ_λ is a Poisson process is a special instance of the 'Mapping theorem' [see 71, Section 2.3], using states space $S = T = \mathbb{R}^d$ and $f(x_1, x_2, \ldots, x_d) = (x_1/\lambda^{1/d}, x_2/\lambda^{1/d}, \ldots, x_n/\lambda^{1/d})$. Denoting the mean measure of Φ (Lebesgue measure) by μ_1, the induced mean measure μ_λ of Φ_λ is given by

$$\mu_\lambda(B) = \mu_1(f^{-1}(B)) = \int_{f^{-1}(B)} \mathrm{d}\mu_1(x) = \lambda \int_B \mathrm{d}\mu_1(x) = \lambda\mu_1(B)$$

□

In the following Sections, Lemma 2.3.1 will be used to study the dependence of the distributions of volume, surface area and number of faces of the grains on the intensity parameter λ.

GRAIN VOLUME

We first focus our attention on the grain volume distribution because of the direct relationship of this Poisson-Voronoi geometrical characteristic and the grain size distribution in microstructure characterisation of materials.
Exploiting the properties of the Poisson process, the distribution for the normalised

length of the Voronoi cell in 1D or size measure in 1D, can be shown to have density [91]

$$f_{1D}(y) = 4y\exp(-2y)\ \ 1_{[0,\infty)}(y)$$

In dimension $d > 1$, it was conjectured that the area (2D) and the volume (3D) of the typical cell in a Poisson-Voronoi diagram may be distributed as the sum of two and three gamma variables with shape and scale parameters equal to 2 [70], but [164] and [39] showed the conjecture to be false. In 2D an analytic, though computationally challenging result is provided by Calka [23], which gives an expression for the distribution of the area of the typical cell in 2D given the number of vertices. In 3D, as we know so far, no trivial analytic expression for the volume distribution exists.

Lemma 2.3.2. *Denote by F_λ the distribution function of the volume (length if $d = 1$, area if $d = 2$) of the typical cell of the Poisson-Voronoi diagram based on a homogeneous Poisson process on $\mathbb{R}^d$ with intensity parameter $\lambda > 0$. Then, for all $x \geq 0$,*

$$F_\lambda(x) = F_1(\lambda x) \tag{2.3.1}$$

Proof. Let Φ be a homogeneous Poisson process on $\mathbb{R}^d$ with intensity 1. Denote by $\mathscr{C}$ the typical cell of the Voronoi diagram based on this process. Fix $\lambda > 0$ and consider the homogeneous Poisson process Φ_λ with intensity λ as introduced in the statement of Lemma 2.3.1. Then the typical cell in the Voronoi diagram based on Φ_λ is a scaled version of the typical cell of the Voronoi diagram based on Φ, in the sense that it is given by $\mathscr{C}_\lambda = \{x/\lambda^{1/d} : x \in \mathscr{C}\}$. This means that the volume V_λ of $\mathscr{C}_\lambda$ is exactly λ^{-1} times the volume V of $\mathscr{C}$. Therefore, for $x \geq 0$,

$$F_\lambda(x) = \mathrm{P}(V_\lambda \leq x) = \mathrm{P}\left(\frac{V}{\lambda} \leq x\right) = \mathrm{P}(V \leq \lambda x) = F_1(\lambda x)$$

□

GRAIN SURFACE AREA

Lemma 2.3.3. *Denote by G_λ the distribution function of the surface area of the typical cell of the Poisson-Voronoi diagram based on a homogeneous Poisson process on $\mathbb{R}^3$ with intensity parameter $\lambda > 0$. Then, for all $x \geq 0$,*

$$G_\lambda(x) = G_1\left(\lambda^{\frac{2}{3}} x\right)$$

Proof. The argument follows the proof of Lemma 2.3.2. Denote by S_λ the surface area of $\mathscr{C}_\lambda$ and note that scaling of $\mathscr{C}_\lambda$ implies that S_λ is $\lambda^{-\frac{2}{3}}$ times the surface area of $\mathscr{C}$, S. Therefore

$$G_\lambda(x) = \mathrm{P}(S_\lambda \leq x) = \mathrm{P}\left(\frac{S}{\lambda^{\frac{2}{3}}} \leq x\right) = \mathrm{P}\left(S \leq \lambda^{\frac{2}{3}} x\right) = G_1\left(\lambda^{\frac{2}{3}} x\right)$$

□

NUMBER OF GRAIN FACES

Finally, another (discrete) property of interest regards the number of grain faces of the typical cell. It is clear that using either Φ or Φ_λ (from Lemma 2.3.1) as a basis for the Voronoi diagram, yields the same number of faces of the typical cell ($\mathscr{C}$ or $\mathscr{C}_\lambda$ respectively), leading to

Lemma 2.3.4. *Denote by N_λ the distribution function of the number of faces of the typical cell of the Poisson-Voronoi diagram based on a homogeneous Poisson process on $\mathbb{R}^d$ with intensity parameter $\lambda > 0$. Then, for all $x \geq 0$,*

$$N_\lambda(x) = N_1(x)$$

The same lemma holds for number of corner points, n_v. In fact, exploiting the Euler-Poincaré relation [103], it is possible to determine n_v when the number of faces is known.

2.4. NON-PARAMETRIC APPROACH

Now, we approximate the distribution function of the grain geometrical features, using the results obtained by a simulation based on 1 000 000 Voronoi diagrams. We consider the volume, the surface area and the number of faces of a 3D Poisson-Voronoi typical cell. Two possible simulation approaches, well described in [103] are possible:

1. generate a large number of points inside a bounded region B according to Φ, construct $\mathcal{V}_\Phi$ and measure the characteristics of all its cells.

2. generate a sequence of independent typical Poisson-Voronoi cells, measure the characteristics of each and then aggregate them to obtain the required distributions.

We follow the second approach. The reason for this choice derives from the convenience of having a sample of independent and identically distributed Voronoi cells such that we can quantify the agreement with the real distribution. Moreover, we are able to control and eliminate the boundary effect that is present because the structure is actually only constructed on a bounded region. For our objective only the distributions of the geometrical properties of the typical cell are needed, using $\lambda = 1$ in the simulations. By Lemma 2.3.2, 2.3.3 and 2.3.4, the distributions based on diagrams with different intensities can be obtained by scaling.

We conduct our simulation approach using the Voronoi software provided by Tata Steel. The algorithm is based on the half plane intersection, which is closely related to the original definition of a Voronoi tessellation. Each Voronoi cell is constructed separately by intersecting $n-1$ half spaces, where n is the number of generator points. A disadvantage is that this algorithm computes in $O(n^2 \log n)$ time [104], while the most frequently used incremental algorithms require $O(n^2)$ time. To accelerate the computations, the algorithm has been extended with a filter, which determines which neighbouring points of a generator point are needed for the Voronoi cell construction of this site. This filter is built in such a way that it first sorts $\sim 80\%$ of the points which are certainly needed for Voronoi cell construction. After that, the other $\sim 20\%$ of the points are checked to see if they give half plane intersection with the Voronoi cell under construction. With

this filter the computational speed is improved to be better than $O(n \log n)$, which is the computational speed of the fastest algorithm by Fortune [41].
We adopt the following Monte-Carlo procedure.
Repeat 1 000 000 times:

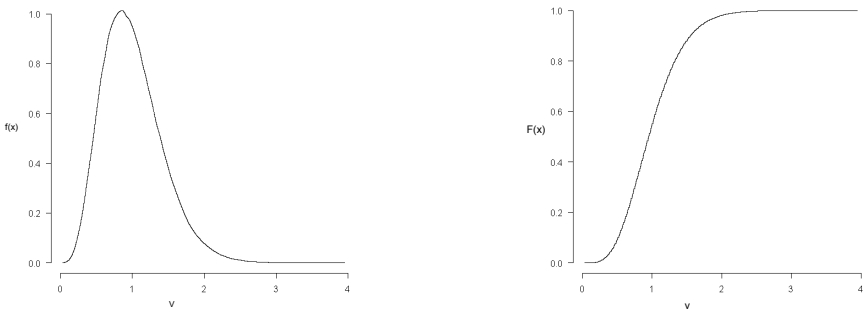
Step 1 : Generate a 3D Poisson-Voronoi diagram with added generator point $(0,0,0)$ with $\lambda = 1$;

Step 2 : Determine the geometrical characteristics of the realisations of the typical Voronoi cell, the cell that contains the point $(0,0,0)$, $\mathscr{C}(0)$;

Then, aggregate the 1 000 000 values.
The main graphical results are shown in Figures 2.1, 2.2 and 2.3. In Tables 2.1 and 2.2, we report the estimated moments of the main geometrical characteristics and the estimated probabilities for the number of faces. They are coherent with both the theoretical and numerical results obtained by other authors [74, 149].

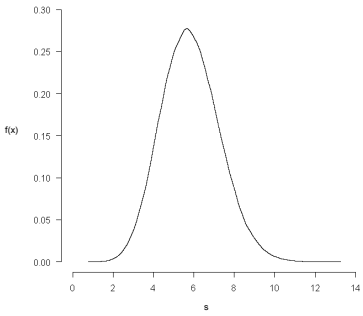
Table 2.1: Estimated moments of the geometrical features of 1 000 000 Poisson-Voronoi typical cells, λ=1

(a) Volume		(b) Surface area		(c) Number of faces	
μ_1	1.00008	μ_1	5.82670	μ_1	15.53071
σ	0.41189	σ	1.43821	σ	3.33896
μ_2	1.16981	μ_2	36.01888	μ_2	252.35173
μ_3	1.55900	μ_3	234.69091	μ_3	4277.80397
μ_4	2.32340	μ_4	1603.48468	μ_4	75464.60519

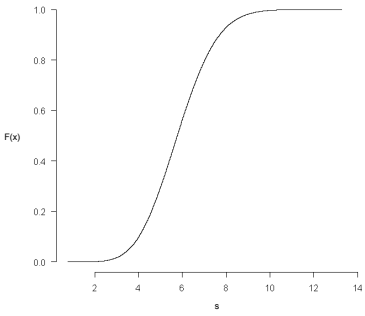


(a) (b)

Figure 2.1: (a) Kernel density estimate (Epanechnikov kernel, cross validation bandwidth $h = 0.05$) and (b) empirical cumulative distribution function of volume of 1 000 000 Poisson-Voronoi typical cells, $\lambda = 1$

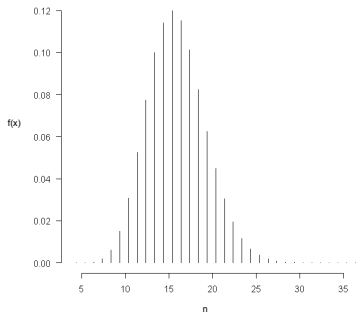


(a)

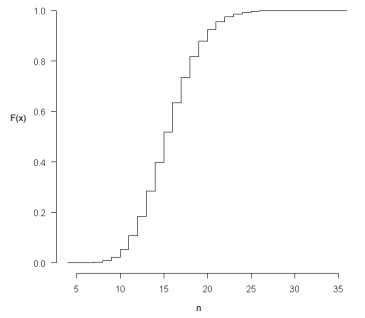


(b)

Figure 2.2: (a) Kernel density estimate (Epanechnikov kernel, cross validation bandwidth $h = 0.25$) and (b) empirical cumulative distribution function of surface area of 1 000 000 Poisson-Voronoi typical cells, $\lambda = 1$



(a)



(b)

Figure 2.3: (a) Relative frequencies and (b) empirical cumulative distribution function of number of faces of 1 000 000 Poisson-Voronoi typical cells, $\lambda = 1$

Table 2.2: Distribution of the number of faces (F) of 1 000 000 Poisson-Voronoi typical cell, $\lambda = 1$

F	n_f	p_f	F	n_f	p_f	F	n_f	p_f
4	5	0.000005	16	115188	0.115188	28	435	0.000435
5	35	0.000035	17	101151	0.101151	29	224	0.000224
6	316	0.000316	18	82277	0.082277	30	95	0.000095
7	1822	0.001822	19	62408	0.062408	31	52	0.000052
8	6190	0.006190	20	44944	0.044944	32	18	0.000018
9	15051	0.015051	21	30477	0.030477	33	3	0.000003
10	30685	0.030685	22	19466	0.019466	34	1	0.000001
11	52528	0.052528	23	11682	0.011682	35	1	0.000001
12	77421	0.077421	24	6756	0.006756	36	1	0.000001
13	100094	0.100094	25	3631	0.003631			
14	114163	0.114163	26	1890	0.001890			
15	120015	0.120015	27	975	0.000975			

2.5. PARAMETRIC APPROACH

Various proposals to estimate the distributions of the geometrical properties of the typical cell were put forward by several authors such as the Lognormal distribution [142, 143], Generalized Gamma distribution with 2 [154] or 3 parameters [149] and Rayleigh distribution [105]. Ferenc and Néda [39] propose their own function for the volume distribution.

As noted in [154] the use of the Lognormal distribution function for representing grain size distribution lacks a solid physical basis and is not in general accurate. Nowadays, the debate regards mostly the Generalized Gamma Distribution with 2 or 3 parameters, but until now no physical explanation for using one preferential distribution exists. However, in view of the scaling properties described in the previous Sections, it is natural to think that the distributions of the geometrical characteristics of the grain belong to a scale parametric family of distributions. Only then the distributions of the quantities *for all* λ can belong to the class. One could, for instance, consider the Lognormal distribution. Its probability density function is given by

$$f(x|\mu,\sigma) = \frac{1}{x\sigma\sqrt{2\pi}} \exp\left(-\frac{(\log(x)-\mu)^2}{2\sigma^2}\right).$$

Let $\hat{\mu}_1$ and $\hat{\sigma}_1$ be the maximum likelihood estimates when $\lambda = 1$ (based on the 1 000 000 simulated values). Then, define a scale family based on that, $f_\lambda(x)$ as:

$$f_\lambda(x) = \lambda f(\lambda x|\hat{\mu}_1,\hat{\sigma}_1) = \frac{1}{x\hat{\sigma}_1\sqrt{2\pi}} \exp\left(-\frac{(\log(x)+\log(\lambda)-\hat{\mu}_1)^2}{2\hat{\sigma}_1^2}\right)$$

which corresponds to a Lognormal distribution with parameter vector $(\hat{\mu}_1 - log(\lambda), \hat{\sigma}_1^2)$. Therefore, we have a log-addition scaling on the first parameter, which is not consistent with the λ-scaling that is found for real distributions. Now let us consider the Generalized Gamma distribution. Its density function, parametrised according to [145], is given by

$$f(x|a,b,k) = \frac{bx^{bk-1}}{\Gamma(k)a^{bk}} e^{-\left(\frac{x}{a}\right)^b} \tag{2.5.1}$$

where a and b are the shape and the scale parameters, k the family parameter. Let $\hat{a}_1$, $\hat{b}_1$ and $\hat{k}_1$ be the maximum likelihood estimates for the parameters (based on the 1 000 000 simulated values) when $\lambda = 1$. Define $f_\lambda(x)$ as equal to:

$$f_\lambda(x) = \lambda f(\lambda x|\hat{a}_1,\hat{b}_1,\hat{k}_1) = \frac{\hat{b}_1 x^{\hat{b}_1\hat{k}_1-1}}{\Gamma(\hat{k}_1)} \left(\frac{\lambda}{\hat{a}_1}\right)^{\hat{b}_1\hat{k}_1} e^{-\left(\frac{\lambda}{\hat{a}_1}x\right)^{\hat{b}_1}}$$

which corresponds to a Generalized Gamma with parameters $(\frac{\hat{a}_1}{\lambda}, \hat{b}_1, \hat{k}_1)$. This suggests to look for a distribution that belongs to this scale family. Special cases of this family are the Gamma distribution with parameters a, k and $b = 1$ and the Weibull distribution with parameters a, b and $k = 1$. Beside the parametrisation in Eq. 2.5.1, another one is provided by Prentice [111]. This is in general more stable in the estimation of the parameters but both parameterizations lead to the same estimates.

In Tables 2.3-2.4 the estimated parameters of the best Generalized Gamma approximations for the volume and the surface area respectively are reported. After a graphical inspection (see Figures 2.4-2.5 for the volume and Figures 2.6-2.7 for the surface area), the fits based on the Gamma distribution, the Generalized Gamma distribution and the Lognormal distribution are statistically compared using two criteria (Table 2.5 for the volume and Table 2.6 for the surface area):

- Supremum distance between two distribution functions:

$$D(F,G) = \sup_{x\in\mathbb{R}} |F(x) - G(x)| \tag{2.5.2}$$

  This distance is computed between the empirical distribution function F_n of the sample and the maximum likelihood fit within the respective parametric families. The data are the 1 000 000 simulated values from the distribution of interest, with $\lambda = 1$.

- Total Variation distance between distributions with distribution functions F and G and densities f and g respectively on $\mathbb{R}$:

$$TV(F,G) := \sup_{A\in\mathscr{B}} \left| \int_A dF(x) - \int_A dG(x) \right| = \frac{1}{2}\int |f(x) - g(x)|\, dx \tag{2.5.3}$$

  This distance is computed between the kernel estimate of the densities and maximum likelihood parametric fits based on the simulation results with $\lambda = 1$.

Note that information on these distances is based on the data obtained with $\lambda = 1$. If the estimates for more general values of λ are obtained via the rescaling, these distances do, however, not change under this scaling, so the distances also hold for the other values of λ.

Table 2.3: Estimated Generalized Gamma parameters for volume distribution approximation, $\lambda = 1$

	$\hat{a}$	$\hat{b}$	$\hat{k}$
Estimate	0.380	1.287	3.583
Std. Error	0.005	0.006	0.0322

Table 2.4: Estimated Generalized Gamma parameters for surface area distribution approximation, $\lambda = 1$

	$\hat{a}$	$\hat{b}$	$\hat{k}$
Estimate	3.174	2.102	3.839
Std. Error	0.025	0.011	0.036

Table 2.5: Comparison of Gamma-, Generalized Gamma- and Lognormal approximations for volume distribution in terms of Supremum- and Total Variation distance

	Gamma	Generalized Gamma	Lognormal
Supremum distance	0.013	0.005	0.041
TV distance	0.018	0.005	0.089

Table 2.6: Comparison of Gamma-, Generalized Gamma- and Lognormal approximations for surface area distribution in terms of Supremum- and Total Variation distance

	Gamma	Generalized Gamma	Lognormal
Supremum distance	0.020	0.002	0.037
TV distance	0.035	0.003	0.082

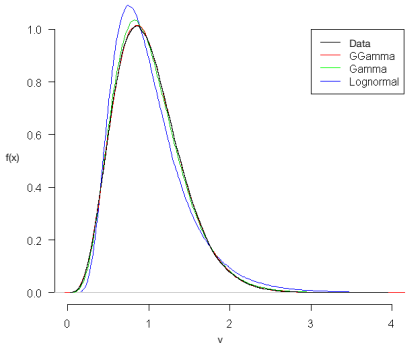
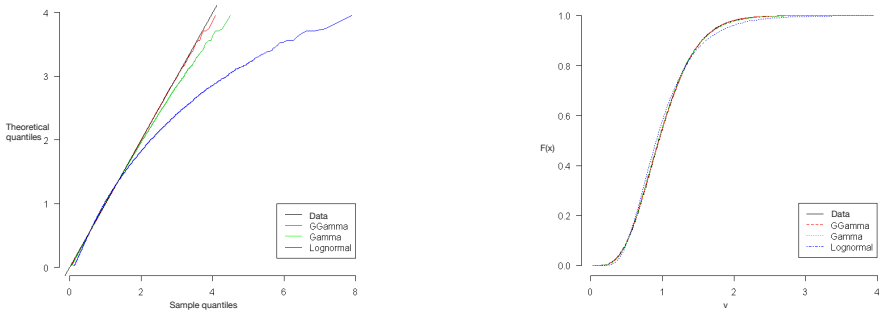


Figure 2.4: Comparison of parametric approximations to the volume distribution of 1 000 000 Poisson-Voronoi typical cells, $\lambda = 1$



(a) (b)

Figure 2.5: (a) QQplot and (b) cumulative distribution function comparison of parametric approximations to the volume distribution of 1 000 000 Poisson-Voronoi typical cells, $\lambda = 1$

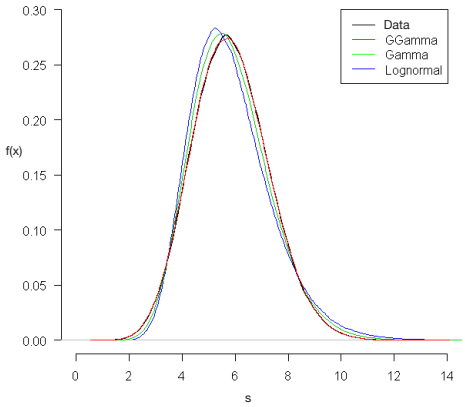
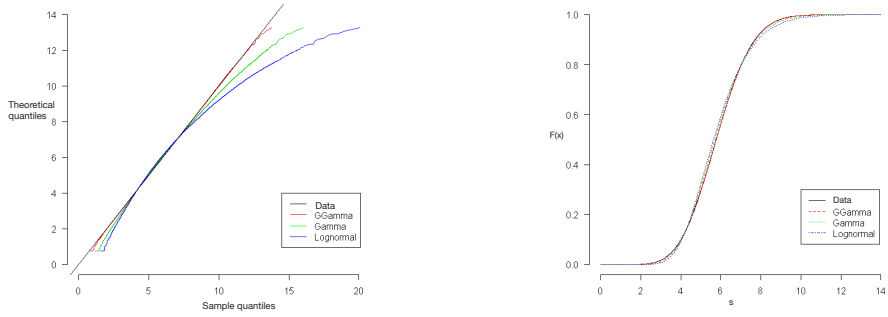


Figure 2.6: Comparison of parametric approximations to the surface area distribution of 1 000 000 Poisson-Voronoi typical cells, $\lambda = 1$



(a) (b)

Figure 2.7: (a) QQplot and (b) cumulative distribution function comparison of parametric approximations to the surface area of 1 000 000 Poisson-Voronoi typical cells, $\lambda = 1$

2.6. APPLICATION

Data used for this application are kindly provided by Erik Offerman (TU Delft). They are relative to 882 grains in an actual steel microstructure in a volume of 950 μm × 1100 μm × 400 μm. The main information collected from the processed experimental data set is:

- center of mass of each grain;
- equivalent spherical radius;
- orientation as Miller indices.

More details about the 3D microstructure and the 3DXRD measurement can be found in [137, 136].
A kernel density esitmate of the volume distribution is shown in Fig. 2.8. First, an

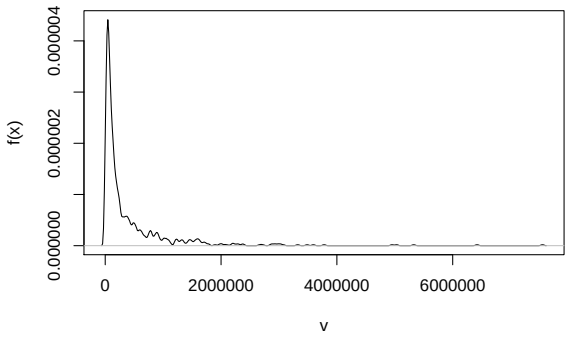


Figure 2.8: Kernel density estimate (Epanechnikov kernel, cross validation bandwidth $h = 21735.28$)

estimate of λ is required for fitting. The most common estimator is given by the ratio between the number of grains and the size of the domain; in the specific case $\hat{\lambda} = 2.11 \times 10^{-6} \mu\text{m}^{-3}$. Another option is to determine the best λ for the fitting. For this purpose, we propose a moment estimator. Let $\mathscr{F}$ be a class of distribution functions $\mathscr{F} = \{\mathrm{F}_\lambda : \mathrm{F}_\lambda(x) = \mathrm{F}_1(x\lambda)\}$ and $V_1, \dots V_n \sim \mathrm{F}_\lambda$ (see Lemma 2.3.2). Then,

$$\mu_\lambda = \int_0^\infty (1 - F_\lambda(t))\mathrm{d}t = \frac{1}{\lambda}\int_0^\infty (1 - F_1(t\lambda))\mathrm{d}t\lambda = \frac{\mu_1}{\lambda} \tag{2.6.1}$$

Note that in this context $\mu_1 = \frac{a\Gamma(k+\frac{1}{b})}{\Gamma(k)}$, known for the Generalized Gamma distribution.

Let $\bar{V}$ be the empirical mean. Then, the moment estimator for λ is:

$$\bar{V} = \frac{\mu_1}{\lambda};\ \hat{\lambda} = \frac{\mu_1}{\bar{V}} \tag{2.6.2}$$

This leads to $\hat{\lambda} = 2.64 \times 10^{-6} \mu\text{m}^{-3}$.

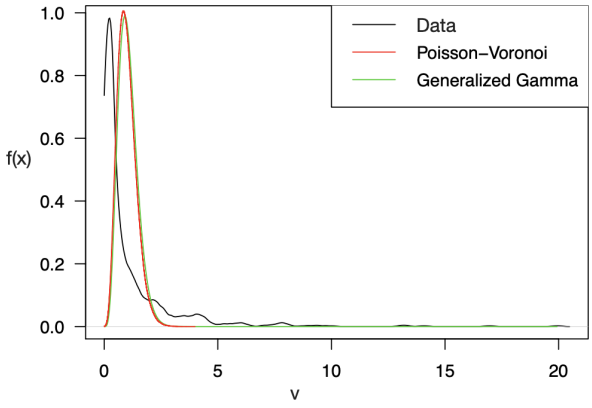
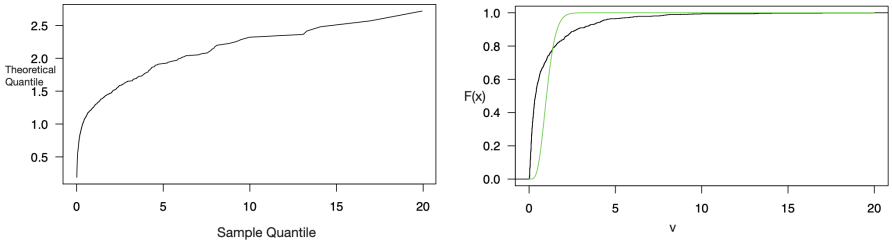


Figure 2.9: Comparison of parametric approximations to the real volume distribution (Epanechnikov kernel, cross validation bandwidth $h = 0.057$, black line), $\lambda = 1$



(a) (b)

Figure 2.10: (a) QQplot and (b) cumulative distribution function comparison of Generalized Gamma distribution to the real volume distribution, $\lambda = 1$

In Figures 2.9, 2.10 (a), 2.10 (b) a graphical comparison in terms of probability density function, qq-plot (quantile-quantile plot) and cumulative distribution function, respectively is performed. At a first sight the result discourages the use of Poisson-Voronoi diagram for this dataset. One major difference is related to the presence of many more small cells in the real microstructure than in the Poisson-Voronoi setting. In fact, the measurement inaccuracy of the smallest cells is a very well known problem in literature [28]. Moreover, volume values close to 0 may be attributed also to the non space filling reconstruction even in the centre regions, as reported by data providers. This over-representation of small cells will also lead to an inaccurate estimate of λ and have a global impact on the comparison of both distributions. It is interesting to see whether the distributions in the higher volume regions fit better. One way to look at this is by conditioning on the (e.g. 10%) highest observed volumes. This conditional distribution then has to be compared to an appropriate Generalized Gamma distribution. We use a

(conditional) method of moments estimate for λ to rescale the data on the same level as was done in Figure 2.10 (b). This leads to Fig. 2.11. In this graph we still see a difference between the two distribution functions as it comes to the thickness of the tails. However, the general shape of both conditional distributions is quite similar.
All in all, we would not recommend the use of the Poisson-Voronoi model for the data at hand because of some complications (as the overrepresentation of small volumes, maybe due to premature stopping of the generating process) that could be addressed by using other models, such as Weighted Voronoi Diagrams. On the other hand, if especially the distributional behaviour of the highest volumes is of interest and there are indications of inaccurate measurements of the smallest grains, the Poisson-Voronoi model may be used as a reasonable approximation and as a way of extrapolating distributional properties for cells with volume values close to 0.

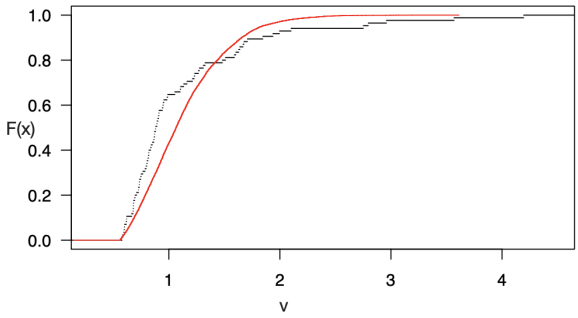


Figure 2.11: Cumulative distribution function comparison of Generalized Gamma distribution to the highest values of volume distribution $\lambda = 1$

2.7. CONCLUSIONS

In this Chapter a very accurate representation for the distributions of the main geometrical characteristics of Poisson-Voronoi typical cell is provided. It is possible to exploit the approximated distribution for generating observations of approximately every geometrical characteristic that defines the grain size and for every possible value of λ. Moreover, we show that the Generalized Gamma distribution, with parameter $\hat{a} = 0.380$, $\hat{b} = 1.287$ $\hat{k} = 3.583$ for the volume and $\hat{b} = 3.174$, $\hat{a} = 2.102$, $\hat{k} = 3.839$ (Tab. 2.3 and 2.4) for the surface area is the best approximation in the class of the commonly used parametric distributions for grain size distributions.
Nevertheless, it is not the true underlying distribution. In fact, the interpretation of the total variation distance as a measure of quality allows to say that using Generalized Gamma approximation for the grain volume distribution we could commit an error of about 0.5% and about 0.3% for the grain surface area (Tab. 2.5 and 2.6).
As noted in the introduction, Poisson-Voronoi diagrams are interesting and widely applied, but for modeling microstructures only constitute the most basic case. Their use in microstructure characterization is not fully evaluated yet. Therefore, we want to test

their applicability (Chapter 3) and then extend our work to more general and less understood Voronoi structures (Chapter 4), such as Multi-Level Voronoi diagrams [72] or Laguerre-Voronoi tessellations [87] in which the convenient scaling properties present in the Poisson-Voronoi diagrams are less obvious.

3

POISSON-VORONOI HYPOTHESIS TESTING

The aim of this Chapter is to develop methods that can be used to test whether a real steel microstructure can be approximated by a specific stochastic model. As an example, a general framework for testing the Poisson-Voronoi assumption based on images of two dimensional sections of real metals is set out. Following two different approaches, according to the use or not of periodic boundary conditions, three different model tests are proposed. The first two are based on measures related to the cells area: the coefficient of variation and the cumulative distribution function of the cells area. The third exploits tools from Topological Data Analysis, such as persistence landscapes constructed using the centres of mass of the observed 2D sectional grains.

Persistence is to the character of man as carbon is to steel.

Napoleon Hill

Parts of this chapter have been published in Applied Stochastic Models in Business and Industry.; 1–24 (2020).

3.1. INTRODUCTION

As stated in the previous Chapters, the first step in the investigation of mechanical properties is finding a good model for metal microstructures. In fact, having a good model for the microstructure, simulations can be performed to generate 'digital versions' of the microstructure and testing its properties, using yet other models that establish the relation between microstructural and mechanical properties.
It is clear that an important and challenging statistical question to be answered is whether a specific model for a microstructure is adequate, given measured data. In the tentative answering of this last question several points need to be touched upon. The first point concerns the choice of a model. There exists a vast choice of models and among them, Voronoi diagrams have been extensively studied and used [103]. In particular, as seen in Chapter 2, Poisson-Voronoi diagrams, only involving one nonnegative intensity parameter λ, represent the most basic case for modelling microstructures. In fact, they are often used in applications involving single-phase steel [73, 74, 103]. More sophisticated models have been proposed, but in this Chapter we will concentrate on the Poisson-Voronoi model.
A second point concerns the available data. While the microstructure of a material is the arrangement of grains and phases in a three dimensional space, the material is typically observed in two dimensions. Usually, a small sample from inside the material is obtained and the exposed surface is examined in a microscope. Therefore, the work involves the study of 2D sections from which 3D microstructure information has to be extracted.
Under the 3D Poisson-Voronoi model, the observable 2D section is a realisation of a so called 2D Sectional Poisson-Voronoi diagram, often denoted by $\mathcal{V}_\Phi(2,3)$. It is the result of the intersection of a fixed plane and a 3D Poisson-Voronoi diagram. Only limited results about the geometrical characteristics of its grains have been obtained analytically but for most of them numerical results have been obtained through Monte Carlo simulations [81]. If a Poisson-Voronoi diagram is a good model, using 2D sections for the estimate of the intensity parameter λ, it is possible to infer distributions of almost all 3D microstructural properties, such as grain volume, grain surface area and grain number of faces (see Chapter 2).
The last point is about the model validation. The question that this Chapter wants to answer is "Given a real 2D materials section, could a Poisson-Voronoi diagram be a good model for approximating the 3D materials microstructure?" We propose several tests for the Poisson-Voronoi hypothesis. These are all based on contrasts between features of the observed 2D picture and the features one would expect if the data were generated according to the Poisson-Voronoi model.
The Chapter structure is as follows. In Section 3.2, after having reviewed the basic concepts of 2D Sectional Poisson-Voronoi diagrams, we recall the main stereological relations which can be used to estimate λ based on a 2D Sectional Poisson-Voronoi diagram and the most used intensity estimators introduced in [49]. In Section 3.3, the distributions of the main geometrical characteristics of the 2D sectional cells are numerically obtained. We distinguish periodic and non periodic boundary conditions. The former case is very popular in materials science practice and it allows to approximate 'infinite structures', giving nice scaling properties and avoiding so called "edge effects". The latter more closely resembles real situations.

Then, we move to the testing framework (Section 3.4). Three model tests are proposed. The first, already introduced in [50], is based on the coefficient of variation of the cell (or grain) areas; the second is a Kolmogorov-Smirnov type test based on the cumulative distribution function of the cell areas. In the non periodic boundaries case, an additional test is defined, using tools from the emergent area of Topological Data Analysis (TDA), which combines the two disciplines of statistics and topology. The focus is on persistent homology, the branch of TDA used for identifying qualitative features of data and to give a measure of the importance of those featuresAfter having briefly and intuitively explained the basic concepts of persistent homology and the common ways of representing it (persistence diagram), a test based on the squared distances between persistence landscapes is presented.
In Section 3.5, we carry out a computer simulation for estimating the quantiles for the proposed model test statistics. We consider null distributions for the test statistics conditional on the number of visible cells in 2D. For a general test statistic, the conditional distribution is expressed in terms of quantities that involve the (unknown) intensity parameter λ of the 3D Poisson process and quantities independent of λ. Therefore a bootstrap approach for computing a 90% confidence interval for λ is proposed.
In Section 3.6 the power of the tests is discussed with respect to a specific parametric alternative hypothesis: 2D Poisson-Voronoi diagram. The new tests proposed in Section 3.4 result to be more powerful than the one already proposed in literature. Finally, in Section 3.7, we show an application of our work based on scanned images by [50] of Alumina Ceramics. The different tests belonging to the different approaches are performed and the results are compared. A brief discussion on future developments follows in Section 3.8.

3.2. BASIC CONCEPTS

In real experiments of microstructure observation, it is often not possible to deal directly with 3D structures. Instead, one has to base inference on pictures of 2D sections of the 3D structure. The theoretical baseline structure in this Chapter is the 2D Sectional Poisson-Voronoi tessellation. This structure is produced by the intersection between a two dimensional plane and a Poisson-Voronoi diagram generated by a Poisson point process Φ in $\mathbb{R}^3$, resulting in the two dimensional Sectional Poisson-Voronoi, denoted by $\mathcal{V}_\Phi(2,3)$.
In a more general context, Chiu et al. [25] answer a fundamental question: “For integers $2 \leq t \leq d-1$, is the intersection between an arbitrary but fixed t-dimensional linear affine subspace of $\mathbb{R}^d$ and the d-dimensional Voronoi tessellation generated by a point process Φ a $t-$dimensional Voronoi tessellation?" The answer to this question is negative when Φ is a Poisson point process [25, 90]. Moreover, each cell in a Sectional Poisson-Voronoi tessellation is almost surely a non-Voronoi cell [25]. For 2D and 3D Poisson-Voronoi diagrams, also for 2D Sectional Poisson-Voronoi diagrams, much information about moments and scaling for the main geometrical characteristics is known, but little information and no analytic expressions for the distributions of them are available so far. In the next Section, we will see how stereological relations can be used to obtain estimates of the intensity parameter λ of the 3D generating Poisson process based on the 2D sections.

STEREOLOGICAL ESTIMATORS FOR THE INTENSITY PARAMETER

Basic stereological relationships exist which are independent of any underlying tessellation model. Moreover, in the literature explicit (scaling) relations are known expressing the expected number of vertices per unit area, P_A, the expected number of cells per unit area, N_A, and the mean total edge length per unit area, L_A, in terms of the intensity parameter λ for a generating 3D Poisson process. Combining stereological and scaling relationships, the following expressions hold, see e.g. [49]:

$$P_A = \frac{8}{15} \cdot \left(\frac{3}{4}\right)^{1/3} \cdot \pi^{5/3} \Gamma\left(\frac{4}{3}\right) \cdot \lambda^{2/3} = c_1 \cdot \lambda^{2/3}$$
$$N_A = \frac{4}{15} \cdot \left(\frac{3}{4}\right)^{1/3} \cdot \pi^{5/3} \Gamma\left(\frac{4}{3}\right) \cdot \lambda^{2/3} = \frac{c_1}{2} \cdot \lambda^{2/3} \text{ and}$$
$$L_A = \pi \cdot \left(\frac{\pi}{6}\right)^{1/3} \cdot \Gamma\left(\frac{5}{3}\right) \cdot \lambda^{1/3} = c_2 \cdot \lambda^{1/3}.$$

Furthermore, exploiting the simple relation between N_A and the expected area of the cell profiles, $\mathbb{E}(a)$, $N_A = \frac{1}{\mathbb{E}(a)}$, four estimators for λ can be obtained:

$$\hat{\lambda}_P = \left(\frac{\hat{P}_A}{c_1}\right)^{3/2} \approx 0.2008 \cdot \hat{P}_A^{3/2}, \; \hat{\lambda}_N = \left(\frac{2\hat{N}_A}{c_1}\right)^{3/2} \approx 0.5680 \cdot \hat{N}_A^{3/2}$$
$$\hat{\lambda}_L = \left(\frac{\hat{L}_A}{c_2}\right)^{3} \approx 0.0837 \cdot \hat{L}_A^{3}, \; \hat{\lambda}_a = \left(\frac{2}{c_1 \bar{a}}\right)^{3/2} \approx 0.5680 \cdot \bar{a}^{-3/2}. \tag{3.2.1}$$

Here, the hats indicate natural estimates for the mean quantities based on the data (like 'number of cells divided by observed area', $\hat{N}_A$). In [49], the behaviour of the estimators is investigated by means of a computer simulation. The authors state that the estimators show hardly any difference concerning bias and variance and that the biases are less than 1% for sample size $n = 50$ and that they decrease rapidly with increasing sample size.
Once we have an estimate of the intensity parameter $\hat{\lambda}$, as explained in Section 2.3 of the previous Chapter, it can be used for estimating the distribution of the main geometrical 3D features of the grains.

3.3. DISTRIBUTION OF THE GEOMETRICAL CHARACTERISTICS

In this Section, we focus on the distribution of the area, the perimeter and the number of edges of cells in 2D Sectional Voronoi diagrams, considering two cases: periodic and non periodic boundary conditions.

PERIODIC BOUNDARY CONDITIONS

Before going more deeply into the testing problem, it is necessary to make a distinction between periodic and non periodic boundary conditions. On the one hand, periodic boundary conditions, resulting from the application of translation symmetries, are mathematically convenient as these provide a natural way to deal with edge effects.

Moreover, for large volumes and large values of λ, the construction really mimics the infinite volume situation where the convenient scaling results as mentioned in Section 3.2. For real materials, the periodic boundary constraint is not realistic. The approach without periodic boundary conditions is more realistic. It will be seen that determining null distributions of test statistics, the approach will be slightly more simulation based, but also more tailored to the data and 3D object at hand. For both simulation studies a Monte-Carlo procedure is used. In particular, in the periodic boundary case, the results are obtained by randomly generating approximately 1 000 points in a box of dimension $10 \times 10 \times 10$ and using Eq. 2.2.1 in Chapter 2 for creating 3D Poisson-Voronoi cells. This is equivalent to saying that the generator points of the Poisson-Voronoi diagram are generated according to a Poisson process with intensity parameter $\lambda = 1$. Then, one section with dimensions 10×10 (parallel to the cube face for reducing boundary effect) for every 3D structure is randomly taken. On average the number of 2D cells in a section turns out to be approximately 146. The simulation is conducted using the software provided by Tata Steel. The algorithm, that the software exploits is described in Section 2.4 of the previous Chapter 2. The procedure consists in repeating 1 000 000 three main steps:

Step 1 : Generate a 3D Poisson-Voronoi diagram with intensity parameter $\lambda = 1$ applying periodic boundary conditions;

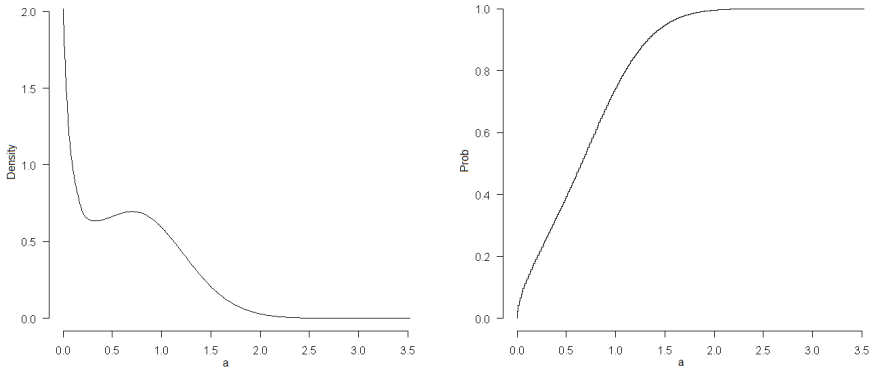
Step 2 : Take a random 2D section of the 3D structure;

Step 3 : Determine the geometrical characteristics of all cells in the 2D section.

Graphical representations of the results are shown in Figures 3.1, 3.2, 3.3. For the grain area and the grain perimeter distributions estimation; a simple boundary correction for kernel density estimation is adopted [67]. Quantities like area and perimeter are by definition nonnegative. This means that in general the probability density functions of these quantities have a discontinuity at zero. Kernel estimators are biased at such points of discontinuity and can be corrected for bias using boundary corrected estimate described in [67]. The linear correction approach, as proposed in [67] (see Equation 3.4 [67]), prevents the estimate to assign mass outside $[0, \infty)$.
The values in Table 3.1 are the estimated values of the main geometrical features for a 2D Sectional Poisson-Voronoi diagram. They are in agreement with both theoretical and simulation results known in the literature (see [103]).

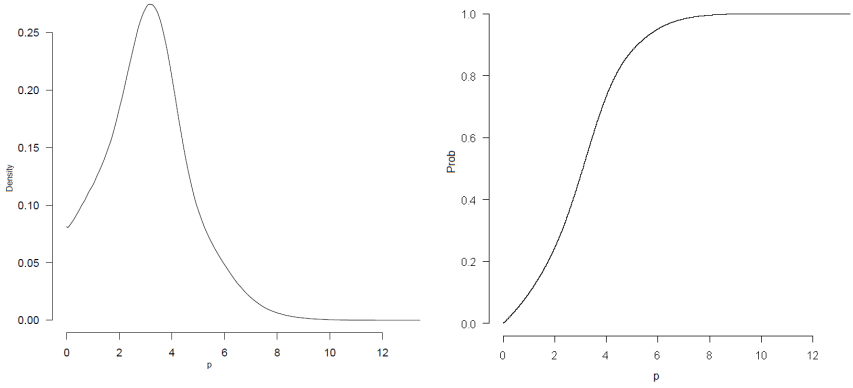
Table 3.1: Estimated moments of the geometrical features of 36 480 600 2D sectional cells, $\lambda = 1$

(a) *Area*		(b) *Perimeter*		(c) *Number of edges*	
μ_1	0.68524	μ_1	3.13345	μ_1	6.00000
σ	0.47342	σ	1.60552	σ	1.69195
μ_2	0.69367	μ_2	12.39622	μ_2	38.86268
μ_3	30.37169	μ_3	2072.73503	μ_3	9818.30810
μ_4	40.94590	μ_4	10695.17596	μ_4	72107.17324



(a) (b)

Figure 3.1: (a) Boundary corrected Kernel density estimate (Epanechnikov kernel, linear combination correction, $h = 0.2$ [67]) and (b) empirical cumulative distribution function of the area of 36 480 600 (originating from the 1 000 000 slices with periodic boundary conditions) 2D sectional cells, $\lambda = 1$

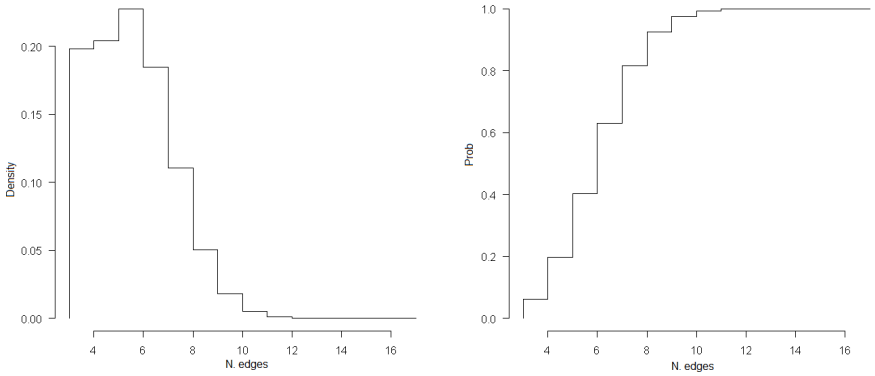


(a) (b)

Figure 3.2: (a) Boundary corrected Kernel density estimate (Epanechnikov kernel, linear combination correction, $h = 0.1$ [67]) and (b) empirical cumulative distribution function of the perimeter of 36 480 600 (originating from the 1 000 000 slices with periodic boundary conditions) 2D sectional cells, $\lambda = 1$

NON PERIODIC BOUNDARY CONDITIONS

In most real situations, the data available are relative to a material section with completely visible as well as partially visible grains. In such situations it is not realistic to use periodic boundary conditions in the model. The second simulation study does not



(a) (b)

Figure 3.3: (a) Relative frequencies and (b) empirical cumulative distribution function of the number of edges of 36 480 600 (originating from the 1 000 000 slices with periodic boundary conditions) 2D sectional cells, $\lambda = 1$

involve periodicity in the boundaries. We fix the geometry of the 3D volume and 2D slice as in the periodic boundaries case. Then the procedure can be summarised repeating 1 000 000 times three main steps:

Step 1 : Generate a 3D Poisson-Voronoi diagram with intensity parameter λ not applying periodic boundary conditions. In this Chapter, for reasons that will become clear later, $\lambda = 0.2$ is chosen;

Step 2 : Take a random 2D section of the 3D structure;

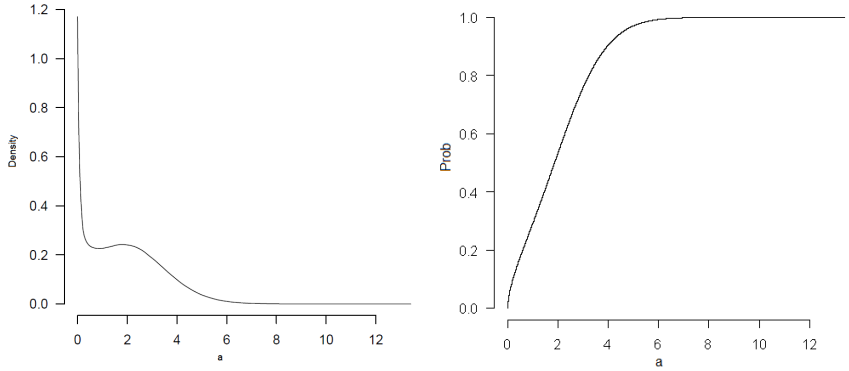
Step 3 : Determine the geometrical characteristics of the completely visible and the partially visible cells in the 2D section.

The main graphical results for the area and the perimeter are shown respectively in Figures 3.4, 3.5.

The shape of the distributions seems to be similar to the periodic boundary case (Figures 3.4, 3.5). The distribution of the number of edges is the one that differs the most in the two boundary type cases (Figures 3.3, 3.6). Note that the scale is different given that two different values of λ are considered for the two different approaches. The values in Table 3.2 are the estimated values of the main geometrical features for a 2D Sectional Poisson-Voronoi diagram with non periodic boundary conditions.

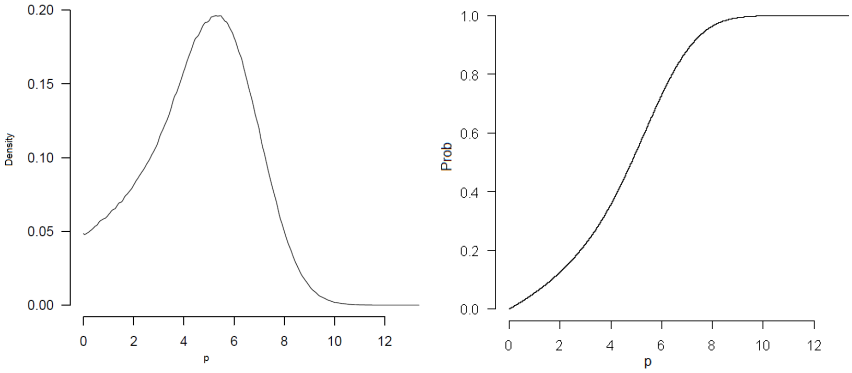
3.4. MODEL TESTS

In [50, 73, 131] several model tests based on the distribution of geometrical features of the grains in random plane sections of a spatial tessellation are proposed. More precisely in [73], the authors propose five stereological model tests based on the distribution of the number of cell vertices. The power of the model tests is investigated under



(a) (b)

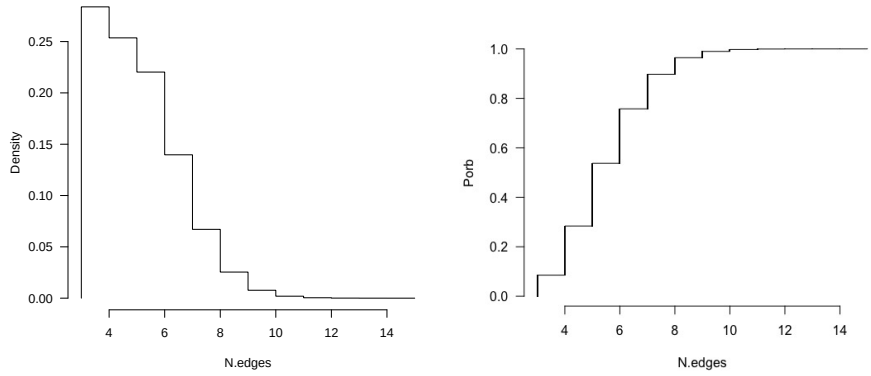
Figure 3.4: (a) Boundary corrected Kernel density estimate (Epanechnikov kernel, linear combination correction, $h = 0.1$ [67]) and (b) empirical cumulative distribution function of the area of 500 000 (originating from the 10 000 slices with non periodic boundary conditions) 2D sectional cells, $\lambda = 0.2$



(a) (b)

Figure 3.5: (a) Boundary corrected Kernel density estimate (Epanechnikov kernel, linear combination correction, $h = 0.1$ [67]) and (b) empirical cumulative distribution function of the perimeter of 500 000 (originating from the 10 000 slices with non periodic boundary conditions) 2D sectional cells, $\lambda = 0.2$

some special parametric alternative hypotheses: a Matérn cluster point process (CVT), a Matérn hard-core point process (HVT) and a simple sequential inhibition point process (SVT). Secondly, in [50] three different model tests are considered: the first two are based on the variability of the section cells area, the third is motivated by a well-known relationship between specific edge length L_A and point process intensities λ and P_A. In line with their previous work, the authors propose one-sided and two-sided tests for dis-



(a) (b)

Figure 3.6: (a) Relative frequencies and (b) empirical cumulative distribution function of the number of 500 000 (originating from the 10 000 slices with non periodic boundary conditions) 2D sectional cells, $\lambda = 0.2$

Table 3.2: Estimated moments of the geometrical features of 500 000 (originating from the 10 000 slices with non periodic boundary conditions) 2D sectional cells, $\lambda = 0.2$

(a) *Area*		(b) *Perimeter*		(c) *Number of edges*	
μ_1	1.99999	μ_1	4.63812	μ_1	5.48690
σ	1.42733	σ	2.03771	σ	1.54197
μ_2	6.03722	μ_2	25.66439	μ_2	32.48377
μ_3	63.81772	μ_3	451.25743	μ_3	597.41117
μ_4	266.05660	μ_4	2921.12340	μ_4	4039.34983

tinguishing Poisson-Voronoi tessellation from more regular tessellations (HVT and SVT) or irregular tessellations (CVT). The null distributions of the test statistics are approximated using simulation. Simulations also show that the model tests are quite powerful in discriminating the different kind of plane sections. It is interesting to note that all their tests are based on summarising indices like the coefficient of variation, skewness index etc, and that the best behaviour among them is reported to be the one based on the coefficient of variation of the cells area (Eq. 3.4.1), also used by the authors in [131].
In this Section we introduce test statistics that use more information contained in the data than only summarising indices. To this end, we use tools belonging to different branches in statistics. Moreover, we describe a partly simulation-based framework to approximate null distributions of the test statistics considered.
If it comes to the study of mechanical properties of metal, the grain size is known to be an important parameter. In 2D, grain area therefore represents one of the most interesting features for real materials sections, especially for single-phase materials [55]. Therefore, the first two tests proposed are based on observed cell areas. The first one,

mentioned before and already used in [50, 131], is based on the coefficient of variation of the observed cell areas:

$$C = \frac{\sqrt{\frac{1}{n-1}\sum_{i=1}^{n}(a_i - \bar{a})^2}}{\bar{a}}. \tag{3.4.1}$$

Here a_i is the area of the i-th sectional cell and $\bar{a}$ is the mean cell area in the section. As the coefficient of variation is scale invariant, one just needs to compute the coefficient of variation of the area of the cells of a real section applying periodic boundary conditions and compare it with the quantile of the distribution of this test statistic. Its counterpart, in the non periodic boundary case, is based on the coefficient of variation of the area of the totally and partially visible cells. Obviously, the referring quantile of the distribution of the statistical test are different with respect to the previous case.
In both cases, the information contained in the 2D section is clearly related to the number of cells observed (n) and comparing the observed value of C with a quantile of the conditional distribution of C given n will only depend on the number of cells observed in the 2D section.
The second test is based on the cumulative distribution function (CDF) of the area of the 2D sectional cells. More precisely it is a Kolmogorov-Smirnov type test given by the supremum distance between the CDF of the area of the cells of the section for which one wants to test the Poisson-Voronoi hypothesis and a function that reflects our expectation of the cumulative distribution function under the Poisson-Voronoi assumption. For the latter, in the periodic boundaries case, we choose a very accurate simulation-based approximation of the CDF of the area of 36 480 600 Sectional Poisson-Voronoi cells.
Let F_1 be the cumulative distribution function of the areas of the 2D sectional cells with intensity parameter $\lambda = 1$ approximated via simulation as described above and let $\hat{G}$ be the empirical cumulative distribution function of the area of n cells of a 2D section from a 3D structure with intensity parameter λ. First, we use eq. 3.2.1 for estimating the intensity based on the considered section, $\hat{\lambda}_a$. Furthermore, inspired by Lemma 2.3.3 in the previous Chapter, we define the next test statistic as the supremum distance between the two functions:

$$D(F, \hat{G}) = \sup_{x \geq 0} |F_1(x) - \hat{G}(\hat{\lambda}^{\frac{2}{3}} x)|. \tag{3.4.2}$$

We will return to the issue of approximating the null distribution of this test statistic in Section 3.5.
In the non periodic boundaries case, the formulation is slightly different. It is expressed by

$$D(\bar{F}_{\lambda\, n_{2D}}, \hat{G}_{n_{2D}}) = \sup_{x \geq 0} |\bar{F}_{\lambda\, n_{2D}}(x) - \hat{G}_{n_{2D}}(x)| \tag{3.4.3}$$

where $\bar{F}_{\lambda\, n_{2D}}$ is the expected CDF conditioned to the event of observing exactly n_{2D} sectional cells with estimated parameter λ. In Section 3.5, it will be explained in more detail how this can be computed. $\hat{G}_{n_{2D}}$ is the empirical CDF of the areas of the totally and partially visible cells of the section under study.
The last test exploits tools coming from the emergent field of Topological Data Analysis. We will now explain the main concepts of persistence homology necessary for using our model test.

TEST BASED ON PERSISTENCE PLOTS

Instead of giving rigid mathematical and topological definitions, the aim of this Section is to guide the reader via intuitive concepts in the construction of persistence diagrams and persistence landscapes used for the last model test. Looking at a single 2D image, it is hard to identify the really 'important' features that univocally characterise it. Topological data analysis (TDA) is a relatively new discipline that has provided new insight into the study of qualitative features of data. In particular, persistent homology is the branch of TDA that provides tools both for identifying qualitative features of data and to give a measure of the importance of those features. Key topological features of a set include connected components, holes, voids .... The main aim of persistent homology is to record the evolution of those characteristics with respect to a scale parameter r that usually can be interpreted as time.

To avoid too long digressions that can drift away from the real scope of the Chapter, most of the main concepts belonging to homology and persistent homology field are just concisely discussed. For readers that aim to come to a formal definition of the following procedure, in [53] more details are provided.

For illustrative reasons and because in this study 2D images are used, the 2D case is considered but generalisation to higher dimensions is not complicated. The input of the analysis typically takes the form of a point cloud $\mathbf{X}$ (Fig. 3.7 (a)). Based on that, a special structure is built. It provides information about the qualitative features discussed above. This structure is based on so called simplices. A geometric k-simplex is the convex hull of $k+1$ affinely independent points $v_0, v_1, \ldots, v_k$. More precisely the 0-simplex identifies vertices, the 1-simplex line segments and the 2-simplex triangles. One way for building this structure starts off with the so called Delaunay Triangulation, $DT(\mathbf{X})$ of $\mathbf{X}$. Basically, this is a graph consisting of vertices in $\mathbf{X}$ and edges between two points if and only if they share a Voronoi edge (Fig. 3.7 (b)). Then, circles are grown with increasing radius r, centred at the points in $\mathbf{X}$. The Alpha complex[1] at radius r, $\alpha_r(\mathbf{X})$, is a subcomplex of $DT(\mathbf{X})$. In fact, for r very small, the Alpha complex is nothing but the set $\mathbf{X}$ of the generator points. Then r grows and once two circles intersect, the edge of the underlying Delaunay triangulation between the two circle centres is added to $\alpha_r(\mathbf{X})$. Eventually, for r very big, the Alpha complex is the Delaunay Triangulation itself (Fig. 3.7 (c-i)).

Now, rather than considering this structure for some fixed value of r, its evolution for growing $r > 0$ is registered. In particular, we keep track of the birth time b and a death time d of connected components and holes[2], where the 'time' is given by the radius of the circles corresponding to those events. One can think of the circles radii growing at constant rate. At time zero, the Alpha complex equals $\mathbf{X}$. All individual points are separate connected components. These are born at time zero. After some time, when the first two points get connected because their circles touch, one can say two connected components merge or one connected component 'dies' (in a more general case in which the birth times might be different the edge that causes two components to merge is paired with the component that was born most recently, i.e. the one with the later birth 'time'). In Figure 3.7, this happens for $r = 0.47$; see subplot 3.7 (c). For one connected com-

[1] Other common choices of simplicial complexes are Čech and Rips complexes; see [33, 53].

[2] In three dimensions one could also consider other topological features, like voids or cavities (holes in more than 2 dimensions)

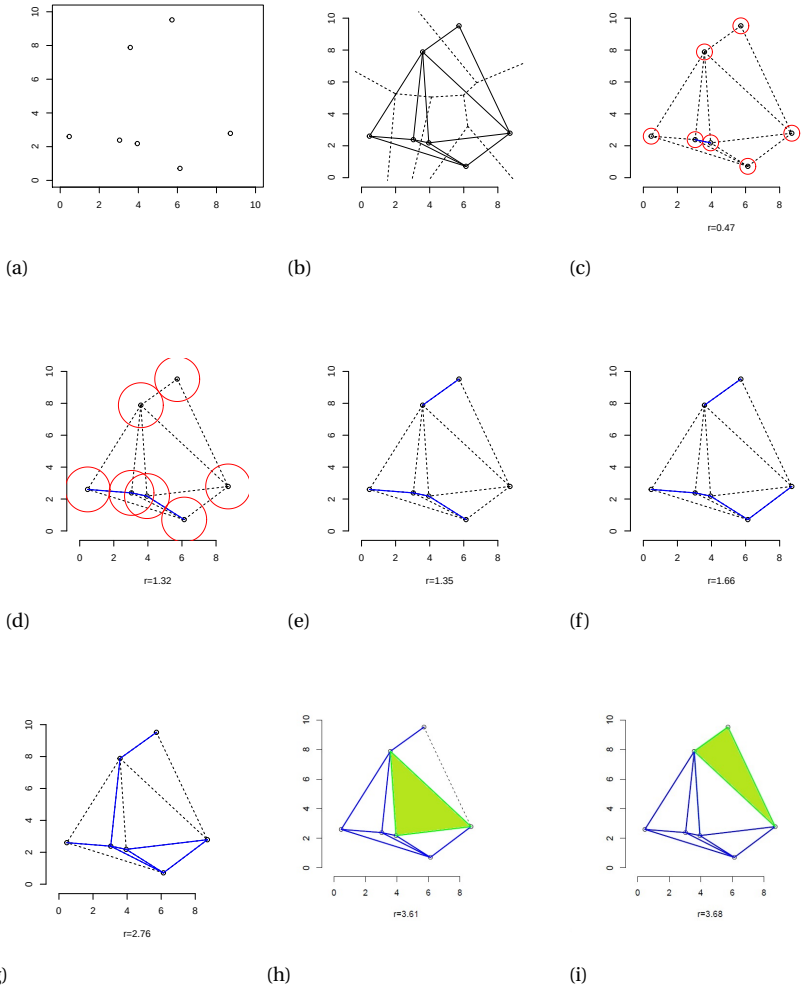
ponent, we therefore have $(b,d) = (0, 0.47)$. Increasing r further, more connected components will 'die' until only one remains for all r large enough because all points are covered by the union of all large circles. During the same process, it is also possible that holes appear. This happens when a polygon (eg. triangle) appears in the picture, such that the r-circles around the corner points of this polygon do not cover the whole polygon. At this time a hole is 'born', yielding a birth time b for this feature. It will also 'die' again, when r is further increased and the circles centered at the corners do cover the whole polygon. Note that not all polygons that appear correspond to the birth of a hole. For instance, in the case of triangles, acute triangles always generate a hole while obtuse triangles not. in Figure 3.8 (g) a triangle appears but the circles centred at the three corners immediately cover the whole triangle.
The points (b,d) thus obtained can be used as coordinates and plotted on a plane, resulting in the so called persistence diagram. Since the topological features (connected components, holes) can only die 'after' they are born ($d \geq b$), necessarily each point appears on or above the diagonal line $y = x$. The persistence diagram corresponding to the data in Figure 3.7 is shown in Figure 3.8. The black dots, D_{0i}, on the vertical axis represent the 'deaths' of connected components; the lowest being the aforementioned $(b,d) = (0, 0.47)$, the highest, $(b,d) = (0, 2.67)$, corresponding to Figure 3.7 (g). The red triangles D_{1i}, represent the birth- and death times of the holes. Based on persistence diagrams, several descriptive summarising functions have been proposed in the literature. For example rank functions [121], landscapes and silhouettes [20, 24] and accumulated persistence functions [15]. In this Chapter we follow the persistence landscapes approach, but any other summary statistic could also be used for testing.
We first describe in words how to construct a landscape from a persistence diagram. Then, the formal definition follows. For each point (b,d) in the persistence diagram, count the number of points to its left top (north-west). This is the rank of the point (b,d) and it can be interpreted as the number of features that are alive at time b and that are still alive at time d. Then, draw horizontal and vertical lines from each point (b,d) in the persistence diagram to the diagonal and 'tip the diagram on its side'. Then take the contour of the projection of the points with the same rank. This results in the so-called landscape. This is done for connected components and holes separately, see Figure 3.9.
More formally, a persistence landscape is a sequence of continuous, piecewise linear functions $\lambda(k,\cdot) : \mathbb{R}^+ \to \mathbb{R}^+,\ k = 1, 2, \ldots$. Denote the set of 'persistence points' in the persistence diagram by D. Then for each $p = (b,d) \in D$ define the triangular functions

$$\Lambda_p(t) = \begin{cases} t-b & t \in [b, \frac{b+d}{2}] \\ d-t & t \in (\frac{b+d}{2}, d] \\ 0 & otherwise. \end{cases}$$

Then, the persistence landscape of the persistence diagram is defined by

$$\lambda_D(k,t) = \text{kmax}_{p \in D} \Lambda_p(t), \quad t \geq 0,\ k \in \mathbb{N}. \tag{3.4.4}$$

Here kmax selects the kth largest value in the set, so for a particular k at each t, $\lambda_D(1,t)$ is the largest value in the set $\{\Lambda_1(t), \Lambda_2(t), \ldots, \Lambda_p(t)\}, p \in D$, $\lambda_D(2,t)$ the second largest value, etc.
Our test will be the contrast between the observed landscape and a landscape one would



(a) (b) (c)

(d) (e) (f)

(g) (h) (i)

Figure 3.7: (a) Set of points $\mathbf{X}$ (b) Voronoi Diagram (dashed) and Delaunay Triangulation (solid) (c) Circles with radius 0.47 around the points of $\mathbf{X}$; the Alpha complex $\alpha_r(\mathbf{X})$ consists of the individual points of $\mathbf{X}$ and the one edge corresponding to the two touching circles (d) Alpha complex for $r = 1.32$ (e) Alpha complex, $r = 1.35$ (f) Alpha complex, $r = 1.66$ (g) Alpha complex, $r = 2.76$ (h) Alpha complex, $r = 3.61$ (i) Alpha complex, $r = 3.68$

expect under the null hypothesis that the 3D structure is Poisson-Voronoi. For this mean landscape, we use the conditional expectation of the landscape given that $N_{2D} = n_{2D}$ and approximate this using the simulation procedure described in Section 3.3. To be more specific,

$$\bar{\lambda}_{D_j}(k,t) = \frac{1}{n}\sum_{i=1}^{n} \lambda_{D_j(i)}(k,t) \;\; j = 0,1, \;\; t \geq 0, \tag{3.4.5}$$

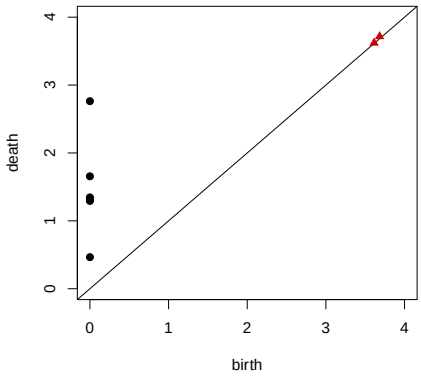


Figure 3.8: Persistence Diagram. The black dots indicate the birth- and death time of connected components and the red triangles the birth- and death times of the holes. The data are the same as those used for Figure 3.7.

where n is the number of 2D Poisson-Voronoi sections generated with $N_{2D} = n_{2D}$. Inspired by the approach proposed in [121], the test statistics are then given by the distance between persistence landscapes and mean persistence landscapes using L^2 norm,

$$\begin{aligned} L_0 &= \|\hat{\lambda}_{D_0} - \bar{\lambda}_{D_0}\|_2 = \Big[\sum_{k=1}^{n_{2D}-1} \int_0^T (\hat{\lambda}_{D_0}(k,t) - \bar{\lambda}_{D_0}(k,t))^2 \mathrm{d}t\Big]^{\frac{1}{2}} \\ L_1 &= \|\hat{\lambda}_{D_1} - \bar{\lambda}_{D_1}\|_2 = \Big[\sum_{k=1}^{\infty} \int_0^T (\hat{\lambda}_{D_1}(k,t) - \bar{\lambda}_{D_1}(k,t))^2 \mathrm{d}t\Big]^{\frac{1}{2}}. \end{aligned} \tag{3.4.6}$$

Here $\hat{\lambda}_{D_j}(k,\cdot),\ j = 0,1$ is the k-th landscape for the connected components ($j = 0$) and for the holes ($j = 1$) for the 2D section under study. If both L_0 and L_1 are less than the threshold quantiles, the Poisson-Voronoi hypothesis is not rejected.

3.5. QUANTILES OF THE MODEL TESTS

In [50], the authors carry out a simulation for estimating the quantiles of the test statistics proposed there. Cells of 3D spatial Poisson-Voronoi diagrams are generated with $\lambda = 1$. Then, a random planar section of the 3D structure is taken and square observation windows are drawn in the section planes with an expected number of 50, 100, 150 and 200 cells, respectively.

We provide an expression for the distribution of any test statistic given the number of observed cells in the section, separating a part that depends on the parameter λ and a part that does not. We consider the situation where we see a window (with known shape and size) of a $2D$ planar section of a $3D$ Poisson-Voronoi diagram in a $3D$ object of known geometry. As before, denote by N_{3D} the number of cells in the $3D$ object and N_{2D} the number of $2D$ cells visible in the $2D$ window. Lemma 3.5.1 below gives an expression

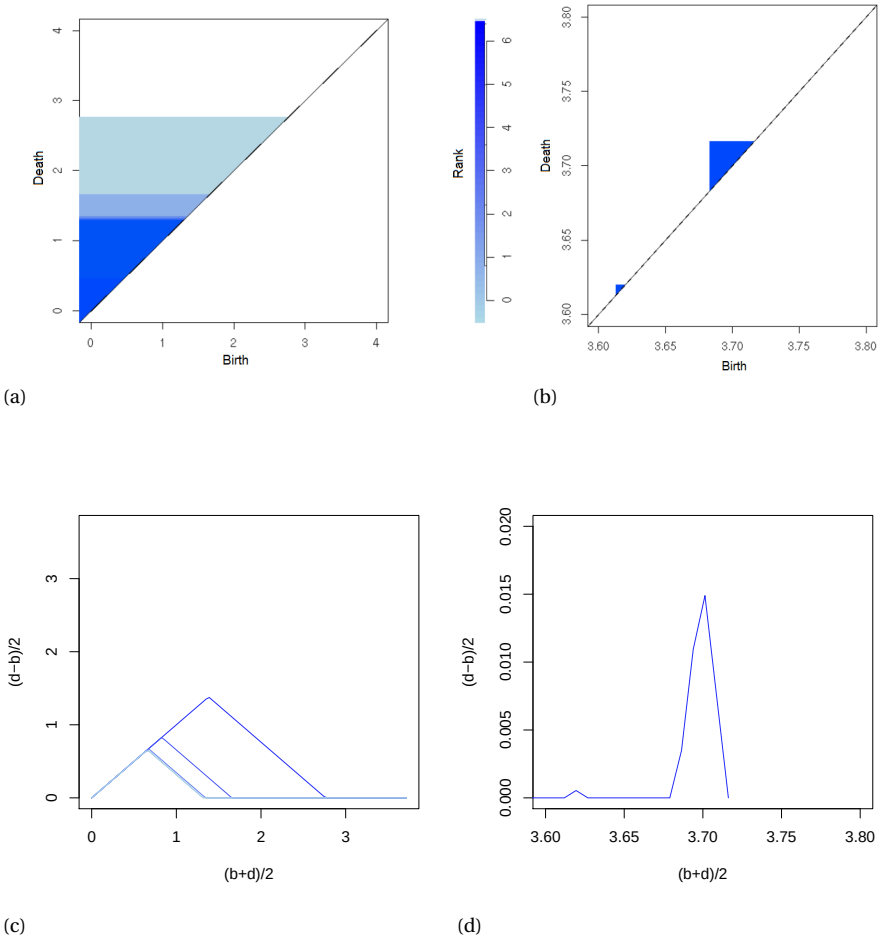


Figure 3.9: Rank function for connected components (a) and holes (b) Persistence Landscapes for connected components (c) and holes (d)

of the null distribution of a test statistic T, given n_{2D} cells are observed in the section. It separates a part that depends on the intensity parameter λ and a part that does not.

Lemma 3.5.1. *Let T denote a general model test for the Poisson-Voronoi assumption validation. The conditional probability $\mathrm{P}_\lambda(T \geq t | N_{2D} = n_{2D})$ can be expressed as*

$$\mathrm{P}_\lambda(T \geq t | N_{2D} = n_{2D}) = \frac{\sum_{k=n_{2D}}^{\infty} \mathrm{P}(T \geq t | N_{3D} = k, N_{2D} = n_{2D}) \, \mathrm{P}(N_{2D} = n_{2D} | N_{3D} = k) \, \frac{(\lambda \mathcal{V})^k}{k!}}{\sum_{j=n_{2D}}^{\infty} \mathrm{P}(N_{2D} = n_{2D} | N_{3D} = j) \, \frac{(\lambda \mathcal{V})^j}{j!}} \tag{3.5.1}$$

Proof.

$$\begin{aligned} \mathrm{P}_\lambda(T \geq t | N_{2D} = n_{2D}) &= \sum_{k=0}^{\infty} \mathrm{P}_\lambda(T \geq t, N_{3D} = k | N_{2D} = n_{2D}) \\ &= \sum_{k=n_{2D}}^{\infty} \mathrm{P}_\lambda(T \geq t, N_{3D} = k | N_{2D} = n_{2D}) \\ &= \sum_{k=n_{2D}}^{\infty} \mathrm{P}_\lambda(T \geq t | N_{3D} = k, N_{2D} = n_{2D}) \mathrm{P}_\lambda(N_{3D} = k | N_{2D} = n_{2D}) \\ &= \sum_{k=n_{2D}}^{\infty} \mathrm{P}(T \geq t | N_{3D} = k, N_{2D} = n_{2D}) \mathrm{P}_\lambda(N_{3D} = k | N_{2D} = n_{2D}). \end{aligned} \tag{3.5.2}$$

In the last equality the λ-dependence disappears from the first factor, because, conditionally on N_{3D}, the distribution of T does not depend on λ. The λ-dependent part in Eq. 3.5.2 can be made more explicit also using that conditionally on N_{3D}, the distribution of N_{2D} does not depend on λ:

$$\begin{aligned} \mathrm{P}_\lambda(N_{3D} = k | N_{2D} = n_{2D}) &= \frac{\mathrm{P}(N_{2D} = n_{2D} | N_{3D} = k) \mathrm{P}_\lambda(N_{3D} = k)}{\mathrm{P}_\lambda(N_{2D} = n_{2D})} \\ &= \frac{\mathrm{P}(N_{2D} = n_{2D} | N_{3D} = k) \mathrm{P}_\lambda(N_{3D} = k)}{\sum_{j=n_{2D}}^{\infty} \mathrm{P}(N_{2D} = n_{2D} | N_{3D} = j) \mathrm{P}_\lambda(N_{3D} = j)} \\ &= \frac{\mathrm{P}(N_{2D} = n_{2D} | N_{3D} = k) \frac{(\lambda \mathcal{V})^k}{k!}}{\sum_{j=n_{2D}}^{\infty} \mathrm{P}(N_{2D} = n_{2D} | N_{3D} = j) \frac{(\lambda \mathcal{V})^j}{j!}}. \end{aligned} \tag{3.5.3}$$

Combining Eqs. 3.5.2 and 3.5.3 yields Eq. 3.5.1. □

For computing p-values in practice, the value of λ is needed. In order to take into account the uncertainty in the estimate of λ while computing p-values for model tests, we compute a 90% confidence interval for λ. To do this, as this value is not known, we propose a bootstrap approach. More precisely, we want to compute

$$\begin{aligned} \mathrm{P}_\lambda(\sqrt{\hat{\lambda}} - \sqrt{\lambda} \leq u) &= \sum_{k=0}^{\infty} \mathrm{P}_\lambda(\sqrt{\hat{\lambda}} - \sqrt{\lambda} \leq u, N_{3D} = k) \\ &= \sum_{k=0}^{\infty} \mathrm{P}_\lambda(\sqrt{\hat{\lambda}} - \sqrt{\lambda} \leq u | N_{3D} = k) \mathrm{P}_\lambda(N_{3D} = k) \end{aligned} \tag{3.5.4}$$

The procedure can be summarised as follows: first we estimate λ from a real 2D image, using $\hat{\lambda}_a$ (eq. 3.2.1). For computing $\mathrm{P}_\lambda(N_{3D} = k)$, $\mathrm{P}_{\hat{\lambda}_a}(N_{3D} = k)$ is then used. Secondly, for computing $\mathrm{P}_\lambda(\sqrt{\hat{\lambda}} - \sqrt{\lambda} \leq u | N_{3D} = k)$, 10 000 Poisson-Voronoi diagrams for each realisation of a Poisson process with $\hat{\lambda}_a$ in a cube are generated. Then a 2D section from each 3D diagram is randomly taken and the number of cells in the section is used for estimating λ. Next, the probability of having exactly k cells in 3D, $\mathrm{P}(N_{3D} = k)$, is used as weight for computing a weighted mean cumulative distribution function. Finally, a square root transformation for normalising and stabilising the variance is used for computing the confidence set [126]:

$$P[\sqrt{\hat{\lambda}} - l_{0.95} \leq \sqrt{\lambda} \leq \sqrt{\hat{\lambda}} - l_{0.05}] \approx 0.90 \tag{3.5.5}$$

As an example, if $\hat{\lambda}_a = 0.2$ (as in the application shown in Section 3.7 $n_{2D} = 50$ and window size= 10×10), the resulting 90%-confidence set is given by:

$$[0.1498; 0.2439] \tag{3.5.6}$$

Having a confidence set for λ at hand, the next step is to compute the null distribution described in Lemma 3.5.1 for the various test statistics. A visualisation of the probability of observing exactly 50 cells given $P(N_{3D} = k)$ is shown in Figure 3.10. The resulting p-values depend on λ, but we can consider these for all λ in the confidence set constructed. We start with the coefficient of variation as test statistic (Eq. 3.4.1). In Figure 3.11 it is possible to see the difference between the cumulative distribution functions of the coefficient of variation of the 2D sectional cells area unconditioned and conditioned on seeing exactly 50 cells in the 2D section. Moreover, the green dotted lines represent the cumulative distribution function of the coefficient of variation for the lower and upper bounds of the λ confidence set. Note that the distance between the two CDFs is small, showing that the approach of [50] to use an unconditional distribution in this particular setting leads to comparable results. In table 3.3, quantiles for the conditional distribution of the CV of the cells area are shown ($\hat{\lambda} = 0.2$). In Figure 3.12, the condi-

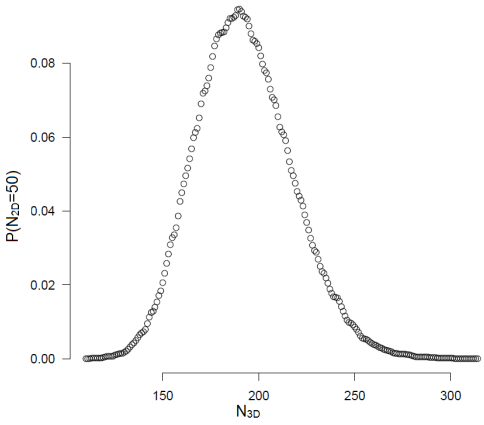


Figure 3.10: Monte Carlo approximation of $P(N_{2D} = 50|N_{3D} = k)$

Table 3.3: Quantiles of the conditional distribution of the coefficient of variation of the 2D sectional cells area given that $N_{2D} = 50$, ($\lambda = 0.2$)

α	0.005	0.01	0.0125	0.025	0.05	0.1	0.9	0.95	0.975	0.9875	0.99	0.995
c_α	0.531	0.547	0.553	0.571	0.591	0.615	0.798	0.826	0.853	0.875	0.883	0.903

tional weighted mean CDF for cells area (black line), its confidence bands (green dotted

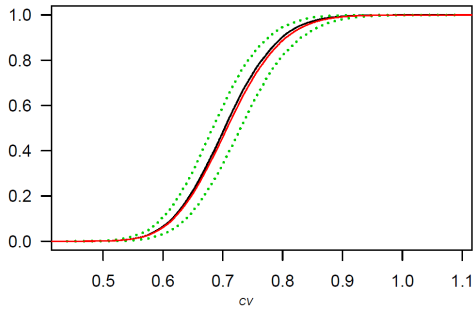


Figure 3.11: Cumulative distribution function of the coefficient of variation of the 2D sectional cells area conditioned on $N_{2D} = 50$ (black line; green dotted lines are obtained using the upper and lower limit of the confidence set for $\hat{\lambda} = 0.2$) and unconditioned (red line)

lines) and the unconditional mean are shown. More precisely we define

$$\begin{aligned}\bar{F}_{\lambda\, n_{2D}}(x) &= \mathbb{E}_\lambda\{F_{N_{2D}}(x)|N_{2D} = n_{2D}\} = \mathbb{E}_\lambda\{\mathbb{E}(F_{N_{2D}}(x)|N_{2D} = n_{2D}, N_{3D})\} \\ &= \sum_{k=n_{2D}}^{\infty} \mathrm{P}_\lambda(N_{3D} = k|N_{2D} = n_{2D}) \cdot \mathbb{E}(F_{N_{2D}=n_{2D},N_{3D}=k}(x)),\end{aligned} \tag{3.5.7}$$

where $F_{N_{2D}=n_{2D},N_{3D}=k}(x)$ is the empirical distribution function of the areas given k cells in $3D$ structure and n_{2D} visible on the slice. The same type of expression is used also for $\bar{\lambda}_{D_0}(1,t)$ and $\bar{\lambda}_{D_1}(1,t)$.
In Figure 3.13 the CDF of the test based on the supremum distance between empirical CDFs of the 2D sectional cells area is shown. As for the test based on coefficient of variation, the difference between conditional and unconditional approach is relatively small. Switching to the test based on persistence landscapes, Fig. 3.14-3.15 are visualisations of k mean persistence landscapes conditioned on $N_{2D} = 50$ for connected components and holes respectively, when $\hat{\lambda} = 0.2$. Instead, Fig. 3.16-3.17 are the conditional maximum weighted means (black lines) and their confidence bands (green dotted lines).
In Figures 3.18-3.19 the CDF of the test based on the L_2 distance between persistence landscapes (connected components and holes) are shown. Also in this case, the difference between conditional and unconditional approach seems to be irrelevant.

For computing the quantiles of the distribution of the model tests based on CDF and on persistence landscape (Tables 3.4, 3.5 and 3.6), we use a 'leave one out' procedure. Here we use the B 2D slices generated as follows:

- For the test based on CDFs difference (3.4.3):

$$d_i = \sup_{x\in\mathbb{R}} |\bar{F}_{\lambda\, n_{2D}(-i)}(x) - \hat{F}_{n_{2D}(i)}(x)|, \quad 1 \le i \le B \tag{3.5.8}$$

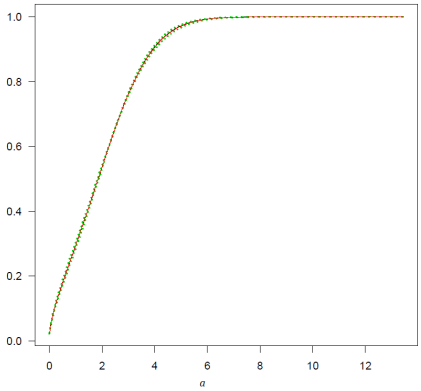


Figure 3.12: Cumulative distribution function of the 2D sectional cells area conditioned on $N_{2D} = 50$ (black line; green dotted lines are obtained using the upper and lower limit of the confidence set for $\hat{\lambda} = 0.2$) and unconditioned (red line)

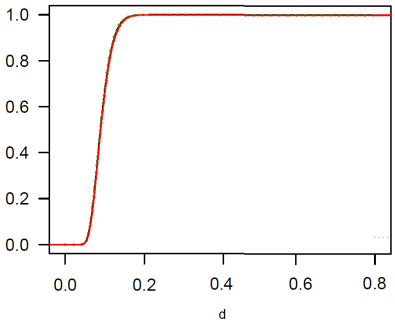


Figure 3.13: Cumulative distribution function of the empirical CDF test of the 2D sectional cells area conditioned on $N_{2D} = 50$ (black line; green dotted lines are obtained using the upper and lower limit of the confidence set for $\hat{\lambda} = 0.2$) and unconditioned (red line)

- For the test based on persistence landscapes difference (3.4.6):

$$\begin{aligned} l_{0(i)} &= \left[\sum_{k=1}^{n_{2D}-1} \int_0^T (\hat{\lambda}_{D_0(i)}(k,t) - \bar{\lambda}_{D_0(-i)}(k,t))^2 \mathrm{dt} \right]^{\frac{1}{2}} \quad 1 \le i \le B \\ l_{1(i)} &= \left[\sum_{k=1}^{\infty} \int_0^T (\hat{\lambda}_{D_1(i)}(k,t) - \bar{\lambda}_{D_1(-i)}(k,t))^2 \mathrm{dt} \right]^{\frac{1}{2}} \quad 1 \le i \le B \end{aligned} \tag{3.5.9}$$

Here $\hat{F}_{n_{2D}(i)}$, $\hat{\lambda}_{D_0(i)}$ and $\hat{\lambda}_{D_1(i)}$ are the empirical results for the section i and $\bar{F}_{n_{2D}(-i)}$, $\bar{\lambda}_{D_0(-i)}$ and $\bar{\lambda}_{D_1(-i)}$ are the mean result computed for all the B sections leaving out the i-th.

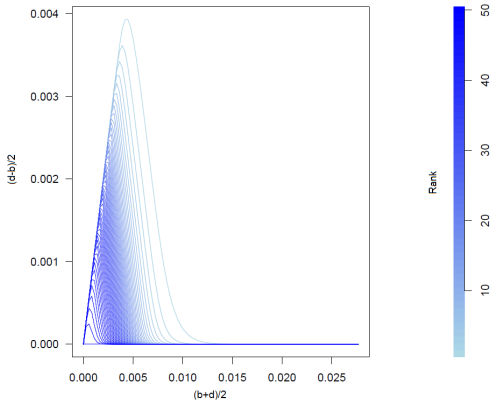


Figure 3.14: k Weighted mean landscapes (connected components) for sections with exactly 50 2D sectional cells, ($\hat{\lambda} = 0.2$)

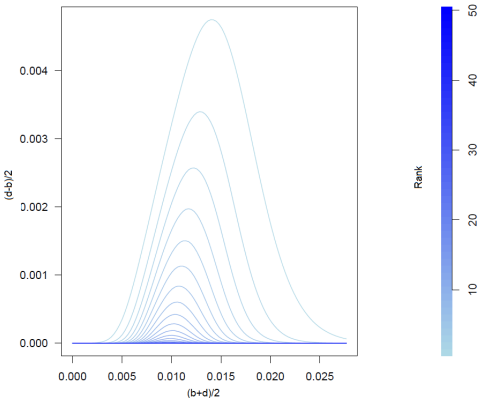


Figure 3.15: k Weighted mean landscapes (holes) for sections with exactly 50 2D sectional cells, ($\hat{\lambda} = 0.2$)

Table 3.4: Quantiles of the conditional distribution of the test based on the difference between cumulative distribution functions of the 2D sectional cells area given that $N_{2D} = 50$, ($\hat{\lambda} = 0.2$)

α	0.005	0.01	0.0125	0.025	0.05	0.1	0.9	0.95	0.975	0.9875	0.99	0.995
d_α	0.047	0.050	0.051	0.054	0.058	0.064	0.123	0.135	0.146	0.155	0.159	0.168

Table 3.5: Quantiles of the conditional distribution of the test based on the difference between the observed landscapes and the conditional mean landscapes (connected components) of the 2D sectional cells area given that $N_{2D} = 50$, ($\hat{\lambda} = 0.2$)

α	0.005	0.01	0.0125	0.025	0.05	0.1	0.9	0.95	0.975	0.9875	0.99	0.995
$l_{0\alpha} \times 10^{-5}$	2.402	2.602	2.802	3.003	3.403	3.803	10	20	20	30	30	40

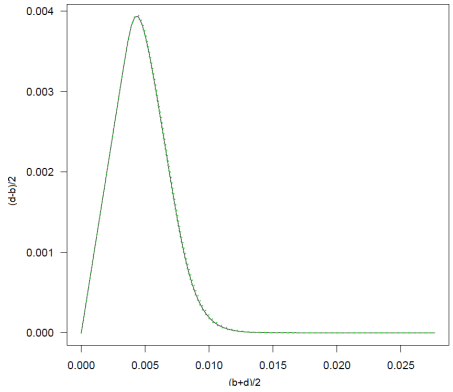


Figure 3.16: Max weighted mean landscape (connected components) for sections with exactly 50 2D sectional cells (black line; green dotted lines are obtained using the upper and lower limit of the confidence set for $\hat{\lambda} = 0.2$)

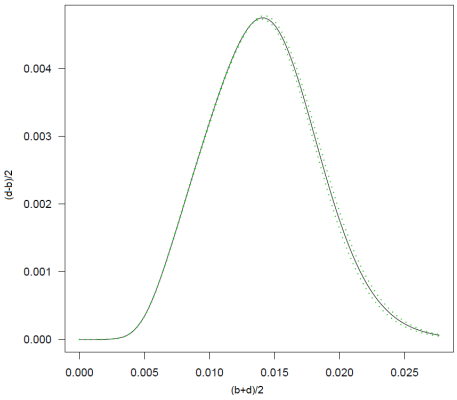


Figure 3.17: Max weighted mean landscape (holes) for sections with exactly 50 2D sectional cells (black line; green dotted lines are obtained using the upper and lower limit of the confidence set for $\hat{\lambda} = 0.2$)

Table 3.6: Quantiles of the conditional distribution of the test based on the difference between the observed landscapes and the conditional mean landscapes (holes) of the 2D sectional cells area given that $N_{2D} = 50$, ($\hat{\lambda} = 0.2$)

α	0.005	0.01	0.0125	0.025	0.05	0.1	0.9	0.95	0.975	0.9875	0.99	0.995
$l_{1\alpha} \times 10^{-5}$	9.109	9.810	9.810	10	10	10	50	70	100	140	150	190

3.6. POWER OF THE MODEL TESTS

To assess the power of the three different tests proposed in Section 3.4, the values of their power functions are estimated under a specific alternative hypothesis: 2D Poisson-Voronoi diagram. As stated in Section 3.2, the authors in [25, 90] showed that a 2D Sec-

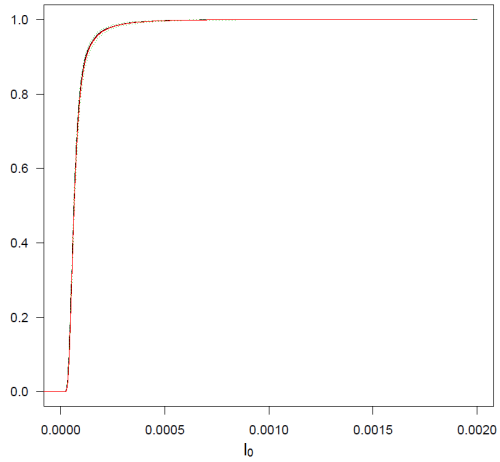


Figure 3.18: Cumulative distribution function of the test based on the L_2 distance between persistence landscapes L_0, (3.4.6), of the 2D sectional cells area conditioned on $N_{2D} = 50$ (black line; green dotted lines are obtained using the upper and lower limit of the confidence set for $\hat{\lambda} = 0.2$) and unconditioned (red line)

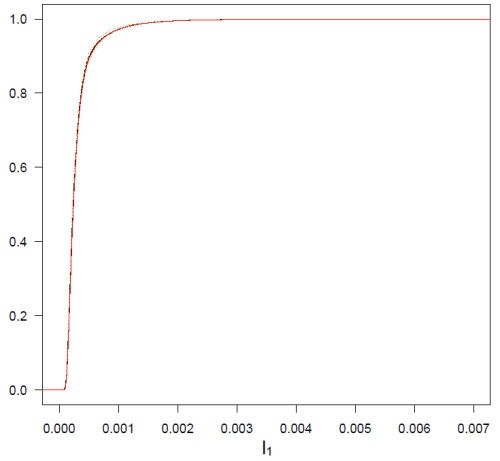
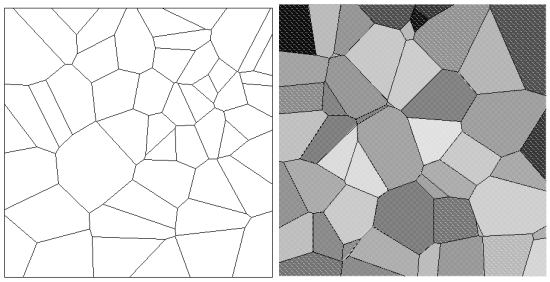


Figure 3.19: Cumulative distribution function of the test based on the L_2 distance between persistence landscapes L_1, (3.4.6), of the 2D sectional cells area conditioned on $N_{2D} = 50$ (black line; green dotted lines are obtained using the upper and lower limit of the confidence set for $\hat{\lambda} = 0.2$) and unconditioned (red line)

tional Poisson-Voronoi diagram cannot be a planar Poisson-Voronoi tessellation. Some mean values of the geometrical characteristics of the sectional diagram clearly deviate from the tessellation resulting from a 2D Poisson point process. Nevertheless, at a first sight the difference between them is not immediate (Figure 3.20).

We generate 7000 2D Poisson-Voronoi diagrams with exactly 50 cells and intensity parameter $\lambda = 0.2$ under non periodic boundary conditions and the main graphical results are shown in Figure 3.21. As the simulations results show, the most powerful test is the one based on the L_2 distance between persistence landscapes. Good results are obtained also for the test based on the empirical CDF difference: its power value is around 90%. The coefficient of variation reaches, however, a considerably lower power 78.6%.

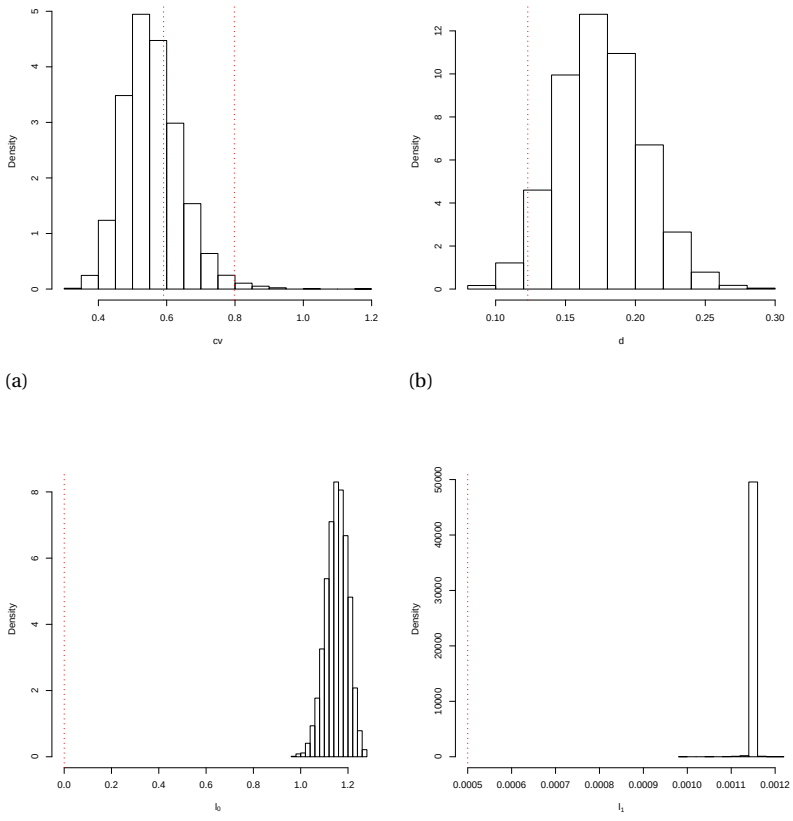


(a) (b)

Figure 3.20: (a) 2D Poisson-Voronoi diagram (b) 2D Sectional Poisson-Voronoi Diagram, $N_{2D} = 50$

3.7. APPLICATION

In [50], it is stated that single-phase microstructures, e.g. alumina ceramics, can be well approximated by Poisson-Voronoi diagrams. Using the same images shown in [50], the tests proposed in the previous Section (Sec. **3.4**) are performed.
First all cells in the images (Fig. 3.22 (a)) are involved in test computations. Hereafter, for illustrative purposes and for a better comparison with the theoretical results shown in the previous Section, we decide to consider just part of the images used in [50]. In fact, the original window size is reduced until exactly 50 cells are visible or partially visible (Fig. 3.22 (b)). In Tables 3.7-3.8, the test statistics and the p values (values in brackets) are shown for the four model tests and following the two different approaches. Figures (3.23-3.27) and (3.28-3.32) are graphical representations of the cumulative distribution function test and the persistence approach steps. In particular, for applying the test based on the difference between persistence landscapes, we take the center of mass of the cells in the images (Fig. 3.24, 3.29), then compute the persistence diagrams (Fig. 3.25,3.30) and finally the persistence landscapes (Fig. 3.26-3.27, 3.31-3.32) as explained in Section 3.4.
Results using the two different approaches lead to slightly different results regarding the first two images (Fig. 3.22 1(a), 1(b), 2(a), 2(b)). For the first image, considering all cells, the coefficient of variation test and the test based on the CDF of cells area suggest that the Poisson-Voronoi model could be reasonably used for approximating alumina ceramics; instead, looking at the cuts, the hypothesis is rejected by both tests. For the second image, the coefficient of variation test based on all cells is in agreement with the results obtained for the reduced sections; just the test based on the CDF considering all cells does not reject the Poisson-Voronoi hypothesis.



(a) (b)

(c) (d)

Figure 3.21: Histograms of the results of the coefficient of variation test (a), of the empirical CDF test (b), of the test based on the L_2 distance between persistence landscape L_0 (c) and L_1 (d) for 7000 2D Poisson-Voronoi diagram. Red dotted lines identify the quantile of the conditional distribution of the test for $N_{2D} = 50$

Using tests from persistence approach instead, the use of Poisson-Voronoi model is discouraged in both cases.

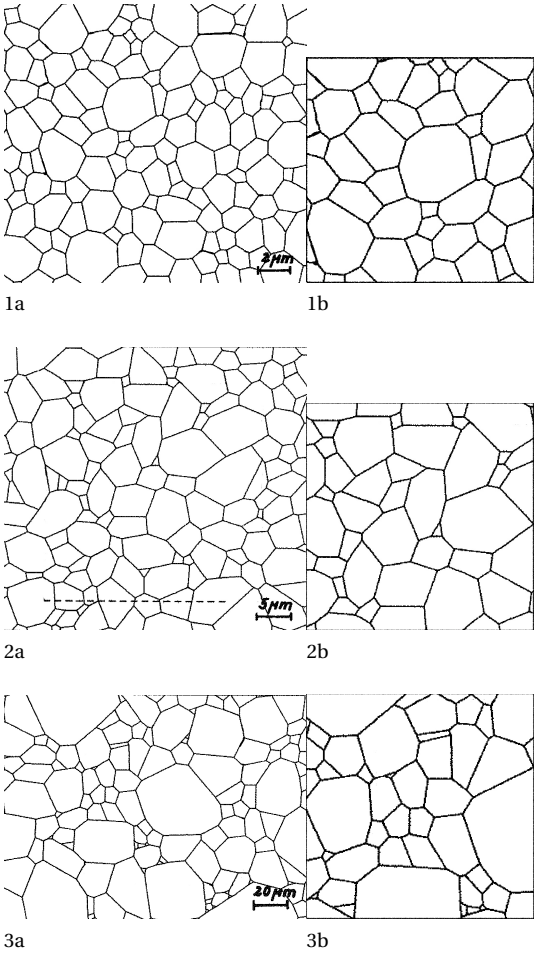


Figure 3.22: Schemes as planar tessellations of plane sections of alumina ceramics: preprocessing (a) Hahn&Lorz ([50]), (b) Cut of the plane sections with exactly 50 cells

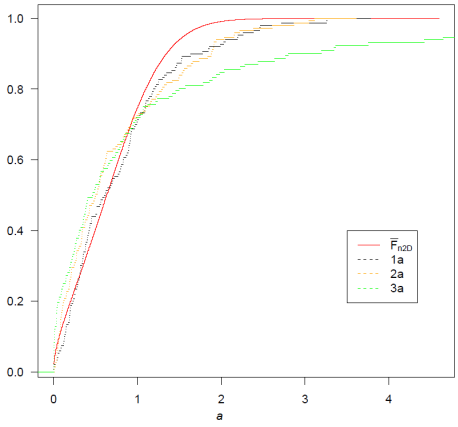


Figure 3.23: Cumulative distribution function comparison of the cells area of the schemes of plane sections of alumina ceramics (Fig.3.22 1 (a) black line, 2 (a) yellow line, 3 (a) green line) and of the 2D Sectional Poisson-Voronoi cells area (red line)

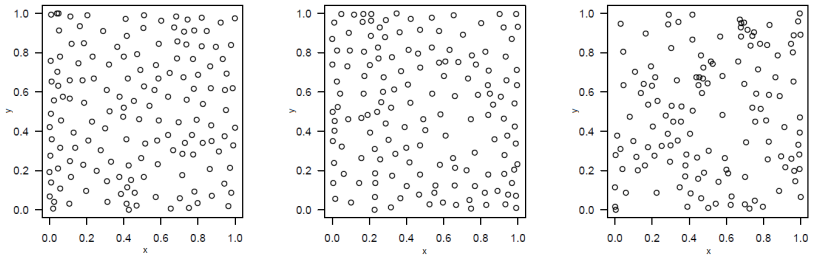


Figure 3.24: From left to right centers of mass of the schemes of plane sections of alumina ceramics (Fig.3.22 1 (a), 2 (a), 3 (a))

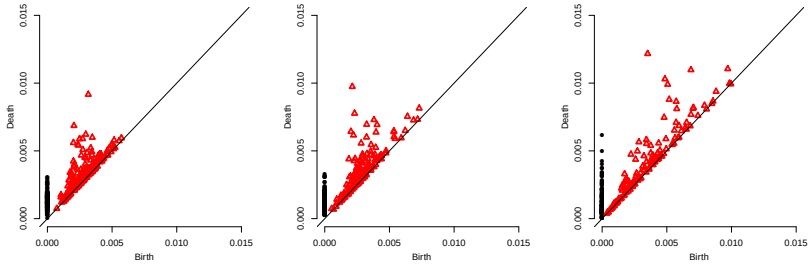


Figure 3.25: From left to right persistence diagrams of the centres of mass of the schemes of plane sections of alumina ceramics (Fig.3.22 1 (a), 2 (a), 3 (a))

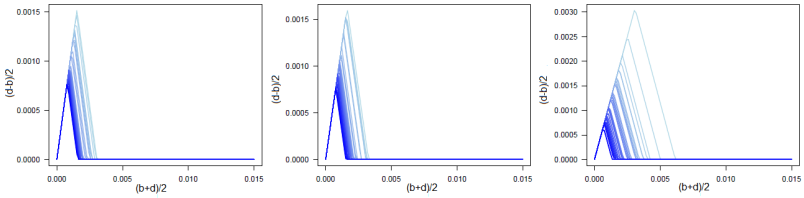


Figure 3.26: From left to right persistence landscapes (connected components) of the schemes of plane sections of alumina ceramics (Fig.3.22 1 (a), 2 (a), 3 (a))

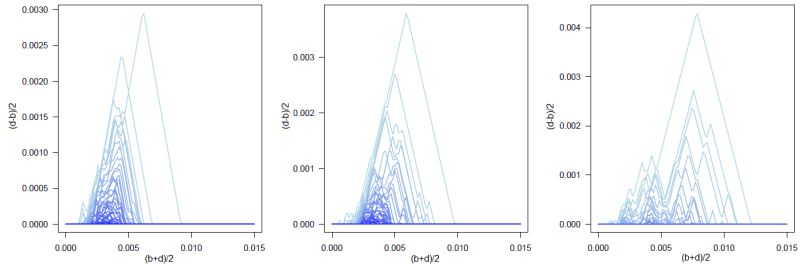


Figure 3.27: From left to right persistence landscapes (holes) of the schemes of plane sections of alumina ceramics (Fig.3.22 1 (a), 2 (a), 3 (a))

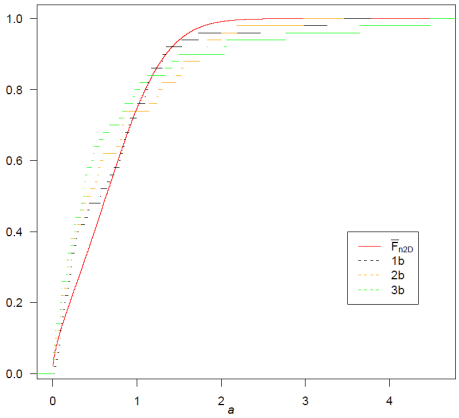


Figure 3.28: Cumulative distribution function comparison of the cuts of the sections of alumina ceramics with exactly 50 cells (Fig.3.22 1(b) black line, 2(b) yellow line, 3(b) green line) and of the 2D Sectional Poisson-Voronoi cells area conditioned on $N_{2D} = 50$ (red line)

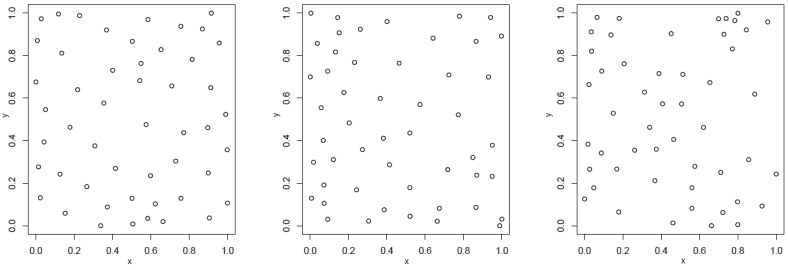


Figure 3.29: From left to right centres of mass of the cuts of the sections of alumina ceramics with exactly 50 cells (Fig.3.22 1 (b), 2 (b), 3 (b))

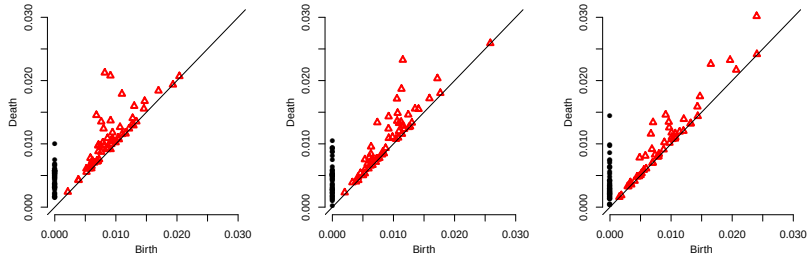


Figure 3.30: From left to right persistence diagrams of the centers of mass of the cuts of the sections of alumina ceramics with exactly 50 cells (Fig.3.22 1 (b), 2 (b), 3 (b))

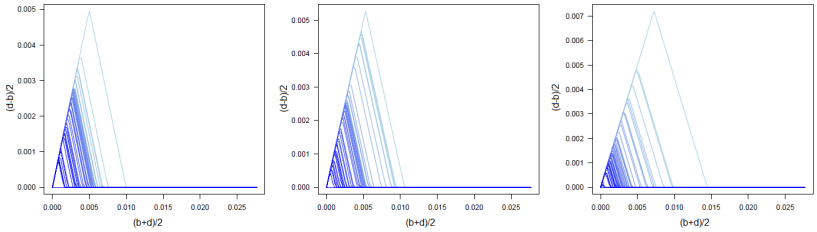


Figure 3.31: From left to right persistence landscapes (connected components) of the cuts of the sections of alumina ceramics with exactly 50 cells (Fig.3.22 1 (b), 2 (b), 3 (b))

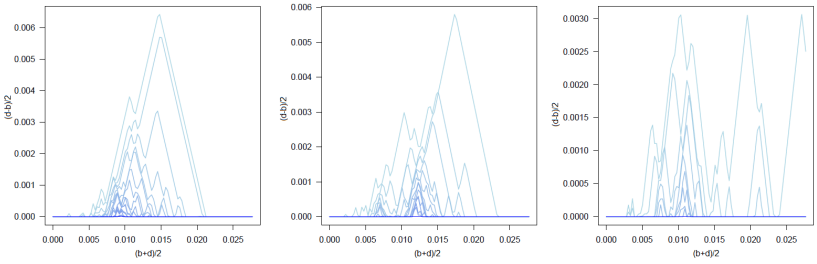


Figure 3.32: From left to right persistence landscapes (holes) of the cuts of the sections of alumina ceramics with exactly 50 cells (Fig.3.22 1 (b), 2 (b), 3 (b))

Table 3.7: Values of the different model tests for the schemes of plane sections of alumina ceramics (Fig.3.22 1 (a), 2 (a), 3 (a))

(a) *1b*		(b) *2b*		(c) *3b*	
c	0.848 (0.073)	c	0.959 (0.002)	c	1.492 (0)
d	0.078 (0.710)	d	0.121 (0.172)	d	0.168 (0.006)
l_0	0.058 (0)	l_0	0.057 (0)	l_0	0.062 (0)
l_1	0.019 (0)	l_1	0.028 (0)	l_1	0.018 (0)

Table 3.8: Values of the different model tests for the cuts of the sections of alumina ceramics with exactly 50 cells (Fig.3.22 1 (b), 2 (b), 3 (b))

(a) *1b*		(b) *2b*		(c) *3b*	
c	0.931 (0.004)	c	1.002 (0.0002)	c	1.328 (0)
d	0.154 (0.014)	d	0.172 (0.004)	d	0.248 (0)
l_0	0.077 (0)	l_0	0.116 (0)	l_0	0.137 (0)
l_1	0.041 (0)	l_1	0.024 (0)	l_1	0.009 (0)

3.8. CONCLUSIONS

This Chapter provides a general setting for testing whether a microstructure is generated by a Poisson-Voronoi diagram, based on a cross section of the microstructure. Taking inspiration from previous work in this field, [50, 73], we widen the testing framework proposing new model tests. In particular, we introduce test statistics using tools coming from different statistical branches like Goodness of Fit and Topological Data Analysis, which show to be more powerful under the specific alternative hypothesis, 2D Poisson-Voronoi diagram. We consider the situation with periodic boundary conditions, which is popular in materials science applications, and without these conditions. Our approach is very general and can be extended to test hypotheses for more complicated models describing the 3D structure based on a 2D section.

Being able to accept the Poisson-Voronoi model on the basis of 2D real metal sections means having complete probabilistic information on the underlying 3D structure. Furthermore, testing a more general model assumption on metal microstructure and accepting the underlying hypothesis will allow to perform mechanical experiments using virtual microstructures and discovering new interesting relations between microstructure features and mechanical properties much faster than possible using physical experiments.

Moreover, since as shown in Section 3.7, Poisson-Voronoi model can be a too simple model for a single-phase microstructure as alumina ceramics, alternative models are required. Hence, future developments involve testing of more general and less understood Voronoi structures for more complicated microstructures, such as Multi-Level Voronoi diagrams. Another interesting direction is to consider fully data based approaches for analysing 2D sections. For instance, studying such a section using a persistence land-

scape does not need the rigid restrictions on the geometry of the cells as present in the Poisson-Voronoi model.

4

DIGITAL MATERIAL REPRESENTATION

Representing metallic microstructure is not an easy task. Microstructure, resulting from binding chemistry and processing history, dictates the final properties and performance of the metallic alloy. Microstructure can be considered the "DNA" of the material and for producing new metallic alloys with desired properties, a deep comprehension of it is necessary. In the classical experimental approaches, problems related to gathering data in a reasonable time-frame and at relatively low cost can occur. Therefore, methods based on digital representation of the material have been developed. In this Chapter, two different methods for the virtual representation of the microstructure of AISI420 steel are presented. The first one accurately matches empirical and digital descriptors to recreate a Representative Volume Element of the material under study. The latter generates statistical virtual microstructures with "similar" geometrical and physical characteristics. Furthermore, in the case in which Poisson-Voronoi assumption is rejected, more "complex" tessellations, such as Multi-Level Voronoi diagrams, constitute a valid alternative.

Technology is nothing. What's important is that you have a faith in people, that they're basically good and smart, and if you give them tools, they'll do wonderful things with them.

Steve Jobs

4.1. INTRODUCTION

A metallic microstructure can be defined as the three-dimensional arrangement of grains, phases and defects, with their extensive chemical and structural variety [102]. In order to represent microstructures, quantitative and qualitative characterisations of its components are needed. In the previous Chapters, the focus has been on the arrangement of the grains in (implicitly assumed) single-phase microstructure. Many metallic alloys contain more than one phase or compound[1]. The term "phase" is related to the structure of matter at the atomic scale. Usually, the predominant phase in the microstructure is referred as "matrix" phase. The study of the microstructure of multi-phase steel involves more 'complications'. For instance, particles belonging to different phases can present different size and shape distributions. Metallic compounds such as carbides, can precipitate in the microstructure during thermal processing (e.g. heating or rapid cooling). Their formation may cause local lattice distortions, making their position another interesting factor.

Another important factor that influences the mechanical performance of the material is the "texture". Metallic texture is defined as the collection of the grain orientations. A common assumption is that the material presents an "isotropic" texture, meaning that the grain orientations are uniformly at random or better that all grain orientations can occur with the same probability. In other cases, grains may present preferred orientations of planes and/or directions of slip, that influence the mechanical behaviour of the material during deformation.

Hence, for a complete description of the material microstructure, identification of the phases present (phase diagrams, volume fraction and chemical composition) and the determination of the morphology (grain arrangement, grain size, grain orientation) of the grains are the fundamental steps.

Having acquired the necessary microstructural information, the aim is to virtually generate/reproduce microstructures and studying the mechanical properties associated to their microstructural features. In [88] an extensive review of digital representations of metallic microstructure is presented. This procedure called "Digital Material Representation" (DMR) is schematically summarised in Figure 4.1. Two main approaches are distinguished: exact reconstruction of microstructures and synthetic generation of microstructures.

In both cases, the aim is to reconstruct or produce a volume element that represents the microstructure from the geometrical, physical and mechanical point of view. The adjective "Representative" is then added if the volume element is sufficiently large (relatively small) to represent materials properties.

Exactly reconstructing microstructures means using experimental data, coming for instance from empirical sectioning of the materials or from tomographic measurements, to loyally produce a smaller (digital) version of the microstructure. However, obtaining this kind of data and a digital microstructure based on them is usually quite demanding and not easily accessible [88].

The second approach, synthetic generation of microstructures, involves the generation of a virtual microstructure by matching (or partially matching) statistical and stereolog-

[1] A metallic compound is a compound that contains one or more metal elements bonded to another element.

ical parameters of the real microstructure [6].
Another important distinction regards the output of the digital material representation. Two main different structures can be obtained: Representative Volume Element (RVE) and Statistically Similar Representative Volume Element (SSRVE). The first definition of

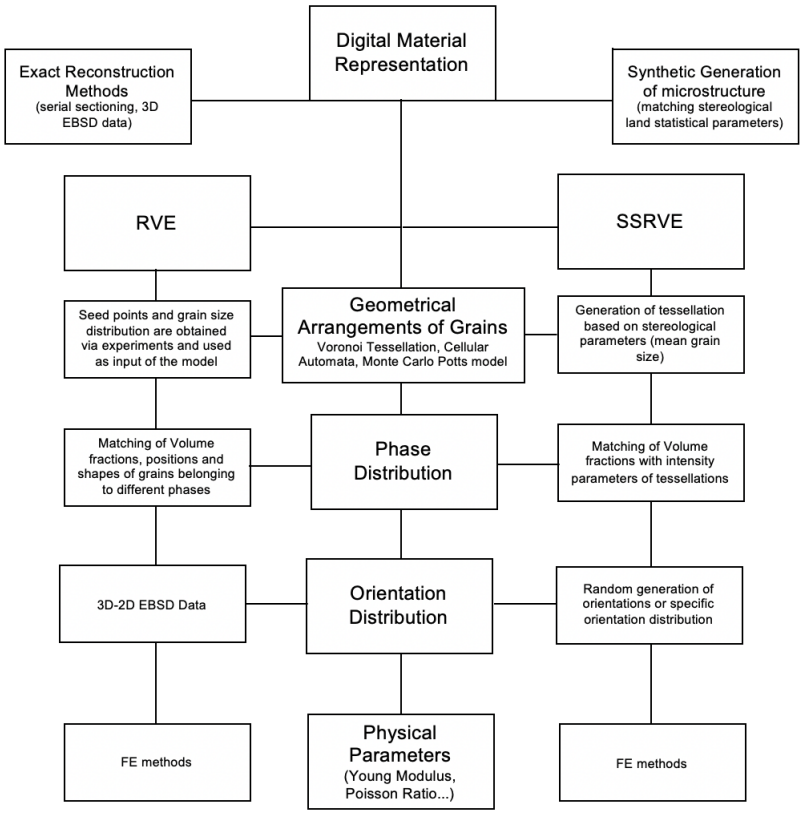


Figure 4.1: Schematic version of methods for Digital Material Representation. The middle column indicates important aspect of the representation. The left- and right column state how these aspects are dealt with in both approaches

RVE is given in [59] as a microstructural sub-region that is representative of the entire microstructure in 'an average sense'. Typically, an experimentally measured large portion of the material's microstructure is considered as a suitable RVE if it is large enough to ensure statistical homogeneity [7].

Alternatively, a digital RVE can be produced based on exact reconstruction methods [19].
An SSRVE or similar constructs, such as statistically equivalent representative volume element (SERVE) [148] or statistically similar volume elements (SSVEs) [19], are structures

generated with a lower morphological complexity compared to real microstructures but still representing the material's mechanical behaviour accurately. The construction of an SSRVE is based on the incorporation of stereological and physical parameters in a volume partitioned by a tessellation. In fact, defining a geometrical structure and dividing the computational domain in an appropriate geometrical tessellation is the first step for the construction of both RVE and SSRVE.

Methods like Voronoi tessellations [103], cellular automata [162] or Monte Carlo Potts models [169] are common ways for describing the geometrical structure underlying the microstructure. As discussed in the previous Chapters 2-3, Voronoi tessellations are defined as the state of the art geometrical methods for generating polycrystalline microstructures, given that their cell growth process is able to mimic the nucleation and growth of grains [8, 165]. In particular, the Poisson-Voronoi diagram is the classical approach to generate single-phase microstructures [88]. However, its use for more complex microstructure is often questionable. Methods for assessing the appropriateness of its use are proposed in Chapter 3. The main limitations of the Poisson-Voronoi diagrams are: i) the impossibility of controlling the shape of the grain size distribution. This can indeed make their use inaccurate for multi-phase or anisotropic microstructures reconstruction; ii) the intrinsic convexity of the grains that can, especially for multi-phase microstructures, limit their capability of mimicking observed features in metallic microstructures.

For overcoming these problems, different alternatives have been proposed. The first approach consists of changing the underlying point process of the generator points of the tessellation. As already seen in Chapter 3, a possible alternative for representing materials microstructures with a more heterogeneous grain size distribution is choosing as underlying point process a Matérn Cluster (CVT) point process. If instead the aim is to represent a more regular arrangement of the grains in metal microstructures, a point process such as Matérn Hard-Core point process (HVT) can be used [50, 49].

Later, with similar objectives, models such as Controlled-Voronoi tessellations [165, 166] and Laguerre-Voronoi [151] tessellations have been proposed. Controlled-Voronoi tessellations are introduced with the aim of controlling the grain size distribution, by tuning a regularity parameter, based on the ratio of the distance between two neighbour cells and the distance one would observe if the structure would be as regular as a honeycomb structure [167]. More specifically, N points are generated in a finite volume with periodic boundary conditions according to a specific law: once the first point is generated subsequent points are 'accepted' only if they are located no nearer than a minimum allowed distance from all other points [168].

Laguerre-Voronoi diagrams, also called weighted-Voronoi diagrams or power diagrams, are a generalisation of the classical Voronoi diagrams in which the generating sites are given an additional weight that affects the size of the associated cells [151]. However, if from one side the increased control of the size distribution of the cells can allow to generate a more realistic metals microstructure, degenerating conditions such as cells containing multiple or no generator points can occur [37]. Another approach, adopted to allow for non-convex grains and to represent multi-phase microstructures, is using Multi-Level Voronoi diagrams [72, 161]. The idea behind this tessellation method is to stack layers of tessellation with a decreasing intensity parameter of the generator points.

For instance, in a Two-Level Voronoi algorithm, first a fine tessellation of Voronoi cells is generated which will form the building blocks of the microstructure. Then, a second set of sites is generated with a lower intensity compared to the one of the first tessellation. The second level cells, or the resulting grains, are given by the union of all cells of the first tessellation with generator points closest to the second level generator point than to the others. Using more flexible models for representing the geometrical aggregation of the grains can allow to include different grain size and shape distributions for grains of different phases or precipitates, making the resulting digital microstructure more 'similar' to real ones. Once the phase compositions, the texture (the distribution of the grain orientations) and the geometrical arrangement of the grains have been obtained, phenomenological laws for the mechanical behaviour depending on these factors have to be assigned for obtaining an accurate 'digital twin' .
In this Chapter, the main aim is representing the microstructure of the annealed AISI420 stainless steel with $M_{23}C_6$ carbides. In fact, understanding the role of $M_{23}C_6$ carbides in the strain development of the material can lead to the design of metals with desired levels of strength. Using a virtual representation of the microstructure allows to have full control of the position, the size and the shape of the precipitates, reducing time and costs typical of real experiments. The two different ways of digitally representing microstructures are considered. In Section 4.2, the creation of RVE based on Electron Backscatter Diffraction (EBSD) data and Finite Element reconstruction methods implemented in the software DREAM.3D is presented. In Sections 4.3 an SSRVE is constructed. The geometrical structure underlying the virtual microstructure is a Multi-Level Voronoi diagram presented in Section 4.3.1. In Section 4.4 the difference between the two approaches and the importance of their accuracy are discussed.

4.2. REPRESENTATIVE VOLUME ELEMENT

In this Section, the creation of a digital Representative Volume Element (RVE) is presented. As previously stated, the term RVE is usually used for indicating a smaller volume element with respect to the whole material, that contains all necessary information and properties of the microstructure under study. An RVE can be both a real smaller part of the material or a digital version constructed as loyally as possible to the real microstructure. The latter is the approach followed in this Section. In order to produce an RVE as similar as possible to the real material, the initial microstructure of the steel must be studied and quantified. The microstructure of annealed AISI420 consists typically of ferrite (matrix phase) with various precipitate particles, predominantly below 10μm, identified as $M_{23}C_6$ Fe-Cr carbides [26]. Figure 4.2 shows a secondary electron image of the microstructure before deformation in which ferrite grains are highly populated with precipitates, namely $M_{23}C_6$ carbides. $M_{23}C_6$ carbides mainly precipitate along prior austenite grain boundaries [64, 160]. Electron Backscatter Diffraction (EBSD) is one of the most used techniques to measure polycrystalline microstructures [19]. Crystallographic orientations, misorientations, grain size, grain boundaries and phases of steel specimens are the kind of data that can be obtained using EBSD. Most empirical methods for grain reconstruction are based on EBSD, more specifically on the crystallographic orientation and misorientation measurements. Indeed, exploiting the definition of a grain as a region containing material that is within a (small) specified orienta-

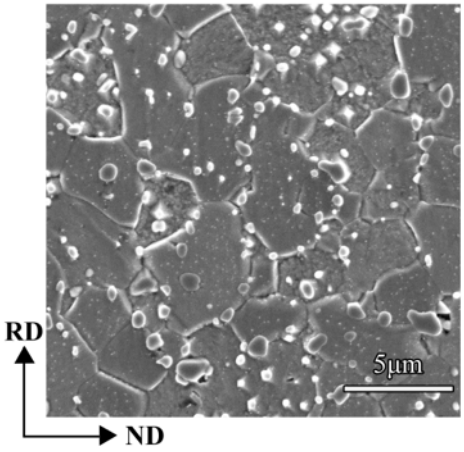


Figure 4.2: Secondary electron SEM image of *AISI*420 with $M_{23}C_6$ carbides (smaller particles) in which rolling direction (RD) and normal direction (ND) is indicated.

tion range, a small variation of orientation can occur within a grain. Defining a critical value for the misorientation angle (commonly between 10° and15°), it is possible to obtain an accurate reconstruction of the microstructure. EBSD measurements and inverse pole figure map (stereographic projection of the crystallographic directions present in the grains that constitute the material) for the material under study are shown in Figure 4.3. As it is possible to see from Figure 4.3, $M_{23}C_6$ carbides seem to be uniformly dis-

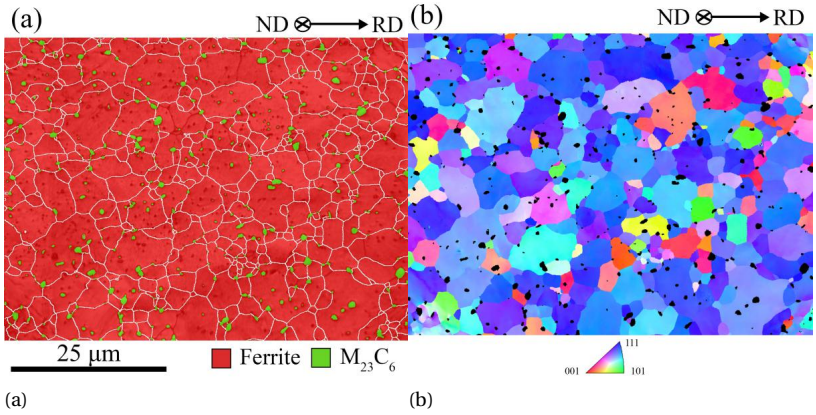
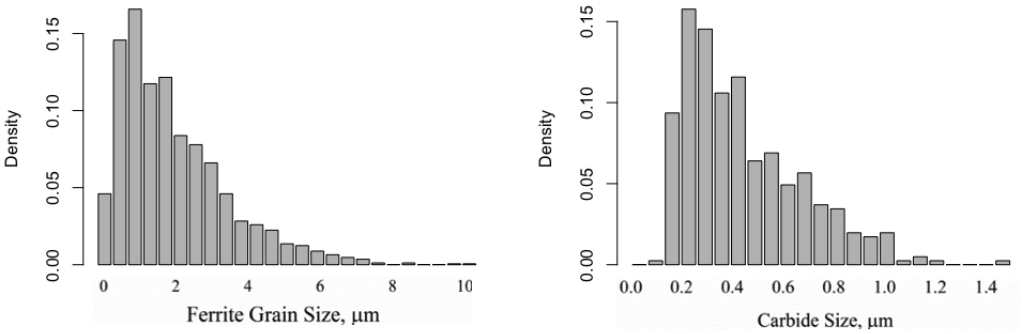


Figure 4.3: (a) EBSD phase map overlapped on image quality map in which white lines delimit ferrite grains with boundary angles higher than 10°. (b) ND inverse pole figure map for ferrite phase; black regions represent $M_{23}C_6$ carbides

tributed within the ferrite matrix. A carbide fraction of 0.032 is measured by EBSD (50 nm step size). The size distributions of ferrite grains and $M_{23}C_6$ carbides are shown in

Figure 4.4 and relevant statistical parameters are collected in Table 4.1. These values are obtained from several EBSD maps taken with surfaces perpendicular to the normal and transverse direction. More than 1000 grains are included in the analysis.



(a) (b)

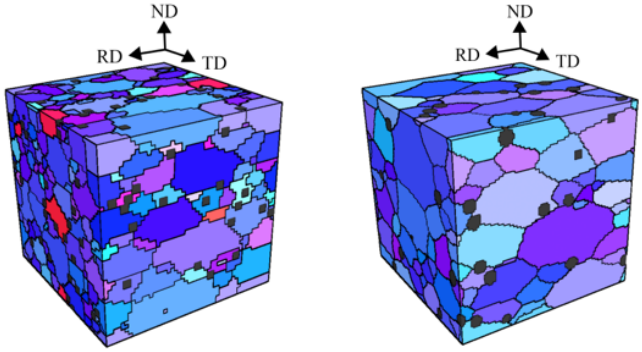
Figure 4.4: (a) Ferrite grain size distribution (b) Carbide size distribution

Table 4.1: Estimated moments of the geometrical features of 1000 grains obtained by EBSD measurements

(a) Ferrite		(b) Carbides	
Volume Fraction	0.968	Volume Fraction	0.032
Mean Volume (μm)	2.58 ± 0.05	Mean Volume (μm)	0.45 ± 0.03
Mean Area (μm)	4.43 ± 0.07	Mean Area (μm)	0.70 ± 0.03

To produce the RVE, the texture and other microstructural parameters obtained by several EBSD measurements are used. The DREAM.3D software [46] is a software commonly employed for RVE generation. It is based on an algorithm that first creates a collection of idealised ellipsoidal grains having distributions of size, shape and shape orientation equal to those observed in the experimental microstructure; secondly, the generated grains are placed inside a volume. A number of constraints are used to determine the arrangement and spatial location of the grains inside this volume. Then, crystallographic orientations obtained via EBSD are assigned to the grains. Finally, a Finite Element (FE) procedure[2] is employed to pool all information in a single volume element. In Figure 4.5 two different RVEs with different resolution and number of grains are shown. They are generated for two different specific purposes. The one with lower resolution

[2] Finite-element methods are developed for reducing the huge number of unknowns in an engineering problem in a smaller number by dividing the solution region into small parts called elements and by expressing the unknown field variables in terms of assumed approximating functions (interpolating functions/shape functions) within each element [158]



(a) (b)

Figure 4.5: Two RVEs with different resolution and number of grains: (a) 50 × 50 × 50 voxels, 502 ferrite grains and 174 carbides (b) 100 × 100 × 100 voxels, 268 ferrite grains and 109 carbides

(Figure 4.5 (a)) is used for calibration of material properties; the second one (Figure 4.5 (b)) is used for the assessment of local strain development during uniaxial deformation. In fact, important physical parameters have to be incorporated in the RVE in order to obtain a proper digital twin. More details on the physical parameter and the phenomenological laws that will be assigned to the reconstructed volume element are given in Chapter 6.

4.3. STATISTICALLY SIMILAR REPRESENTATIVE VOLUME ELEMENT

As seen in the previous Section, the construction of RVE is based on empirical measurements such as EBSD data and inverse pole figure maps. In fact, RVE are sometimes considered as the maximal measurable portion of a microstructure [130]. Due to the high complexity one can achieve in retrieving data of real microstructure morphology, using RVEs as inputs of FE methods can be computationally inefficient. Therefore, the SSRVE concept is developed with the aim of creating a structure with a lower complexity but that still maintains the principal characteristics of the real microstructure. Examples of their use can be found in [6, 19, 72, 122, 148, 161]. In this Section, an SSRVE is constructed with software provided by Tata Steel. The software allows to create volume elements in which the grains are arranged according to Multi-Level Voronoi tessellations. In the next subsection, details about the definition of this new kind of diagrams and qualitative description of their geometrical characteristics are presented.

4.3.1. MULTI-LEVEL VORONOI TESSELLATION

In order to account for non-convex grains and to include different grain size distributions for grains of diverse phases, Tata Steel developed an algorithm based on the generation of a Multi-Level (Multi-Layer) Voronoi tessellation for the simulation of steels microstructure [72, 161]. Following the same approach used in Chapter 2, without loss

of generality we introduce the Multi-Level Voronoi diagrams considering two tessellation layers.
Consider two finite sets of distinct points in $\mathbb{R}^d$, $X_1 = \{x_{k1} : k = 1,\dots n\}$ and $X_2 = \{x_{i2} : i = 1,\dots m\}$ and usually $m < n$. Here, $\{x_{k1}\}$ are the generator points of the first level tessellation, and a first level cell is defined as

$$C_{k1} = \{y \in \mathbb{R}^d : ||x_{j1} - y|| \leq ||x_{k1} - y||, j \neq k\}, \ k = 1,\dots,n. \tag{4.3.1}$$

where $||\cdot||$ is the usual Euclidean norm. Let

$$I_i = \{k : ||x_{i2} - x_{k1}|| \leq ||x_{i2} - x_{l1}||, l \neq k\}, \ i = 1,\dots,m, \tag{4.3.2}$$

be a set of indices. The cells of the resulting Multi-Level Voronoi tessellation, also referred as second level cells or grains, are given by:

$$C_i^* = \bigcup_{k \in I_1} C_{k1}, \ \ i = 1,\dots,m. \tag{4.3.3}$$

Loosely speaking it means that given two point sets ($m < n$), all the first level cells are merged together if their generator points are closest to the second generator point with respect to all the others. If we assume that the sites of both the first and the second tessellation are generated according to Poisson processes, Φ_1 and Φ_2, with intensity parameters λ_1 and λ_2 respectively ($\lambda_1 > \lambda_2$), we refer to the resulting tessellation as Multi-Level Poisson-Voronoi Diagram, $\mathscr{MV}_{(\Phi_1,\Phi_2)}$.
However, unlike the case of the classical Poisson-Voronoi diagrams, there is not just one parameter (the intensity parameter of the underlying Poisson process) influencing the distribution of the geometrical characteristics of the grains. For illustrating this concept, two different 3D Multi-Level Voronoi diagrams and their corresponding 2D sections are shown in Figure 4.6.

The two diagrams are both generated in a finite volume of $10 \times 10 \times 10$ and the intensity of the second layer generator points is the same, namely 0.1. This intensity value is responsible for the resulting number of grains in the tessellation (bigger grains indicated by colours and separated by bold black lines). The first level tessellations of the two diagrams have different generator points intensities. For the first diagram, 4.6 (a)-(b), the intensity of the first level cells is equal to 0.3; for the second, 4.6 (c)-(d), it is equal to 3. This intensity difference results in different grain morphologies. Taking λ_1 very small results in a tessellation with grains clearly not convex and with more irregular boundaries. If $\lambda_1 \to \infty$ the resulting diagram boils down to the original Poisson-Voronoi diagram based on the second level generating points and therefore the resulting grains are convex.
In Figures 4.7-4.8 the volume and the surface area distributions of the cells of the first tessellation (a)-(c) and of the grains of the whole tessellation (b)-(d) are compared. In Figure 4.9 a ECDF visual comparison for volume and surface area distributions is provided. Especially from this last comparison is possible to notice how the two grain surface area distributions differs. Similar conclusions can be drawn from the ECDF visual comparison of area and perimeter distributions of 2D random sections of the two structures (Figure 4.10). Another advantage of using Multi-Level Voronoi tessellations is

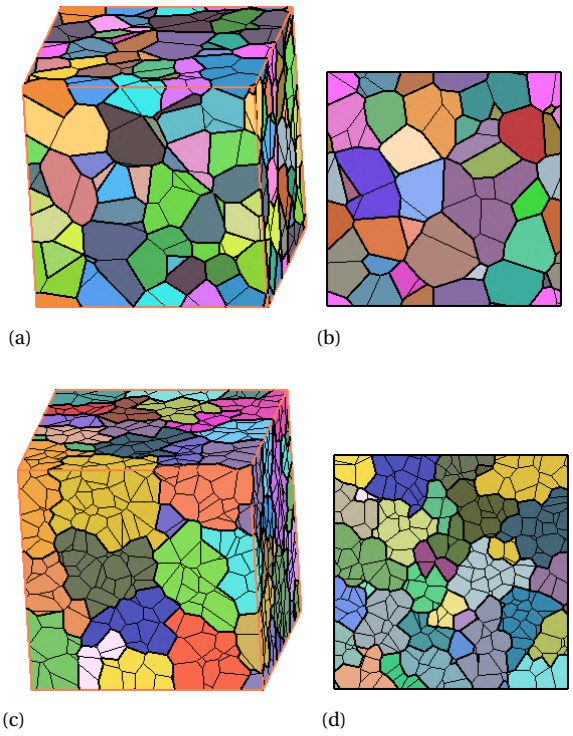


Figure 4.6: (a) 3D Multi-Level Poisson-Voronoi diagram and corresponding (b) 2D sectional Multi-Level Poisson-Voronoi diagram with $\lambda_1 = 0.3$ and $\lambda_2 = 0.1$ (c) 3D Multi-Level Poisson-Voronoi diagram and corresponding (d) 2D sectional Multi-Level Poisson-Voronoi diagram with $\lambda_1 = 3$ and $\lambda_2 = 0.1$

the possibility of defining different size distributions for grains of diverse phase or for precipitates. Its use is explained in the construction of an SSRVE of the microstructure of the annealed AISI420 stainless steel with $M_{23}C_6$ carbides. In SSRVE construction, as previously mentioned, matching of stereological parameters is a fundamental step. For instance for the definition of the phases, empirical values of the volume fractions and the correspondent mean grain size values (Table 4.1) are used. The volume fraction of the ferrite phase is used for defining the intensity parameter of the second level grains, instead the volume fraction of the carbides for the intensity of the first level cells. The intensity parameter of the first level tessellation is consequently decomposed as:

$$\lambda_1 = \lambda_1^f + \lambda_1^c,$$

where λ_1^f is the intensity of the grains belonging to the ferrite phase and λ_1^c is the intensity of the carbides. In Figure 4.11, two different SSRVEs with different λ_1^c, equal to 0.03 and 0.11[3], are presented. The software allows also to assign crystallographic orien-

[3]These volume fraction values are chosen accordingly to the volume fractions of carbides measured for the AISI420 under study with EBSD and XRD respectively

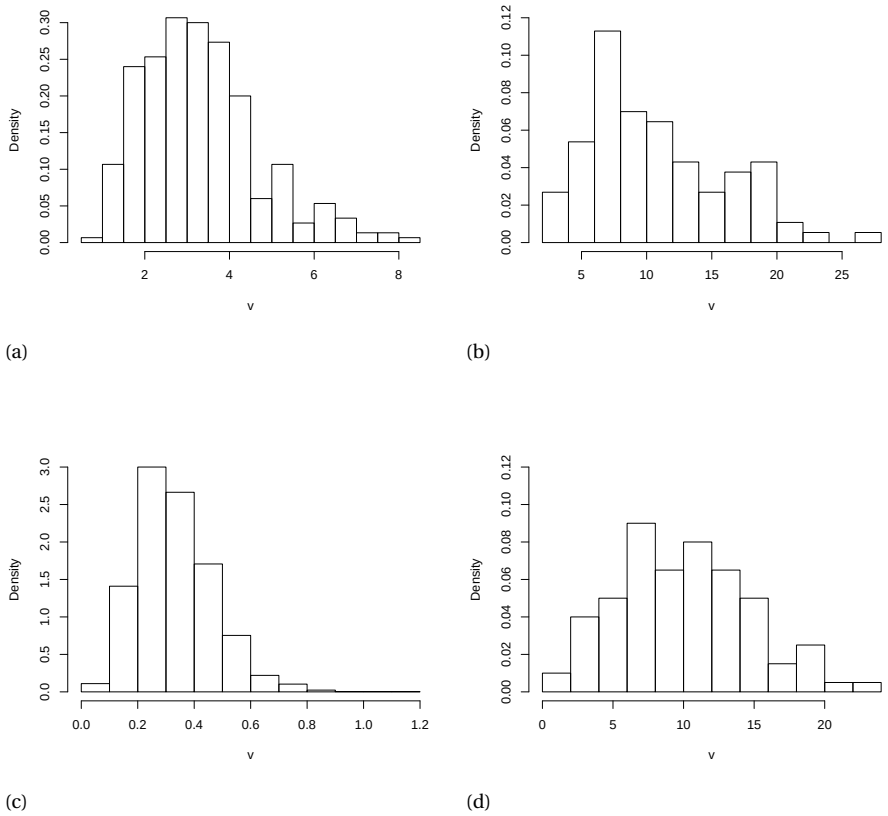
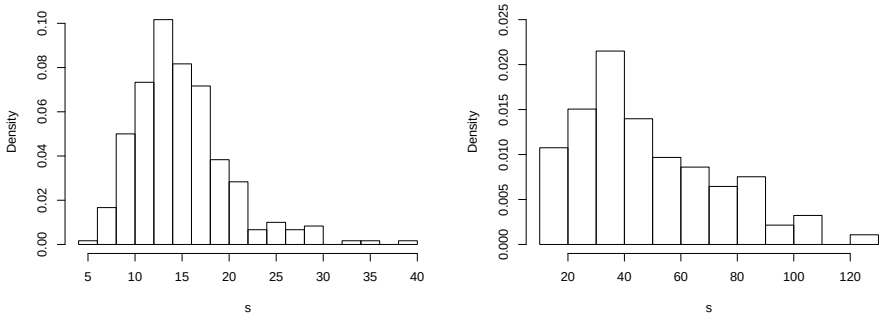


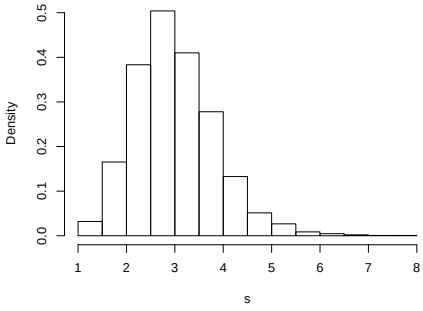
Figure 4.7: Histogram of the volume of the first level cells and of the second level grains of a 3D Multi-Level Poisson-Voronoi diagram with $\lambda_1 = 0.3$ and $\lambda_2 = 0.1$ (a)-(b) and of a 3D Multi-Level Poisson-Voronoi diagram with h $\lambda_1 = 3$ and $\lambda_2 = 0.1$(c)-(d)

tations, and thus a texture to the generated structure. Random orientation structures or specific orientation information empirically gathered with EBSD method, can be defined. For completing the definition of an SSRVE, as in the RVE case, physical parameter and phenomenological laws have to be incorporated to obtain the final statistical digital twin. In Chapter 6 more details about this procedure are given.

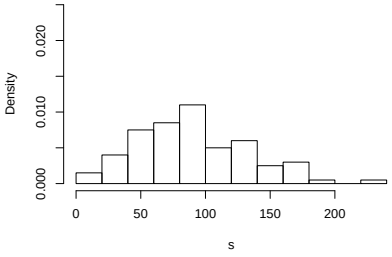


(a)

(b)

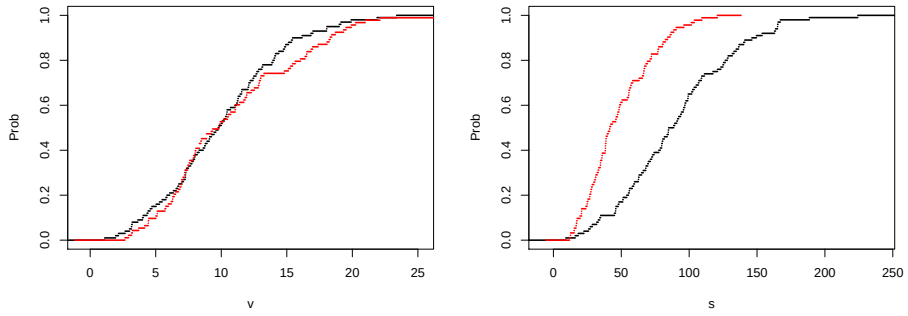


(c)



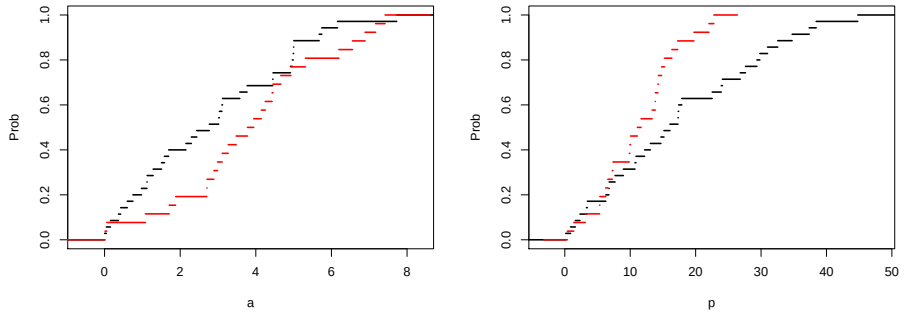
(d)

Figure 4.8: Histogram of the surface area of the first level cells and of the second level grains of a 3D Multi-Level Poisson-Voronoi diagram with $\lambda_1 = 0.3$ and $\lambda_2 = 0.1$ (a)-(b) and of a 3D Multi-Level Poisson-Voronoi diagram with h $\lambda_1 = 3$ and $\lambda_2 = 0.1$(c)-(d)



(a) (b)

Figure 4.9: Empirical Cumulative Distribution comparison between the volume distributions of 100 grains (a) and the volume distributions of the second level grains (b) of a 3D Multi-Level Poisson-Voronoi diagram with $\lambda_1 = 0.3$ and $\lambda_2 = 0.1$ (red line) of a 3D Multi-Level Poisson-Voronoi diagram with h $\lambda_1 = 3$ and $\lambda_2 = 0.1$ (black line)



(a) (b)

Figure 4.10: Empirical Cumulative Distribution comparison between the area distributions of the first level cells (a) and the area distributions of the second level grains (b) of a 2D section of a 3D Multi-Level Poisson-Voronoi diagram with $\lambda_1 = 0.3$ and $\lambda_2 = 0.1$ (red line) and of a 3D Multi-Level Poisson-Voronoi diagram with h $\lambda_1 = 3$ and $\lambda_2 = 0.1$ (black line)

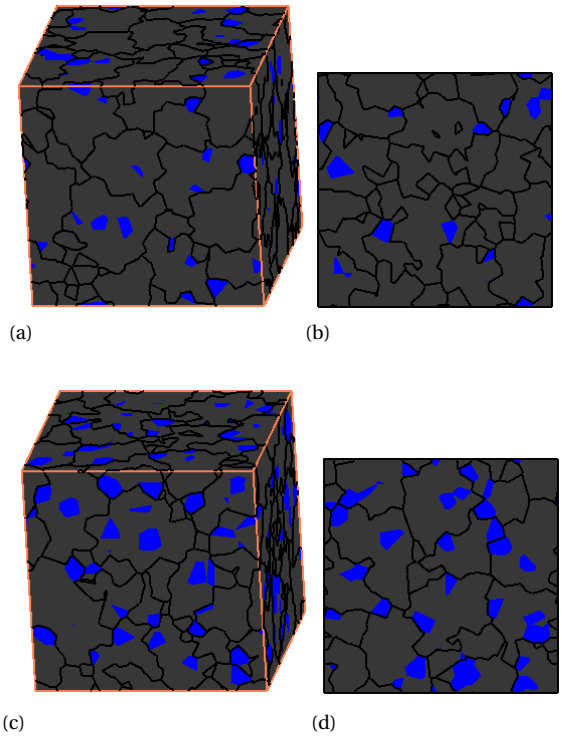


Figure 4.11: Two SSRVEs with the same number of ferrite grains (λ_2) but different carbides volume fractions (λ_1^c) generated in a volume $10 \times 10 \times 10$: (a) 3D Multi-Level Poisson Voronoi diagram and corresponding (b) 2D sectional Multi-Level Poisson Voronoi diagram with $\lambda_1 = 3$ ($\lambda_1^c = 0.03$) and $\lambda_2 = 0.5$ (c) 3D Multi-Level Poisson Voronoi diagram and corresponding (b) 2D sectional Multi-Level Poisson Voronoi diagram with $\lambda_1 = 3$ ($\lambda_1^c = 0.11$) and $\lambda_2 = 0.5$. The blue particles are cells of the first level tessellation for which a different phase (carbide) is assigned

4.4. CONCLUSIONS

Being able to virtually reconstruct microstructures is the first step in understanding the relation between microstructure features and mechanical properties. Accurately mimicking steel microstructures or generating a similar digital version of it, can lead to the creation of new materials with desired mechanical properties. In this Chapter, two different approaches have been presented for representing the microstructure of AISI420 stainless steel with $M_{23}C_6$ carbides. The first approach is based on exact reconstruction methods resulting in the creation of RVEs. The latter, more statistically oriented, is based on the synthetic generation of SSRVEs. Constructing RVEs can lead to more accurate results with disadvantages in terms of time and costs than generating SSRVEs, which compensates the drawbacks of the first approach, but with poorer accuracy. However, the two approaches are not mutually exclusive. In fact, it is possible to construct RVEs for testing and calibrating the physical parameters that have to be assigned to the microstructure and in the same study using SSRVEs for performing large scale simulations and obtaining new insight into the relationship between microstructure features and mechanical properties.

II

MEC

5

MECHANICAL PROPERTY INVESTIGATION FROM 2D IMAGES

Investigating the main determinants of the mechanical performance of metals is not a simple task. Already known physically inspired qualitative relations between 2D microstructure characteristics and 3D mechanical properties can act as the starting point of the investigation. Isotonic regression allows to take into account ordering relations and leads to more efficient and accurate results when the underlying assumptions actually hold. The main goal in this Chapter is to test order relations in a model inspired by a materials science application. The statistical estimation procedure is described considering three different scenarios according to the knowledge of the variances: known variance ratio, completely unknown variances, variances under order restrictions. New likelihood ratio tests are developed in the last two cases. Both parametric and non-parametric bootstrap approaches are developed for finding the distribution of the test statistics under the null hypothesis. Finally an application on the relation between Geometrically Necessary Dislocations and number of observed microstructure precipitate is shown.

One sees qualities at a distance and defects at close range.

Victor Hugo

5.1. INTRODUCTION

Understanding the intrinsic nature of the mechanical properties of metals is not an easy task. In order to get insight into what gives desired mechanical performance to a metal, a deep and detailed analysis of the metal microstructure characteristics is needed. For instance, it is known in literature that dislocations, i.e. line defects in the crystalline arrangement of the atoms [65], play a fundamental role in the mechanical behaviour of metal alloys. More specifically, the appearance of Geometrically Necessary Dislocations[1] (GNDs) during plastic deformation of the material contributes to the hardening of the material. Detecting GNDs from 2D microstructure images is often challenging. A widely accepted way is to use the so called Kernel Average Misorientation (KAM) [98]. The KAM, measured in Electron BackScatter Diffraction (EBSD), quantifies the average misorientation around a measurement point with respect to a defined set of a nearest or nearest plus second-nearest neighbour points of EBSD observation [21].
In [79, 118, 14] studies on the relation between GNDs and microstructure properties such as grain size and carbide size are presented. The relation between GNDs and grain size has both theoretical and experimental confirmation and it can be related to the well-known macroscopic Hall-Petch relation [51, 109]. In fact, the Hall-Petch relation, in its original version, describes the negative dependence of yield stress (mechanical property) on grain size; loosely speaking the smaller the grains are, the stronger the material is. More specifically in [68] the authors give as an explanation of the relation between GNDs and grain size that as the grain size decreases the grain boundary layer in which GNDs typically accumulate, occupies a greater volume fraction of the material, therefore it is reasonable to think that the smaller the grains are, the more GNDs will be observed. Still unclear is instead the relation between carbides and GNDs. In fact, since the 1940's several studies on the effect of carbides on the mechanical behaviour of metals have been conducted. In [110] the authors state that the primary carbides and their distribution have a major influence on the wear resistance and the toughness of the material. However, carbides tend to precipitate along the grain boundaries, that as said before, are the locations in which GNDs typically accumulate. Until now, no direct physical relationship has been found between carbides and Geometrically Necessary Dislocations. Therefore, isolating the effect of carbides and assessing the conjecture on the positive relation between carbides and GNDs is a problem of interest. In [58] a descriptive statistical analysis with response variable KAM, used as a proxy of GNDs and as explanatory variables the number of grains, the number of carbides and the position of carbides revealed an almost monotone trend of the response variable according to the increments of the explanatories.
Therefore, in order to take into account the already known direction of the physical relation, we want to propose an approach that incorporates this information and a procedure for testing the prementioned conjectures on a new dataset.

[1] Dislocations are usually classified into redundant and non-redundant dislocations, respectively called Statistically Stored Dislocations (SSDs) and Geometrically Necessary Dislocations (GNDs). GNDs are dislocations with a cumulative effect and they allow the accommodation of lattice curvature due to non-homogeneous deformation. They control the work hardening individually by acting as obstacles to slip and collectively by creating a long-range back stress.

5.2. ISOTONIC REGRESSION

In this context, isotonic regression comes to aid. In fact, the idea at the basis of isotonic regression is taking order restrictions into account for improving the efficiency of the statistical analysis by reducing the error or the expected error of estimates and increasing the power of the testing procedures, provided that the hypothesised order restriction actually holds. The first papers about isotonic regression appeared in the 1950's [4, 153] and books [9, 32] are well known references for statistical inference under order restrictions. Isotonic regression proves its power in different fields such as epidemiology in testing the effects of different treatments or in dose-finding [127, 147], but also in genetics [86], business [69], biology [10]. There are not many examples of isotonic regression use in materials science. Throughout this Chapter special attention is given to the peculiar data structure. Nowadays, developments towards multivariate isotonic regression, isotonic regression in inverse and censoring problems [48, 47], Bayesian isotonic regression [77] are ongoing. But also in the most basic framework there is still something missing.

In this Chapter, starting off with the most basic case, univariate isotonic regression of means under normality assumptions with known variances, we guide the reader into estimation and testing order restriction assumptions, considering different conditions on the variances.

Three different scenarios are considered. In all three cases, we focus on maximum likelihood as estimation procedure and likelihood ratio test as test statistic for hypothesis testing.

The first case is the basic case in which 'the variances' are known or unknown but their ratio is known. This instance is considered extensively in [9, 32] and results for estimation and testing order restrictions are already known.

The second scenario is from an applications point of view the most common scenario in which the variances are unknown. In [140], the authors derive a two steps estimating procedure for means and variances and interesting results on existence and uniqueness of the maximum likelihood estimates are derived under special conditions. Another iterative method, proposed in [139], is extended to the unknown variances case. The derivation of the test statistic and of its distribution in this scenario is not trivial. In fact, the estimate of the mean under the null hypothesis is also affected by the non knowledge of the variances. We propose the likelihood ratio test statistic and two different bootstrap approaches, one parametric and one non-parametric, for obtaining the test statistic distribution.

The last model considers not only the means under order restrictions but also the variances. This case has not often been faced probably because it is not common to have prior knowledge on the order of both means and variances. As in the unknown variances scenario, a two steps procedure for estimating means and variances is derived in [138] and similar results on existence and uniqueness under specific conditions on the empirical variances are given. In [139] an improved algorithm called Alternating Iterative Method (AIM) and more general results about convergence are derived. For testing in this case we derive the likelihood ratio test taking into account the order of variances also under the null hypothesis and apply a parametric and non-parametric bootstrap approach in line with the one derived in the unknown variance case to obtain approxi-

mate p-values.
The Chapter structure is the following. In Section 5.3 we explain the estimation procedure of the isotonic means in the three different cases. In Section 5.4 the focus is on the Likelihood Ratio Test. We present it in the three different cases and in Section 5.5 we propose both a parametric and non-parametric bootstrap approach for approximating the distribution of the test statistics under the null hypothesis. Finally, in Section 5.6 we come back to the application and we illustrate step-by-step how to deal with a real problem and more precisely how to perform isotonic regression and test for monotonicity of KAM with respect to the number of carbides. The Chapter ends with conclusions in Section 5.7.

5.3. ESTIMATING RESTRICTED MEANS IN THE NORMAL CASE

We first introduce isotonic regression and the notation used in the rest of the Chapter in a more general context. Normality is assumed throughout this section.
Let y_{ij}, $j = 1,\dots,n_i$, $i = 1,\dots,k$ be the jth observation of the response variable Y corresponding to the ith level of the explanatory variable X.
We assume Y_{ij} to be independent random variables, normally distributed with means μ_i and variances σ_i^2, $i = 1,\dots,k$, $j = 1,2,\dots,n_i$.
The log-likelihood is then given by

$$l(\boldsymbol{\mu},\boldsymbol{\sigma^2}) = \sum_{i=1}^{k}\Big\{-\frac{n_i}{2}\ln\sigma_i^2 - \frac{1}{2\sigma_i^2}\sum_{j=1}^{n_i}(y_{ij}-\mu_i)^2\Big\} + \mathrm{c} \tag{5.3.1}$$

where c is a constant which does not depend on the parameters $\boldsymbol{\mu} = (\mu_1,\dots\mu_k)'$ and $\boldsymbol{\sigma^2} = (\sigma_1^2,\dots,\sigma_k^2)'$.
Furthermore, we assume that $\boldsymbol{\mu}$ satisfies

$$\mu_1 \le \mu_2 \le \cdots \le \mu_k. \tag{5.3.2}$$

A k-dimensional vector $\boldsymbol{\mu}$ is said to be isotonic if $t \le s$ implies $\mu_t \le \mu_s$.
Be D the set of all the isotonic vectors in $\mathbb{R}^k$,

$$D = \{\boldsymbol{\mu} \in \mathbb{R}^k; \mu_1 \le \mu_2 \le \cdots \le \mu_k\} \tag{5.3.3}$$

In this section we discuss the maximum likelihood estimator of $(\boldsymbol{\mu},\boldsymbol{\sigma^2})$, where $\boldsymbol{\mu}$ is isotonic and $\sigma_i^2 > 0$. Depending on the information on $\boldsymbol{\sigma^2}$, different MLEs have been derived.
In the following three subsections the three different cases are considered.

ISOTONIC REGRESSION OF MEANS WITH KNOWN VARIANCE RATIO

This first case constitutes the most basic case in which all variances are either known or unknown but they differ according to some known multiplicative constants c_i. This means that the variance σ_i^2 of the response variable Y_i is given by:

$$\sigma_i^2 = c_i\sigma^2, \ 1 \le i \le k.$$

This specific case is already covered in [9, 32], but we hereafter report the main results. The problem of maximising log-likelihood Eq. 5.3.1 in μ can be rewritten equivalently as solving:

$$\min_{\mu \in D} \sum_{i=1}^{k} (\bar{y}_i - \mu_i)^2 w_i \tag{5.3.4}$$

where $\bar{y}_i = \frac{\sum_j y_{ij}}{n_i}$ and $w_i = \frac{n_i}{c_i}$. Note that this objective function does not depend on σ^2. The solution, $\hat{\boldsymbol{\mu}}^I$, is called the isotonic regression of $\bar{\boldsymbol{y}} = (\bar{y}_1, \ldots, \bar{y}_k)$ with weights $\boldsymbol{w} = (w_1, \ldots, w_k)$ [140]. For obtaining the solution to Eq. 5.3.4, different algorithms have been proposed in the literature ([9],[32]). In this Chapter, the "Pool-Adjacent Violators Algorithm" (PAVA) is used.
More details about the algorithm are provided in Appendix A (ALGORITHM 2.1).

ISOTONIC REGRESSION OF MEANS WITH UNKNOWN VARIANCES

In this second case, no assumptions on the variances are made. They are unknown and for obtaining the maximum likelihood estimate of $\boldsymbol{\mu}$, they need to be estimated as well. In [140] the authors consider this case and interesting results on existence and uniqueness of the MLE are achieved. We hereby recall the main results. The approach is to maximise the log-likelihood Eq. 5.3.1, with $\boldsymbol{\mu} \in D$ and $\boldsymbol{\sigma^2} \in \mathbb{R}_+^k$.
For any fixed $\boldsymbol{\sigma^2} \in \mathbb{R}_+^k$ the maximiser $\hat{\boldsymbol{\mu}}^{\boldsymbol{I}}$ of $l(\boldsymbol{\mu}, \boldsymbol{\sigma^2})$ over $\boldsymbol{\mu} \in D$ is the isotonic regression of $\bar{\boldsymbol{y}}$ with weights $\boldsymbol{w} = (w_1, \ldots w_k)'$ and $w_i = \frac{n_i}{\sigma_i^2}$.
On the other hand, for any fixed $\boldsymbol{\mu} \in D$, the maximiser $\boldsymbol{\sigma^2}$ of $l(\boldsymbol{\mu}, \boldsymbol{\sigma^2})$ over $\boldsymbol{\sigma} \in \mathbb{R}_+^k$ is $\hat{\boldsymbol{\sigma}}^{\boldsymbol{2}}(\boldsymbol{\mu}) = (\hat{\sigma}_1^2(\mu_1), \ldots \hat{\sigma}_k^2(\mu_k))'$, where $\hat{\sigma}_i^2(\mu_i) = \frac{\sum_j^{n_i} (y_{ij} - \mu_i)^2}{n_i}$.
Substituting $\hat{\sigma}^2(\mu)$ into Eq. 5.3.1, we can express the profile log-likelihood of $\boldsymbol{\mu}$ as

$$l(\boldsymbol{\mu}) = \sum_{i=1}^{k} -n_i \ln[\bar{\sigma}_i^2 + (\bar{y}_i - \mu_i)^2] + c \tag{5.3.5}$$

where $\bar{\sigma}_i^2 = \frac{\sum_j^{n_i} (y_{ij} - \bar{y}_i)^2}{n_i}$ is the sample variance of the ith normal population and c a constant that does not depend on $\boldsymbol{\mu}$. Note that $l(\boldsymbol{\mu}) \to -\infty$ if $\mu_k \to \infty$ or $\mu_1 \to -\infty$. Hence, maximising l over D is equivalent to maximising l over a compact subset of D of type $D_a = \{\mu \in D : \mu_1 \geq -a, \mu_k \leq a\}$. As l is continuous on D_a, a maximizer over D exists.
As previously said, the authors in [140] discuss also uniqueness of the MLE of $(\boldsymbol{\mu}, \boldsymbol{\sigma^2})$. They state that l is not a concave function in general and that for guaranteeing uniqueness the following condition suffices (see Theorem 2.3 [140]):

Condition 5.3.1. For $i = 1, \ldots, k$, $\bar{\sigma}_i^2 > \max\{(\bar{y}_i - \min(\bar{\boldsymbol{y}}))^2, (\bar{y}_i - \max(\bar{\boldsymbol{y}}))^2\}$.

For finding a maximizer of Eq. 5.3.5, a two steps iterative algorithm based on PAVA has been proposed in [140]. From an initial guess for $\boldsymbol{\mu}$, the associated maximizer in $\boldsymbol{\sigma^2}$ is computed and after that the maximizer in $\boldsymbol{\mu}$ based on this $\boldsymbol{\sigma^2}$ and so on. This iterative procedure stops when the maximum difference between the estimated means at step $l-1$ and at step l is less than an arbitrary small threshold value, e.g.,

$$\max_{1 \leq i \leq k} |\mu_i^{I(l-1)} - \mu_i^{I(l)}| \leq 10^{-m},$$

where m is taken to be equal to 3 in our case. In [139] the authors propose a new algorithm called Alternating Iterative Method (AIM). The procedure is based on the minimisation of a semi-convex function. In particular, restating the problem in terms of $(\boldsymbol{\mu}, \boldsymbol{\nu})$, where $\boldsymbol{\nu} = (1/\sigma_1^2, \dots, 1/\sigma_k^2)'$ and given D_a is a convex subset of $\mathbb{R}^k$ and V a convex subset of $\mathbb{R}_+^k$,

$$V = \{v \in \mathbb{R}_+^k : 0 \leq 1/\max_i(\min_{\min(\tilde{\boldsymbol{y}}) \leq \theta \leq \max(\tilde{\boldsymbol{y}})} s_i^2(\theta)) \leq v_i \leq 1/\min_i(\min_{\min(\tilde{\boldsymbol{y}}) \leq \theta \leq \max(\tilde{\boldsymbol{y}})} s_i^2(\theta))\},$$

$L(\boldsymbol{\mu}, \boldsymbol{\nu})$ is a semi-convex function because: i) $L(\boldsymbol{\mu}, \boldsymbol{\nu})$ is defined on $D_a \times V$; ii) for any given $\boldsymbol{\mu} \in D_a$, $L(\boldsymbol{\mu}, \cdot)$ is strictly convex on V and, for any given $\boldsymbol{\nu} \in V$, $L(\cdot, \boldsymbol{\nu})$ is strictly convex on D_a. The algorithm originally proposed for the simultaneous order restrictions of means and variances can be easily extended to the unknown variance case. The iteration method works in alternating the search of the minimum point, $\boldsymbol{\mu}^{(l)}$, of $L(\boldsymbol{\mu}, \boldsymbol{\nu}(\boldsymbol{\mu}^{(l-1)}))$ on a compact subset D_a and the search of the minimum point, $\boldsymbol{\nu}^{(\boldsymbol{l})}$, of $L(\boldsymbol{\mu}(\boldsymbol{\nu}^{(l-1)}), \boldsymbol{\nu})$ on V. Proof of the convergence of the algorithm does not require additional conditions [139]. The iterative procedure stops when the difference between the likelihoods at step $l-1$ and at step l is less than an arbitrary small threshold value:

$$|L(\boldsymbol{\mu}^{(\boldsymbol{l-1})}, \boldsymbol{\nu}^{(\boldsymbol{l-1})}) - L(; \boldsymbol{\mu}^{(\boldsymbol{l})}, \boldsymbol{\nu}^{(\boldsymbol{l})})| \leq 10^{-m} \tag{5.3.6}$$

A more detailed version of both algorithms is reported in Appendix A (ALGORITHM 2.2).

ISOTONIC REGRESSION OF MEANS AND VARIANCES SIMULTANEOUSLY

We now assume that both mean and variances are restricted by simple orderings. Therefore, in addition to assumption Eq. 5.3.2, we assume also:

$$\sigma_1^2 \geq \sigma_2^2 \geq \cdots \geq \sigma_k^2 > 0 \tag{5.3.7}$$

The reason for taking decreasing order is relates to our application considered in Section 5.6; increasing variances can be dealt with analogously. In [138], maximum likelihood estimation under simultaneous order restrictions on mean and variances from a Normal population is studied. Some of the most important results are hereby recalled. The approach is to maximise the log-likelihood Eq. 5.3.1 with $\boldsymbol{\mu} \in D$ and $\boldsymbol{\sigma^2} \in \bar{G}$, where $\bar{G}$ is the closure of

$$G = \{\boldsymbol{\sigma^2} \in \mathbb{R}_+^k : \sigma_1^2 \geq \sigma_2^2 \geq \cdots \geq \sigma_k^2 > 0\}. \tag{5.3.8}$$

This means that the maximizer will have positive σ^2-values if there is variation within the groups. Then, for any fixed $\boldsymbol{\sigma^2} \in G$, the maximizer $\boldsymbol{\mu^I}$ of $l(\boldsymbol{\mu}, \boldsymbol{\sigma^2})$ over $\boldsymbol{\mu} \in D$ is the isotonic regression of $\tilde{\boldsymbol{y}}$ with weights $\boldsymbol{w} = (w_1, \dots w_k)'$ and $w_i = \frac{n_i}{\sigma_i^2}$.

Furthermore, for any $\boldsymbol{\mu} \in D$, the maximizer $\hat{\boldsymbol{\sigma}}^{\boldsymbol{2I}}(\boldsymbol{\mu})$ of $l(\boldsymbol{\mu}, \boldsymbol{\sigma^2})$ is the so called antitonic regression (isotonic regression with reversed order [47]) of $\boldsymbol{s^2} = (s_1^2, \dots s_k^2)'$, $s_i^2 = \frac{\sum_{j=1}^{n_i}(y_{ij} - \mu_i)^2}{n_i}$, with weights $\boldsymbol{N} = (n_1, \dots, n_k)'$. Existence is guaranteed noticing that $\boldsymbol{\sigma^2} \in [\min_i(\min_{\min_i(\tilde{\boldsymbol{y}}) \leq \theta \leq \max_i(\tilde{\boldsymbol{y}})} s_i^2(\theta)), \max_i(\min_{\min_i(\tilde{\boldsymbol{y}}) \leq \theta \leq \max_i(\tilde{\boldsymbol{y}})} s_i^2(\theta))]$, $s_i^2(\theta) = \sum_{j=1}^{n_i}(y_{ij} - \theta)^2/n_i$ (see Theorem 2.1 [138]).

Uniqueness is proven under the following condition (see Theorem 2.2 [138])

Condition 5.3.2. For $i = 1,\dots k$ the sample variance $\bar{\sigma}_i^2$ satisfies $\bar{\sigma}_i^2 > 2(b-a)$ where b and a are the maximal and the minimal means respectively.

As in the unknown variances case, a two steps iterative algorithm is proposed for finding the solution for both means and variances under order restrictions. The proof of the convergence of the algorithm is given under Condition 5.3.2.
Later, in [139], as mentioned in the previous section, the authors show that restating the problem in terms of $(\boldsymbol{\mu},\boldsymbol{\nu})$, where $\boldsymbol{\nu} = (1/\sigma_1^2,\dots,1/\sigma_k^2)'$ Condition 5.3.2 is not needed for proving that the algorithm converges. In fact, also in this case the proposed AIM algorithm can be employed. Since $L(\boldsymbol{\mu},\boldsymbol{\nu})$ has continuous second-order partial derivatives and the Hessian matrix with respect to μ $H(\boldsymbol{\mu},\boldsymbol{\nu}) = \text{diag}(n_1\nu_1,\dots,n_k\nu_k)$ is a positive definite diagonal matrix for any fixed $\boldsymbol{\nu} = (\nu_1,\dots,\nu_k)' \in V_0$,

$$V_0 = \{\nu \in \mathbb{R}^k : 0 \leq \frac{1}{\max_i(\min_{\min_i(\bar{y})\leq\theta\leq\max_i(\bar{y})} s_i^2(\theta))} \leq \nu_1 \leq \cdots \leq \nu_k \leq \frac{1}{\min_i(\min_{\min_i(\bar{y})\leq\theta\leq\max_i(\bar{y})} s_i^2(\theta))}\}$$

then by Theorem 4 in [139] the iterative sequence of solutions to $L(\boldsymbol{\mu},\boldsymbol{\nu})$, $\{(\boldsymbol{\mu^{(n)}},\boldsymbol{\nu^{(n)}})\}$ converges to the MLE solution and consequently the sequence $\{(\boldsymbol{\mu^{(n)}},\boldsymbol{\sigma^{2(n)}})\}$ as well.
As in the previous case, the alternating iterative procedure is stopped when the maximum difference between the likelihoods at step $l-1$ and at step l is less than an arbitrary small threshold value (see Eq. 5.3.6).
A pseudo-code of the algorithms can be found in Appendix A (ALGORITHM 2.3).

5.4. LIKELIHOOD RATIO TEST: CONSTANT μ AGAINST MONOTONICITY

We are interested in testing hypotheses of monotonicity in μ under the various assumptions on the variances discussed in Section 5.3. There exists extensive literature on testing hypotheses on means. In most cases, a standard testing procedure entails testing the hypothesis of equality of means against the hypothesis that they are different. In this Chapter, we consider the same null hypothesis but the alternative is different: monotonicity of the means. As in the previous section, we consider three different testing frameworks according to the different assumptions on the variances. In all three different scenarios the test statistic of interest is the Likelihood Ratio Test (LRT), an intuitive and powerful tool in hypothesis testing. In both [9] and [32] an entire chapter is dedicated to LRT developments and its use for testing order restrictions hypothesis under the normality assumption and known variance ratio. Using the same notation used in Section 5.3, we wish to test

$$H_0: \quad \mu_1 = \mu_2 = \cdots = \mu_k$$

against monotonicity of means

$$H_1: \quad \mu_1 \leq \mu_2 \leq \cdots \leq \mu_k. \tag{5.4.1}$$

The likelihood ratio test for H_0 against H_1 can be defined as:

$$\Lambda = \frac{\max_{(\boldsymbol{\mu}\in H_0;\boldsymbol{\sigma^2})} L(\boldsymbol{y_1},\boldsymbol{y_2},\dots,\boldsymbol{y_k};\boldsymbol{\mu},\boldsymbol{\sigma^2})}{\max_{(\boldsymbol{\mu}\in H_1;\boldsymbol{\sigma^2})} L(\boldsymbol{y_1},\boldsymbol{y_2},\dots,\boldsymbol{y_k};\boldsymbol{\mu},\boldsymbol{\sigma^2})} \tag{5.4.2}$$

where $\boldsymbol{y_i} = (y_{i1},\dots,y_{in_i})'$, $\boldsymbol{\mu} = (\mu_1,\dots\mu_k)'$ and $\boldsymbol{\sigma^2} = (\sigma_1^2,\dots\sigma_k^2)'$. It rejects the null hypothesis for small values of Λ or alternatively for large values of $-2\log\Lambda$. The convenience

in using this other form lies on the analogy with the χ^2 statistic used to test against the alternative hypothesis $\bar{H}_0$, that not all μ_i's, $i = 1,\dots,k$, are the same.
In the following subsections more explicit expressions for Λ are given depending on the specific assumptions on means and variances.

LIKELIHOOD RATIO TEST WITH KNOWN VARIANCE RATIO

As in Section 5.3 let y_{ij} $j = 1,2,\dots n_i$, $i = 1,2,\dots k$ be independent observations, normally distributed with unknown mean μ_i and variances $\sigma_i^2 = c_i\sigma^2$ with c_i known and σ^2 unknown. Under H_0, the maximum likelihood estimate of $\mu_1 = \mu_2 = \cdots = \mu_k$ is given by:

$$\hat{\mu}_{H_0} = \frac{\sum_{i=1}^k w_i \bar{y}_i}{\sum_{i=1}^k w_i} \tag{5.4.3}$$

with $w_i = \frac{n_i}{c_i}$. Under H_1 the MLE of $\boldsymbol{\mu}$ is $\hat{\boldsymbol{\mu}}^{\boldsymbol{I}}_{\boldsymbol{H_1}}$, the isotonic regression of $\bar{\boldsymbol{y}}$, with weights $\boldsymbol{w} = (w_1,\dots,w_k)'$, with respect to the simple order defined in (5.4.1).
The likelihood ratio test for H_0 against H_1, if the variances are known and $c_i = 1$ boils down to rejecting H_0 for large values of

$$-2\log\Lambda = \frac{1}{\sigma^2}\Big[\sum_{i=1}^k\sum_{j=1}^{n_i}(y_{ij}-\hat{\mu}_{H_0})^2 - \sum_{i=1}^k\sum_{j=1}^{n_i}(y_{ij}-\hat{\mu}^I_{iH_1})^2\Big] \tag{5.4.4}$$

It is easy to check that the test is equivalent to rejecting H_0 for large values of:

$$\bar{\chi}^2 = \frac{\sum_{i=1}^k \bar{\chi}_i^2}{\sigma^2} \tag{5.4.5}$$

where $\bar{\chi}_i^2 = n_i(\hat{\mu}^I_{iH_1} - \hat{\mu}_{H_0})^2$ and σ^2 is the (known) common value of the variance.
Now, let us consider the more general case, $\sigma_i^2 = c_i\sigma^2$ with $c_1, c_2, \dots c_k$ known and σ^2 unknown. The estimator of σ^2 under the null hypothesis is

$$\hat{\sigma}^2_{H_0} = \frac{\sum_{i=1}^k c_i^{-1}\sum_{j=1}^{n_i}(y_{ij}-\hat{\mu}_{H_0})^2}{N} \tag{5.4.6}$$

and under H_1

$$\hat{\sigma}^2_{H_1} = \frac{\sum_{i=1}^k c_i^{-1}\sum_{j=1}^{n_i}(y_{ij}-\hat{\mu}^I_{iH_1})^2}{N} \tag{5.4.7}$$

The likelihood ratio test rejects H_0 for small values of $\Lambda = \big(\frac{\hat{\sigma}^2_{H_1}}{\hat{\sigma}^2_{H_0}}\big)^{N/2}$ or equivalently, taking $\bar{E}^2 = 1 - \Lambda^{2/N}$, for large values of

$$\bar{E}^2 = \frac{\sum_{i=1}^k c_i^{-1}\bar{\chi}_i^2}{\sum_{i=1}^k c_i^{-1}\sum_{j=1}^{n_i}(y_{ij}-\hat{\mu}_{H_0})^2} \tag{5.4.8}$$

An extension to the multivariate case with covariance matrix Σ unknown but common can be found in [107, 129].

LIKELIHOOD RATIO TEST WITH UNKNOWN VARIANCES

In this second case, no assumptions on the variances are made. They are unknown and possibly unequal. Using the notation of Section 5.3 let y_{ij}, $j = 1,2,\ldots,n_i$, $i = 1,2,\ldots,k$ be independent observations from a univariate Normal distribution with unknown mean vector μ_i and completely unknown variances $\sigma_i^2 > 0$. Let $\hat{\boldsymbol{\mu}}^{\boldsymbol{I}}$ be the solution of the isotonic regression of $\bar{\boldsymbol{y}}$ with weights $\boldsymbol{w} = (w_1,\ldots,w_k)'$, $w_i = \frac{n_i}{\sigma_i^2}$ found used Algorithm (2.2) in Appendix A.

The first example of testing when all the variances are unknown can be found in [11] and the univariate version of the test proposed by the author is:

$$\sum_{i=1}^{k} \frac{(\hat{\mu}_i^I - \bar{y})^2 n_i}{s_i^2} \tag{5.4.9}$$

where $\bar{y} = \frac{\sum_{i=1}^k n_i \bar{y}_i}{\sum_{i=1}^k n_i}$ and $s_i^2 = \frac{\sum_{i=1}^k \sum_{j=1}^{n_i} (y_{ij}-\bar{y}_i)^2}{n_i - 1}$. This test is clearly inspired by the LRT but it is not.

Let us consider first the maximum likelihood solution $(\hat{\mu}_{H_0}, \hat{\boldsymbol{\sigma}}^{\boldsymbol{2}}_{H_0})$, $\hat{\boldsymbol{\sigma}}^{\boldsymbol{2}}_{\boldsymbol{H_0}} = (\hat{\sigma}^2_{1H_0},\ldots,\hat{\sigma}^2_{kH_0})'$ under the null hypothesis. The log-likelihood under the null hypothesis is

$$l(\mu, \boldsymbol{\sigma^2}) = \sum_{i=1}^{k} \Big\{ -\frac{n_i}{2} \ln \sigma_i^2 - \frac{1}{2\sigma_i^2} \sum_{j=1}^{n_i} (y_{ij} - \mu)^2 \Big\} + \text{c.} \tag{5.4.10}$$

Differentiating this log-likelihood with respect to μ and σ_i^2, the following $k+1$ score equations in $k+1$ unknowns emerge:

$$\begin{cases} \mu_{H_0} = \frac{\sum_{i=1}^k n_i \sigma^{-2}_{iH_0} \bar{y}_i}{\sum_{i=1}^k n_i \sigma^{-2}_{iH_0}} \\ \sigma^2_{iH_0} = \sum_{j=1}^{n_i} n_i^{-1} (y_{ij} - \mu_{H_0})^2 \quad 1 \le i \le k \end{cases} \tag{5.4.11}$$

Substituting $\boldsymbol{\sigma}^{\boldsymbol{2}}_{\boldsymbol{H_0}}(\boldsymbol{\mu})$ in Eq. 5.4.10, the profile likelihood of μ is:

$$l(\mu) = -\sum_{i=1}^{k} \frac{n_i}{2} \ln\Big(\sum_{j=1}^{n_i} n_i^{-1} (y_{ij} - \mu)^2 \Big) + c. \tag{5.4.12}$$

Theorem 5.4.1. *A maximizer of Eq. 5.4.12 over $\mathbb{R}^d$ exists and it is contained in $[\min_i \bar{y}_i, \max_i \bar{y}_i]$. Moreover, if $[\min_i \bar{y}_i, \max_i \bar{y}_i] \in [\max_{1\le i\le k}(\bar{y}_i - \bar{\sigma}_i), \min_{1\le i\le k}(\bar{y}_i + \bar{\sigma}_i)]$ then the maximizer is unique.*

Proof. Maximizing profile likelihood of μ Eq. 5.4.12 boils down to maximise the sum of functions

$$-\frac{n_i}{2} \ln(n_i(\bar{\sigma}_i^2 + (\bar{y}_i - \mu)^2)), \quad i = 1,\ldots,k. \tag{5.4.13}$$

Functions of type Eq. 5.4.13 are unimodal with mode at $\bar{y}_i$ and strictly concave on $[\bar{y}_i - \bar{\sigma}_i; \bar{y}_i + \bar{\sigma}_i]$. As the sum of unimodal functions is decreasing to the right of the rightmost mode (since all terms are decreasing) and from $-\infty$ to the leftmost mode, the sum

is increasing (as all of the functions are increasing on that set). Therefore, any maximizer of l, if it exists, belongs to the interval $[\min_i \bar{y}_i, \max_i \bar{y}_i]$. As l is continuous on $[\min_i \bar{y}_i, \max_i \bar{y}_i]$, existence of a maximizer is guaranteed.
Then if we consider the (possibly empty) interval where all the functions in Eq. 5.4.13 are strictly concave, on that interval the sum is also strictly concave. As for each i the function Eq. 5.4.13 is strictly concave on $I_i = [\bar{y}_i - \bar{\sigma}_i; \bar{y}_i - \bar{\sigma}_i]$, Eq. 5.4.12 is strictly concave on $\bigcap_{i=1}^{k} I_i$. If $[\min_i \bar{y}_i, \max_i \bar{y}_i]$ is contained in this intersection, l is strictly concave on $[\min_i \bar{y}_i, \max_i \bar{y}_i]$. Hence l has a unique maximizer on $\mathbb{R}^d$.

□

Remark: in a setting with real data, it is easy to check whether $[\min_i \bar{y}_i, \max_i \bar{y}_i] \in [\max_{1\le i\le k}(\bar{y}_i - \bar{\sigma}_i), \min_{1\le i\le k}(\bar{y}_i + \bar{\sigma}_i)]$ and hence to determine whether the maximum is unique.
However, as seen from Eq. 5.4.11 the MLE estimate $(\mu, \boldsymbol{\sigma^2})$ has no closed form expression. Therefore, in [44] and [100] two different methods for finding the optimal solution are proposed. The first is an iterative procedure based on the Newton-Raphson method. A reasonable initial value for $\hat{\mu}_{H_0}^{(0)}$ is the so called Graybill-Deal estimator [45] $\hat{\mu}_{(GD)} = \frac{\sum_{i=1}^{k}(n_i \bar{y}_i)/\bar{s}_i^2}{\sum_{i=1}^{k} n_i/\bar{s}_i^2}$ with $\bar{s}_i^2 = \frac{\sum_{j=1}^{n_i}(y_{ij}-\bar{y}_i)^2}{n_i - 1}$. The convergence speed of the algorithm strongly depends on the initial values. The second method is based on the profile likelihood approach. The authors in [100] propose the bisection method for finding the zero of the profile likelihood with respect to μ_{H_0}. Under H_1 we use as estimates of $(\boldsymbol{\mu_{H_1}}, \boldsymbol{\sigma^2_{iH1}})$, $(\hat{\boldsymbol{\mu}}^{\boldsymbol{I}}, \hat{\boldsymbol{\sigma}}^{\boldsymbol{2}})$ found using the iterative procedure described in Section 5.3.
The likelihood ratio test when the variances are completely unknown can be expressed as:

$$\tilde{\Lambda} = \prod_{i=1}^{k} \left(\frac{\hat{\sigma}^2_{iH_0}}{\hat{\sigma}^2_{iH_1}} \right)^{-\frac{n_i}{2}}$$

Therefore, as in the previous case, the test rejects for small values of $\tilde{\Lambda}$ or equivalently for large values of $-2\log\tilde{\Lambda}$.

LIKELIHOOD RATIO TEST WITH ORDERED VARIANCES

Using the notation of Section 5.3 let y_{ij}, $j = 1, 2, \ldots, n_i$, $i = 1, 2, \ldots, k$ be independent observations from Normal distributions with mean vector μ_i and variances σ_i^2. As in the previous case, the first step is the estimation of $(\mu, \boldsymbol{\sigma^2})$ under the null hypothesis. In this case we need to maximise Eq. 5.4.10 under the restriction

$$\sigma_1^2 \ge \sigma_2^2 \ge \cdots \ge \sigma_k^2 > 0. \tag{5.4.14}$$

Theorem 5.4.2. *Suppose that for* $1 \le i \le k$, $\bar{\sigma}_i^2 > 0$. *Then there exists a maximizer of Eq. 5.4.10 under constraints Eq. 5.4.14.*

Proof. First consider the situation for fixed $\boldsymbol{\sigma^2}$ with $\sigma_i^2 > 0$ for all i. Differentiating Eq. 5.4.10 with respect to μ yields the equation

$$\sum_{i=1}^{k} \frac{n_i(\bar{y}_i - \mu)}{\sigma_i^2}$$

This shows, that for this $\boldsymbol{\sigma^2}$, the (unique) maximizer of Eq. 5.4.10 in μ is given by the following weighted sum of level-means,

$$\hat{\mu}(\boldsymbol{\sigma^2}) = \frac{\sum_{i=1}^{k} n_i \sigma_i^{-2} \bar{y}_i}{\sum_{i=1}^{k} n_i \sigma_i^{-2}}$$

Consequently, $\min_i \bar{y}_i \leq \hat{\mu}(\boldsymbol{\sigma^2}) \leq \max_i \bar{y}_i$, bounding the set of possible maximizers of Eq. 5.4.10 in μ irrespective of the precise value of $\boldsymbol{\sigma^2}$.
Now, given any $\mu \in \mathbb{R}$, the corresponding optimal $\boldsymbol{\sigma^2}$ is the solution to the antitonic regression problem antireg($\bar{\boldsymbol{\sigma}}^2_{\boldsymbol{H_0}}, \boldsymbol{N}$) where $\bar{\boldsymbol{\sigma}}^2 = (\bar{\sigma}_1^2, \dots \bar{\sigma}_k^2)'$, $\bar{\sigma}_i^2 = \frac{\sum_{j=1}^{n_i}(y_{ij}-\mu)^2}{n_i}$, $\boldsymbol{N} = (n_1, \dots, n_k)'$ (see [32] Example 1.5.5). The vector to be projected has elements $\bar{\sigma}_i^2 + (\mu - \bar{y}_i)^2$. This means, that if μ is restricted to $[\min_i \bar{y}_i, \max_i \bar{y}_i]$, the coordinates to be projected all belong to the interval $[\min_i \bar{\sigma}_i^2, \max \bar{\sigma}_i^2 + (\max \bar{y}_i - \min \bar{y}_i)^2]$. So, if μ ranges over $[\min_i \bar{y}_i, \max_i \bar{y}_i]$, the optimal $\boldsymbol{\sigma^2}$ is also contained in a the closed bounded region $[\min_i \bar{\sigma}_i^2, \max \bar{\sigma}_i^2 + (\max \bar{y}_i - \min \bar{y}_i)^2]^k$. By our assumption that all $\bar{\sigma}_i^2 > 0$, the MLE exists being a maximizer of a continuous function on a compact set in $\mathbb{R} \times \mathbb{R}^k$ □

If we consider this case as a special case of the case considered in [138] the solution is unique if Condition 5.3.2 holds. Given that the solution is not in a closed form, we use an iterative procedure to approximate the solution. As a starting value $\hat{\mu}^{(0)}$, a modified version of the Graybill-Deal estimator of the common mean when the variances are subject to order restrictions proposed in [94] appears to be a good choice:

$$\hat{\mu}_{(I)} = \frac{\sum_{i=1}^{k} w_i \hat{\tau}_i \bar{y}_i}{\sum_{i=1}^{k} w_i \hat{\tau}_i} \tag{5.4.15}$$

where $\hat{\tau}_i$ is the isotonic regression of $(\boldsymbol{t}, \boldsymbol{N})$ where $\boldsymbol{t} = (t_1, \dots t_k)'$, $t_i = \frac{1}{s_i^2}$.
Under H_1 we use as estimates of $(\boldsymbol{\mu_{H_1}}, \boldsymbol{\sigma^2_{iH1}})$, $(\hat{\boldsymbol{\mu}}^{\boldsymbol{I}}, \hat{\boldsymbol{\sigma}}^{\boldsymbol{2I}})$ found using the iterative procedure described in Section 5.3.
In contrast with the previous cases, it is not possible to further reduce the expression of the LRT because

$$\exp\left\{\frac{1}{2}\sum_{i=1}^{k}\sum_{j=1}^{n_i}\frac{(y_{ij}-\hat{\mu}_{H_0})^2}{\sigma^2_{H_0}}\right\}$$

does not reduce to a constant. The same holds under H_1. Therefore the LRT in this case can be computed by substituting the solutions obtained via the iterative procedure under H_0 and H_1 in the generic expression given in Eq. 5.4.2:

$$\Lambda^I = \frac{L(\hat{\mu}_{H_0}, \hat{\boldsymbol{\sigma}}^{\boldsymbol{2I}}_{\boldsymbol{H_0}})}{L(\hat{\boldsymbol{\mu}}^{\boldsymbol{I}}_{\boldsymbol{H_1}}, \hat{\boldsymbol{\sigma}}^{\boldsymbol{2I}}_{\boldsymbol{H_1}})} \tag{5.4.16}$$

5.5. BOOTSTRAP APPROACH

In order to determine the significance of the various test statistics proposed in the previous sections, we need the null hypothesis distribution of the test statistics. The main

distributional results concerning $\bar{\chi}^2_k$ and $\bar{E}^2_k$, the test statistics derived in the known variance ratio case, are contained in [9] (Theorems 3.1-3.2). However, problems related to the value of k can arise in the analytical derivation of the p-values. Numerical approximation can be necessary, especially if $k > 4$ and if the variation in the range of the weights is not 'moderate' [120, 141].
Furthermore, in the case of completely unknown variances, the null distribution depends on the unknown variances. When analytical derivation of the null distribution is particularly complex or not possible, bootstrap methodology is a good option. Therefore, we propose both a parametric and a non-parametric bootstrap approach that can be easily employed for finding approximate p-values taking into account the different assumptions on the variances. For overcoming the complex derivation when the variances are unknown, bootstrap procedures have been proposed in the literature [93, 11]. In particular, in [93] an interesting review of the methods used to approximate the null distribution of the test statistic under H_0 and the restrictive normality assumption (with which we will not deal in this Chapter) is reported. Moreover the authors propose both a parametric and non-parametric bootstrap approach for the likelihood ratio test null distribution for one sided hypothesis testing for means in a multivariate setting [93]. Also in [11] a bootstrap approach to test the homogeneity of order restricted mean vectors when the covariance matrices are unknown is used. In line with those previous approaches, here we propose two general bootstrap procedures, parametric and non-parametric, that can be used for testing the null hypothesis taking into account the various assumptions on the variances.

PARAMETRIC BOOTSTRAP

Algorithm:

(1) Obtain the estimates $\hat{\boldsymbol{\mu}}^{\boldsymbol{I}}_{\boldsymbol{iH_1}}$ and $\hat{\mu}_{H_0}$ using the original data and compute the observed value of the test statistic of interest $LRT^{(0)}$ ($\bar{\chi}^{2(0)}$, $\bar{E}^{2(0)}$, $\bar{\Lambda}^{(0)}$ or $\Lambda^{I(0)}$).

(2) Generate, for $1 \le i \le k$, $1 \le j \le n_i$ $\boldsymbol{Y^*_{ij}} \sim N\big(\hat{\mu}_{H_0}, \sqrt{\sigma^2_{iH_0}}\big)$, independently.

(3) For $(\boldsymbol{Y^*_i}, \ldots, \boldsymbol{Y^*_k})$ obtain the estimates $\hat{\boldsymbol{\mu}}^{\boldsymbol{I}*}_{\boldsymbol{i}}$ and $\hat{\mu}^*$ and compute the bootstrap test statistic of interest LRT^*

(4) Repeat **(2)**-**(3)** for a sufficient large number of times M

The bootstrap approximation of the p-value is the given by:

$$p \approx \frac{\#(LRT^* > LRT^{(0)})}{M} \tag{5.5.1}$$

and the null hypothesis is rejected whenever this p-value is less than the nominal level α.
Step (2) is the key step, in which the assumption on the variances play a crucial role. It is interesting to notice that the above procedure can be further simplified. In fact, we can instead of generating individual observations, directly generate empirical means $\bar{y}_i = Z_i * \frac{\sigma}{\sqrt{n_i}}$, with Z_i Standard Normally distributed.

NON-PARAMETRIC BOOTSTRAP

The non-parametric version of the bootstrap releases the normality assumption of the bootstrap samples. However a relatively large sample size is required for the following approach.

Algorithm:

(1) Obtain the estimates $\hat{\boldsymbol{\mu}}^{\boldsymbol{I}}_{\boldsymbol{iH_1}}$ and $\hat{\mu}_{H_0}$ using the original data and compute the observed value of the test statistic of interest $LRT^{(0)}$ ($\bar{\chi}^{2(0)}$, $\bar{E}^{2(0)}$, $\tilde{\Lambda}^{(0)}$ or $\Lambda^{I(0)}$).

(2) Standardize the original y_{ij} to obtain 'standardized residuals' $z_{ij} = \frac{y_{ij}-\bar{y}_i}{\sqrt{s_i^2}}$

(3) Combine all z_{ij} observations from $(1 \leq i \leq k; 1 \leq j \leq n_i)$ into a vector of length $\sum_{i=1}^{k} n_i$ and draw k simple random samples z^*_{ij} with replacement each of respective sizes $(n_1, n_2, \ldots, n_k)$

(4) Transform z^*_{ij} to $y^*_{ij} = z^*_{ij} \cdot \tilde{\sigma}_{iH_0} + \hat{\mu}_{H_0}$

(5) For each bootstrap sample y^*_{ij} $(1 \leq i \leq k; 1 \leq j \leq n_i)$ obtain the estimates $\hat{\boldsymbol{\mu}}^{\boldsymbol{I*}}_{\boldsymbol{iH_1}}$ and $\hat{\mu}^*_{H_0}$ and compute the bootstrap test statistic of interest LRT^*

(6) Repeat **(3)**-**(4)**-**(5)** for a sufficient large number of times M

The bootstrap approximated p-value is defined as in the parametric case Eq. 5.5.1.

5.6. APPLICATION

One of the most common ways for investigating strength and ductility of metallic materials is by performing a tensile test. A tensile test is an experiment in which a uniaxial force is applied to the test sample causing deformation of the material, temporarily (elastic behaviour), permanently (plastic behaviour) and eventually its fracture [27]. Data used in this Chapter are image data of the microstructure of the material subjected to a plastic strain (deformation) of 0.139 obtained performing a uniaxial tensile test in which force is applied to the test sample with respect to just one specific axis (Fig. 5.1). At a microstructure level the deformation of the material corresponds to displacements in the lattice structure and in the possible appearance of Geometrically Necessary Dislocations (GNDs). The material used is the same described in Chapter 4, more specifically an annealed AISI420 ferrite stainless steel with $M_{23}C_6$ carbides. The aim is to investigate the carbide effect on the GNDs formation. Kernel Average Misorientation (KAM) is used as a proxy of the GNDs. In Figure 5.2 the KAM is represented by red filaments, the blue lines represent the ferrite grain boundaries, carbides are the black dots. The results of the estimation in the three different scenarios faced in Sections 5.3 are summarised in Table 5.1. Modelling the relationship between KAM and carbides and more generally understanding its inhomogeneous distribution over the microstructure is now the main aim and it can be considered a starting point for finding a stochastic model for predicting mechanical properties from 2D microstructure images. We apply estimation procedures and perform tests under order restrictions, three different univariate isotonic regressions



Figure 5.1: Tensile testing machine

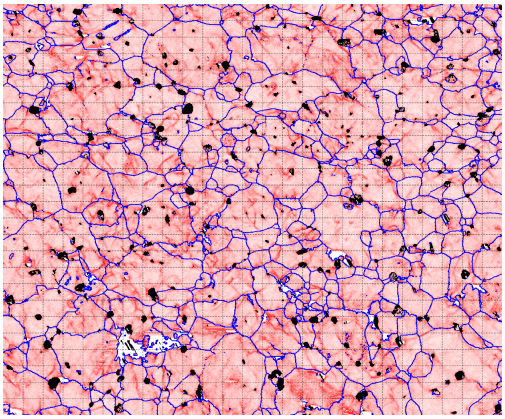


Figure 5.2: Microstructure image showing the KAM at strain level 13.9 % (overlapped grid of 25 × 25).

according to the assumption on the variances.
The first step for obtaining the data in the most suitable form for the analysis is 'overlaying' a grid over the image. In Figure 5.2 a 25 × 25 grid is added to the image. With y_{ij}, we denote the mean KAM value of the jth square of the grid of the image taken in which i carbides are observed. The explanatory variable X in all three isotonic regressions is the number of carbides observed in the grid squares. A plot of the data is shown in Figure

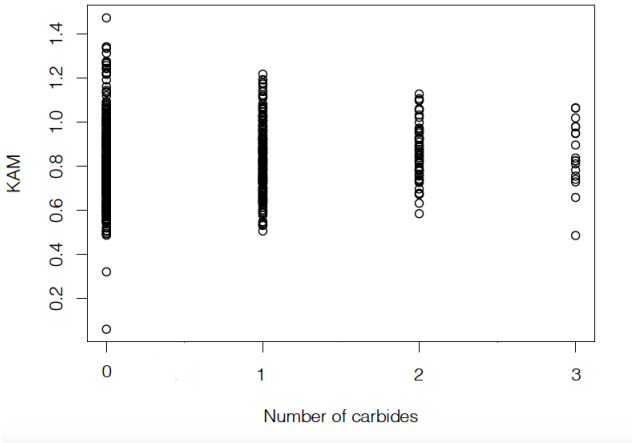


Figure 5.3: Plot of KAM and Number of carbides for the 625 squared areas of Figure 5.2

5.3.

We wish to test the null hypothesis that the expected KAM is the same in all the squares of the gird, regardless the numbers of carbides observed in the grid. The alternative hypothesis

$$\mu_0 \leq \mu_1 \leq \mu_2 \leq \mu_3. \tag{5.6.1}$$

represents the idea that KAM tends to be higher in areas where more carbides are observed. Moreover, in the ordered variances case, we assume that

$$\sigma_0^2 \geq \sigma_1^2 \geq \sigma_2^2 \geq \sigma_3^2 > 0. \tag{5.6.2}$$

This is in accordance with what we see in Figure 5.3. In fact, the idea behind this assumption is that in areas in which less carbides are observed GNDs have more freedom to move, resulting in increments in dispersion. In Table 5.2, the results of testing the null hypothesis are shown. For computing $\chi^{2(0)}$ and $\bar{E}^{2(0)}$, the variance ratio is supposed to be known. In the specific case, we assume that the KAM total variance for the whole image is the real known variance and that $c_i = \frac{\bar{\sigma}_i^2}{\sigma^2}$. For computing both the parametric and non-parametric p-values, the two different bootstrap approaches described in Section 5.5 have been used and M, the number of replications, is taken equal to 20000. Independent of the knowledge or assumptions on the variances, the conclusion is the same and leads to the rejection of the null hypothesis.

5.7. CONCLUSIONS

This Chapter presents three different models involving order restrictions and within these models the ML estimators and Likelihood Ratio tests for the homogeneity of the means against monotonicity are introduced and studied. Prior knowledge given by physical relations or intuition is not often exploited in statistical studies about materials and this

Table 5.1: Values of estimated means and variances of the KAM conditioned on the number of carbides visible in a square of a grid 25×25 according to different order restrictions assumptions (13.9% Strain)

	0	1	2	3
$\bar{y}$	0.815	0.833	0.870	0.854
$\bar{\sigma}^2$	0.035	0.024	0.017	0.022
s^2	0.035	0.024	0.017	0.023
$\hat{\mu}^I_{(1)}$	0.815	0.833	0.867	0.867
$\hat{\mu}^I_{(2)}$	0.815	0.833	0.867	0.867
$\hat{\sigma}_{(2)}$	0.035	0.024	0.017	0.022
$\hat{\mu}^I_{3)}$	0.815	0.833	0.866	0.866
$\hat{\sigma}^I_{(3)}$	0.035	0.024	0.018	0.018
n	340	211	54	18

Table 5.2: Estimated values for the four different likelihood ratio test with the corresponding parametric and non-parametric p-values

	$\hat{\mu}_{H_0}$	Test Statistic	p-value (parametric)	p-value (non-parametric)
$\tilde{\chi}^{2(0)}$	0.827	5.760	0.0323	0.0310
$\tilde{E}^{2(0)}$	0.831	0.0121	0.0112	0.0085
$-2\log\tilde{\Lambda}$	0.831	7.330	0.0178	0.0222
$\Lambda^{I(0)}$	0.831	7.105	0.0212	0.0251
	0	1	2	3
$\hat{\sigma}^2_{H_0}$	0.035	0.024	0.018	0.022
$\hat{\sigma}^{2I}_{H_0}$	0.035	0.024	0.019	0.019

can lead to less efficient methods that produce less accurate results. After having described the estimation procedures and highlighted the influence of prior knowledge of the variances, we propose the likelihood ratio test as test statistic for testing the homogeneity of means. In the case of unknown variances and ordered variances, heteroskedasticity plays a crucial role also under the null hypothesis, leading to different estimates of the common mean under H_0. Results on existence and uniqueness of the maximum likelihood estimates in these last two cases are derived. Furthermore, two different bootstrap approaches are proposed for approximating the null distribution of the test statistic under the different assumptions on the variances. The proposed tests are applied to a real data example of a metal microstructure, showing evidence that the so-called KAM tends to be higher in regions of the microstructure where more carbides are observed. In fact, incorporating reasonable intuition about the order of means and the variances order in this context helps understanding the evolution of complicated structure of dislocations in metals and its effect on the hardening behaviour of the material during deformation.

6

3D Virtual Experiments

Multiple factors, as measurement accuracy, limitations in controlling microstructural changes of all individual constituents during the deformation of a material and lack of data due to high costs of experiments make the identification of a physical relation between microstructure features and mechanical properties very challenging. In this Chapter we propose a completely simulation-based approach. Digital twins of different microstructures with different carbides volume fractions and different textures are generated. Multi-Level Poisson Voronoi diagram is adopted as model. The resulting virtual microstructures are used as samples for virtual tensile tests. The stress–strain curves corresponding to the different volume fractions of carbides and different textures are studied. Two different approaches are employed for understanding how the different microstructural characteristics relate to the mechanical behaviour of the material. The first is to construct a function ad hoc piecewisely defined with change points based on the different stages observed during a tensile test. The characteristic parameters of the resulting function are then analysed as function of the carbides intensity and texture. The latter treats the data as functional data and uses functional principal component analysis to describe the variation among the functions in terms of carbide intensity and texture.

Difficulties strengthen the mind, as labor does the body.

Lucius Annaeus Seneca

6.1. INTRODUCTION

It is well known that strain development in metallic alloys is critically affected by the microstructural characteristics such as grain size of the matrix phase (size of the cells belonging to the principal phase) as well as size, density and nature of existing precipitates. These characteristics, influencing the dislocation motion in the structure, play a fundamental role in the mechanical behaviour of the metallic alloys. Metal microstructures may indeed consist of hard particles embedded in a relatively soft (plastic) matrix, or viceversa a soft phase embedded in a matrix with significantly higher hardness [5]. Understanding the contribution and the interaction among grains and precipitates of different phases can lead to the design of superior materials with desired mechanical properties [156].
Predicting macroscopic material properties and relating them to microstructures features has been the focus of many studies [7, 19, 54, 123, 156, 165].
However, controlling all the microstructure parameters that influence the mechanical behaviour of the material is a too ambitious aim in real experiments. Therefore, simulations and statistics may help in this respect. In this Chapter, a digital approach is proposed and it can be summarised in three main steps.
As in all simulation-based studies, the first step is creating a virtual microstructure, or in other words a 'digital twin' of the physical microstructure.
As explained in Chapter 4, digitally representing microstructures, using statistical and stereological models (SSRVE) or empirical based reconstruction (RVE), is a fundamental step for simulating the mechanical behaviour of the material.
One of the advantages of virtually generating microstructures is the possibility of testing materials with hypothetical microstructure characteristics that can improve the mechanical response of the material.
Once the digital twin microstructure is ready, the second step is to perform the virtual experiment. For this purpose a software that combines a crystal plasticity model with a Spectral Solver, called DAMASK (Düsseldorf Advanced Material Simulation Toolkit,[123]) is used. Finally, the last step is assessing the validity of the outcome comparing it to real experiments results.
In this Chapter, a virtual tensile test is performed for the investigation of mechanical properties of a AISI420 stainless steel with $M_{23}C_6$ carbides precipitates. We start with the description of the virtual experiment (Section 6.2). Using Multi-Level Poisson Voronoi diagrams as geometrical model for the digital microstructures, 70 Statistically Similar RVEs are produced. The difference is in the texture (10 different random orientations distributions) and in the carbides volume fraction (7 different values for the first level cells intensity of a Multi-Level Poisson Voronoi diagram with two phases). Then, the virtual tensile test is performed using DAMASK. The main outcomes of the experiments are stress–strain curves corresponding to the different microstructures. After having reviewed the main characteristics of a stress–strain diagram, some of the classical models used for representing the stress–strain function are discussed (Section 6.3). The influence of the type of tensile test performed, the temperature, the texture and the volume phase fractions are examples of the parameters influencing the resulting stress–strain curve. The high number of parameters and the interrelation of multiple factors makes the identification of a unique function for representing the stress–strain behaviour of

metals (almost) impossible to achieve. In this Chapter, two new modelling approaches for understanding the influence of the different carbide intensities are introduced. The first is an approach 'ad hoc', based on a priori physical knowledge. The assumption is that a typical stress–strain curve can be represented by different segments correspondent to different stages of the tensile test: elastic deformation, plastic deformation, rupture. For determining the points at which the function changes, an algorithm based on a "leave-one-out" maximisation procedure is proposed. The dependence of the parameters of the resulting function on the value of the carbide intensity is then studied. Also the texture seems to have an influence on the resulting stress–strain curve (Section 6.4). The second approach is a functional approach, in which the stress–strain curves are used as input of Functional Principal Component Analysis (FPCA) (Section 6.5). FPCA is one of the most common tools in Functional Data Analysis, used for understanding the different sources of variability among the functions. Here, we propose a modified version of the classical approach in which the functions are not centred on the mean, but on the mean stress–strain curve one would observe for a microstructure without carbides. Conclusions and further developments are discussed in Section 6.6.

6.2. VIRTUAL TENSILE TEST

As previously stated, the virtual approach proposed in this Chapter consists of three main steps.

The first step is generating a virtual microstructure. In Chapter 4, the main methods used for digital representation of metal microstructures are reviewed. In particular, two examples of digital twins for describing the microstructure of AISI420 stainless steel with $M_{23}C_6$ carbides precipitations are presented (Sections 4.2-4.3). Here, the Statistically Similar Representative Volume Element (SSRVE) approach is followed. With the aim of understanding the relation between carbides presence and material's strengthening, SSRVEs with increasing carbides volume fractions are generated. The Multi-Level Poisson Voronoi diagram is used as model (Section 4.3.1). The value of the intensity of the first level cells decomposed in $\lambda_1 = \lambda_1^f + \lambda_1^c$ is taken equal to 3; λ_2, the intensity of the second level grains is instead taken equal to 0.5. Taking into account that the observed volume fraction of carbides in stainless steels is usually in the range $[0.03, 0.11]$, 7 different values are considered for λ_1^c, namely: 0, 0.01, 0.03, 0.05, 0.07, 0.09, 0.11. The virtual mi-

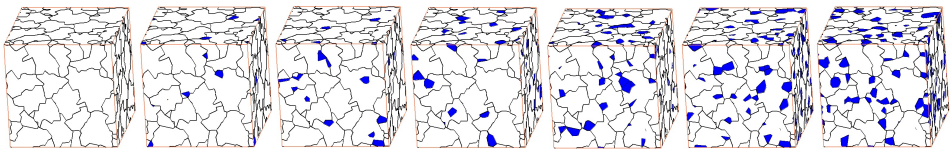


Figure 6.1: 3D Multi-Level Poisson Voronoi diagrams with increasing level of λ_1^c: (a) $\lambda_1^c = 0$, (b) $\lambda_1^c = 0.01$, (c) $\lambda_1^c = 0.03$, (d) $\lambda_1^c = 0.05$, (e) $\lambda_1^c = 0.07$, (f) $\lambda_1^c = 0.09$, (g) $\lambda_1^c = 0.11$

crostructures shown in Figure 6.1 differ just for the carbides intensity: ferrite grain size and ferrite grain orientations are kept the same. This generation is repeated 10 times,

hence in total 70 microstructures are considered. While the ferrite grain size is kept constant, not changing the value of the intensity of the second level grains, the orientations of the grains are randomly assigned. In total 10 different random textures are considered. Although texture effect is not the principal scope of this Chapter, its possible influence has to be taken into account. In fact, during deformation the grains in a polycrystalline material tend to rotate towards stable orientations [106] and specific initial texture conditions can lead to different mechanical responses.
The strain and stress development in the different digital versions of the microstructure is simulated combining a crystal plasticity model and a spectral solver based on the Fast Fourier Transform (FFT) implemented in the DAMASK software. The intricate stress interactions between the grains of a polycrystalline material are modelled numerically using the spectral element (SE) method. In the following subsection, only the constitutive equations for the elastic and plastic deformation are broadly presented.

DAMASK

The Düsseldorf Advanced Material Simulation Kit (DAMASK) is an an open source software based on a Crystal Plasticity methods which allows to conduct advanced microstructural and mechanical property simulations. Crystal Plasticity (CP) methods, which are based on the behaviour of an assembly of single crystals, have been successfully applied in predicting the mechanical response of polycrystals up to the industrially relevant component scale [123]. Each grain is represented by one or more finite elements; then the single elements are combined in a polycrystal structure with specific boundary conditions for which the deformation under specific constraints is simulated. The single crystal plasticity model is combined into the Spectral Element framework to define the constitutive relation at each integration point of the element. The deformation in the continuum theory of crystal plasticity is described as a multiplicative decomposition into elastic, F_e, and plastic, F_p, parts of the deformation gradient F, where the elastic part accounts for lattice distortion and rotation, and plastic defromation arises due to slip. The elastic stress is expressed in form of the 2^{nd} Piola-Kirchhoff stress $\boldsymbol{S}$ and depends only on the elastic strain expressed as the Green-Lagrange strain tensor $\boldsymbol{E}$ and the material specific stiffness C, $\boldsymbol{S} = C : \boldsymbol{E}$, $\boldsymbol{E} = 1/2(F^e F^{eT} - 1)$. For cubic crystals, the elastic stiffness matrix is assumed to be composed of three independent terms, C_{11}, C_{12} and C_{44}. It is worth to note that the effect of dislocations is not included in this model. The evolution of plastic strain is given by:

$$\dot{F}_p = L_p F_p \tag{6.2.1}$$

where L_p is the plastic velocity gradient. A widely adopted phenomenological description for the hardening is used, which is based only on slip of multiple slip systems β_i. The evolution of critical shear stress[1], $\dot{\tau}_C^{\beta}$, i.e. the hardening, of individual slip systems in a single crystal is given by:

$$\dot{\tau}_C^{\beta} = \sum_{\eta} h_{\beta\eta}\dot{\gamma}^{\eta} \tag{6.2.2}$$

[1]The shear stress is the force tending to cause deformation of a material by slippage along a plane or planes parallel to the imposed stress.

The instantaneous slip-system hardening moduli $h_{\beta\eta}$, in general, depend upon the history of slip and provides information about additional hardening caused by interactions of fixed slip systems β and active slip systems η. $h_{\beta\eta}$ is determined by the following expression:

$$h_{\beta\eta} = q^{\beta\eta}[h_0(1-(\tau_C^\eta)/\tau_{sat})^a] \tag{6.2.3}$$

The parameters h_0, τ_C^η and τ_{sat} are respectively the reference hardening, the critical slip resistance and the saturation shear stress, and depend on the crystal structure and the slip system. Parameter a has not a direct physical meaning, but has a direct influence on the development of hardening and it is usually taken $a \geq 1$. The latent hardening parameter, $q^{\beta\eta}$, defines the interaction between system β and η and is set to 1, if β and η are coplanar, otherwise $q^{\beta\eta} = 1.4$. The shear strain rate $\dot{\gamma}^\eta$ of the system η is restricted by it resolved shear stress, τ^η, and τ_C^η:

$$\dot{\gamma}^\eta = \dot{\gamma}_0|\tau^\eta/\tau_C^\eta|^{1/n}\text{sign}(\tau^\eta) \tag{6.2.4}$$

where n is related to the strain rate sensitivity of slip and $\dot{\gamma}_0$ is the reference shear rate, being both variables specific of the material. The shear rates of all slip systems can be then used to determine the plastic velocity gradient:

$$L_p = \sum_{\beta=1}^{N} \dot{\gamma}^\eta m_\beta \otimes n_\beta \tag{6.2.5}$$

where N denotes the number of slip systems ($N = 12$ for iron $\{110\}_{bcc}$ and $N = 12$ for $M_{23}C_6$ carbides $\{111\}_{fcc}$), m is the normalized slip direction and n the unit normal of the slip plane. For a complete description of simulation procedure, the reader is referred to [123]. The materials parameters required for the simulation have been obtained and optimised and their values are reported in Table 6.1. The calibration of the crystal plasticity

Table 6.1: Materials parameter for DAMASK model implementation

(a) Ferrite		(b) Carbides	
N_{slip}	12	N_{slip}	12
C_{11}	233×10^9GPa	C_{11}	550.8×10^9GPa
C_{12}	135×10^9GPa	C_{12}	225.9×10^9GPa
C_{44}	118×10^9GPa	C_{44}	140×10^9GPa
$\dot{\gamma}_0$	0.001s^{-1}	$\dot{\gamma}_0$	0.001s^{-1}
n	110	n	200
τ_C^η	77×10^6MPa	τ_C^η	1600×10^6MPa
τ_{sat}	220×10^6MPa	τ_{sat}	1800×10^6MPa
h_0	2370×10^6GPa	h_0	20000×10^6GPa
a	1.6	a	1.1

constitutive parameters for ferrite is performed based on strain-stress data from tensile tests (better discussed in the next Section 6.3), obtained using the RVE method described in Section 4.2 (see Figure 6.2). Finding experimental measurements of the mechanical

properties of single crystal of $M_{23}C_6$ carbide is more challenging and thus, a rather qualitative choice of material parameters has been made, based on previous results in the literature [80, 66] and on arbitrary selection trying to emulate a particle exhibiting high hardening [58].
Once the crystal plasticity model and the parameters are set, the virtual tensile test is performed. The most commonly used test is the uniaxial tensile test in which force is applied to the test sample with respect to just one specific axis causing deformation of the material, temporarily (elastic behaviour) and permanently (plastic behaviour) and eventually its fracture. In this virtual test, uniaxial tension along x-direction is applied at a constant deformation rate of 0.0001 s^{-1} . The main output of the test are stress and strain values, plotted in the so called "stress–strain diagram". In Figure 6.3, the stress–strain curve for the 70 different microstructures are shown. From the analysis of the

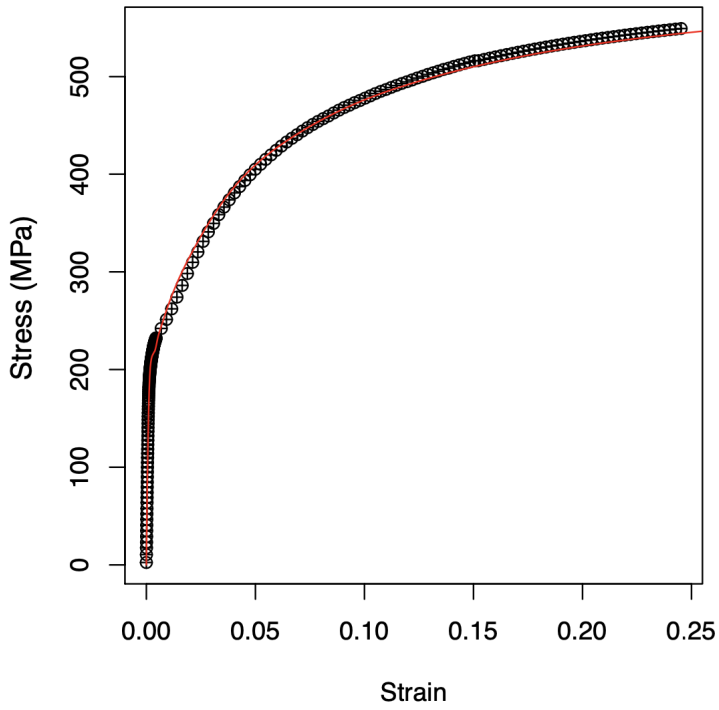


Figure 6.2: Experimental (hollow symbol) and simulated (red line) stress–strain obtained at constant deformation rate of 0.0001 s^{-1}

stress–strain curve several insights about mechanical properties of the materials can be achieved. More details are given in the next Section 6.3.

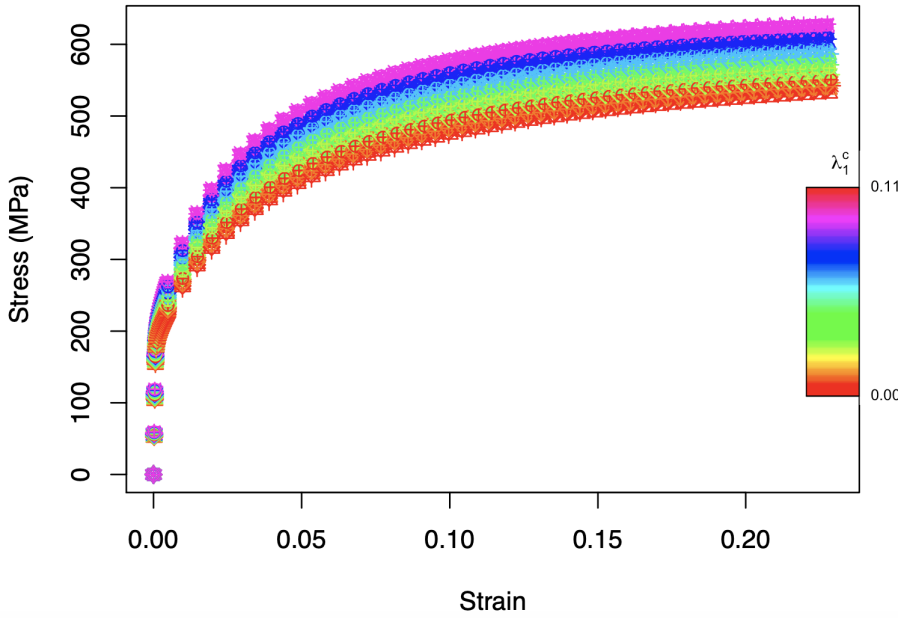


Figure 6.3: Stress–Strain curves. Different colours indicating different values of the intensity parameter of the carbides, different symbols indicating different textures.

6.3. STRESS–STRAIN DIAGRAM

Tensile testing is one of the most common ways for investigating strength, ductility and in general loadability (the ability of a material to support a stress) of metallic materials [27]. In this section, a basic explanation of the stress–strain diagram is presented. From the stress–strain diagram, several mechanical properties, such as elasticity, strength, brittleness, can be determined.

During a uniaxial tensile test, as previously stated, an increasing (ϵ) is applied (x-axis) and the resulting stress (σ) in the material is recorded and plotted in an XY-plane (Fig. 6.4). Various formulas have been developed to describe stress–strain curves of metals [76]. However, a unified formula that describes accurately the material's behaviour in the full range of the experiment is (almost) impossible to obtain [152]. In fact, the overall shape of the curve depends on several factors such as the material considered and the temperature, at the macro-scale. Moreover, the strain hardening behaviour involves a complex interaction among various factors also at the micro-scale. Grain size, dislocations, volume fractions and crystallographic orientations are aspects that can influence the shape of the curve. However, there are some recurrent features in every stress and strain diagram. As shown in Figure 6.4, points of interest of a general stress–strain curve are: the proportionality limit, the offset yield, the elastic deformation limit (yield point), the maximum tensile strength and the fracture or rupture point. These points correspond to different phases or regions in which the material behaves differently.

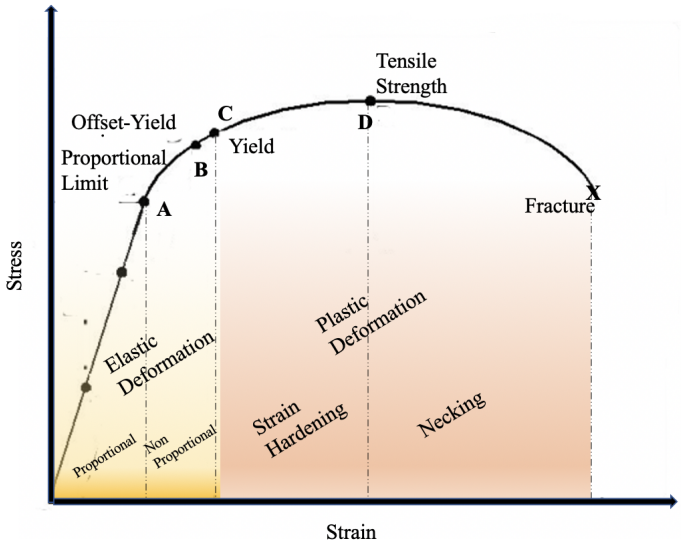


Figure 6.4: Stress–Strain Diagram

At the start of a tensile test, stress and strain are proportionality (elastic deformation - proportionality region). The material follows the well-known Hooke's Law [63]. The limiting point beyond which stress and strain are not proportional anymore is the proportionality limit (Point A Fig. 6.4). Beyond the proportionality limit, elastic deformation still takes place but greater elongation occurs in this section under increasing applied force (elastic deformation - proportionality region). The end of the elastic region of the stress–strain diagram is the yield point also called elastic limit (Point C Fig. 6.4). Problems in the determination of the proportional and elastic limit can occur due to measurements precision, therefore an offset yield strength is used for increasing reproducibility (Point B Fig. 6.4). This point is defined as the stress corresponding to the intersection point between a straight line parallel to the initial proportional line with an offset given by the strain equal to 0.002. After the yield point the plastic region begins, where the material deforms permanently. In the first part of the plastic region strain hardening[2] usually occurs. The maximum point in the plastic region is called tensile strength or ultimate strength (Point D Fig. 6.4). After this point, the materials starts to neck. The stress in fact is applied in a much smaller cross-sectional area of the material. The diagram ends with the fracture of the material. In the next Section the main mathematical models used for representing the stress–strain behaviour are reviewed.

CLASSICAL MATHEMATICAL MODELS

In this Section we recall the main mathematical models used for describing the stress–strain curve. As previously mentioned, a typical stress–strain curve presents different regions corresponding to the different stages of the tensile test. Starting from the elas-

[2] Hardness increment due to plastic deformation

tic region and in particular from the first part of the elastic region, stress and strain are proportional following Hooke's Law:

$$\sigma = E\epsilon, \tag{6.3.1}$$

where E is called elastic modulus or Young's modulus [125].
This law is valid until the proportionality limit point. In most of the cases proportionality limit point, elastic limit point and offset yield point are very close[57], therefore Hooke's Law is used to describe the whole elastic behaviour. While for the elastic proportional part of the curve Eq. 6.3.1 is commonly accepted, for the other regions of the curve various formula have been proposed. In general, the plastic deformation part of the stress–strain curve of many metals can be described by a power curve relation [29]:

$$\sigma = K \cdot \epsilon^n \tag{6.3.2}$$

strain hardening exponent. The value of K provides some indication of the level of the strength of the material and of the magnitude of forces required in forming[3], whilst the value of n provides a measure of the ability of the material to retard localisation of deformation [128]. Equation 6.3.2 is also known as Hollomon equation [62]. The materials constants are usually determined by a log-log plot of the stress versus the strain in which $\log(K)$ is the intercept and n is the slope of the regression line. Hollomon equation is nowadays one of the most popular equation for describing the plastic part of the stress–strain diagram [12]. However, the resulting double logarithmic plot rarely exhibits a linear trend. Especially for stainless steel the use of Hollomon equation is considered inadequate [159]. Another common expression proposed by Ludwik [85] is:

$$\sigma = \sigma_0 + L \cdot \epsilon^q \tag{6.3.3}$$

where σ is the true stress, ϵ is the true strain, σ_0, is a type of friction stress and L and q are material constants. However, also this expression seems to don't be suitable for austenitic stainless steel [159]. A modified version of equation 6.3.2 for which its validity is generally confirmed for austenitic stainless steels also in presence of carbide precipitates [159] is proposed by Ludwigson [84]:

$$\sigma = k_1\epsilon^{n_1} + \exp(k_2 + n_2\epsilon). \tag{6.3.4}$$

In [159] the effect of grain boundary carbide in the resulting stress–strain curve is studied; the major empirical finding is that the presence of grain boundary carbide decreases n_1 and n_2, increases k_1 slightly and does not change k_2.
Another approach to characterise the full-range stress–strain curve is using segmented functions [1, 76]. Most of these formulas proposed are purely empirical descriptions of the stress–strain relationships and material specific [76].
In the next Sections, two different approaches are proposed. The first is an ad hoc approach that recalls the use of segmented function and of change point detection tools. The latter is a functional approach based on Functional Principal Component Analysis.

[3] Metal forming is a process in which the shape of the metal is changed using plastic deformation

6.4. SEGMENTED APPROACH

As seen in the previous Section, mathematically describing the full range stress–strain curve with just one expression is not an easy task. Representing the stress response to strain deformation during the different stages of the tensile test using a unique expression is hardly possible. Therefore, separate models for the stress behaviour in the elastic and in the plastic regime are usually fitted.
Inverse problem methods and curve fitting procedure are the common approaches for the estimation of the parameters of the chosen models [155]. Inspired by the approaches proposed in [1, 56, 117], we can describe the stress–strain behaviour as a function made of three/four segments representing the different deformation phases occurring during the tensile test (elastic-proportional, elastic-non proportional, plastic-strain hardening, plastic-necking, Figure 6.4). In the specific case, given that rupture (end of the plastic deformation region) is not present, three different segments are considered:

$$\begin{cases} \sigma = E\epsilon & \epsilon < \epsilon_1 \\ \sigma = K_1 \cdot \epsilon^{n_1} & \epsilon_1 \leq \epsilon < \epsilon_2 \\ \sigma = K_2 \cdot \epsilon^{n_2} & \epsilon \geq \epsilon_2. \end{cases} \tag{6.4.1}$$

The first segment up to ϵ_1 represents the elastic part described by the Hooke's Law, where E correspond to the Young's modulus. The other two segments are two non-linear functions (inspired by 6.3.2) describing the elastic part where proportionality does not hold anymore (up to ϵ_2) and the plastic deformation up to the tensile strength. The decision of using these three segments is arbitrary and different choices are possible. The aim of this Section is twofold: i) presenting a new method for estimating the parameters and the change points of a segment function (Eq. 6.4.1) using an iterative algorithm based on "leave-one-out" Mean Squared Error; ii) understanding how the increasing carbides intensity and the different textures relate to the model parameters using linear mixed models.
The streamline of the approach is now sketched. Let us consider stress data ordered by the strain and denote them by $\sigma = (\sigma_1, \ldots, \sigma_n)$. Assume the function relating stress and strain can be represented by $m+1$ distinct segments, implying that there are m change-points in the data. We let the $j-$th change point be ϵ_j with $\epsilon_1 = \epsilon_1$ and $\epsilon_{m+1} = \epsilon_n$. The $j-$th segment will consist of data points $\sigma_{\epsilon_{j-1}+1}, \ldots, \sigma_{\epsilon_j}$ for $j = 1, \ldots, m$. For such a problem, change points correspond to points in strain where the fitting of each segment of the function becomes "too poor". For the continuity constraint and for the parameter estimation Equation 6.4.1 can be rewritten as:

$$\begin{cases} \sigma = E\epsilon & \epsilon < \epsilon_1 \\ \sigma = E\epsilon_1 (\frac{\epsilon}{\epsilon_1})^{n_1} & \epsilon_1 \leq \epsilon < \epsilon_2 \\ \sigma = E\epsilon_1 (\frac{\epsilon_2}{\epsilon_1})^{n_1} (\frac{\epsilon}{\epsilon_2})^{n_2} & \epsilon \geq \epsilon_2. \end{cases} \tag{6.4.2}$$

Therefore, the parameters of interest are E (Young's Modulus), n_1 and n_2 (Hollomon strengthening coefficients).
For the first segment a simple linear regression model without intercept is used. The other two segments are non-linear. Hence, a non-linear regression estimation procedure

based on linearisation of the segments, using a logarithmic transformation is adopted [124] (Figure 6.5).

An iterative procedure based on "leave-one-out" or "add-one-in" Goodness of Fit cri-

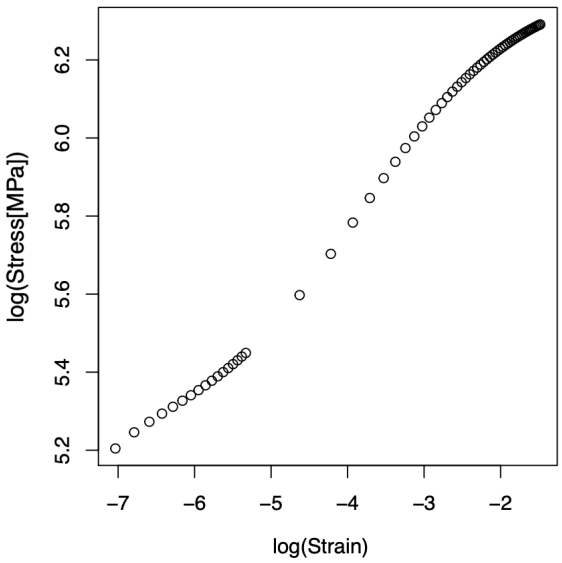


Figure 6.5: Log-log plot for one stress–strain curve excluding the first linear part of the function

terion is adopted for finding the change points among the segments. In particular, for the first linear segment, an "add-one-in" procedure based on the coefficient of determination, R^2, is used for the determining the first change point ϵ_1. In fact, it is reasonable to assume that the more observations you add, the lower the R^2 will become. Therefore, fixing a threshold t, observations keep being added until R^2 becomes lower than t (in our case $t = 0.98$). For the second piece, a "leave-one-out" Minimum Squared Error (MSE) criterion is used:

$$MSE_l = \frac{1}{n}\sum_{i=1}^{n}(\sigma_{(-l)i} - \hat{f}_m(\epsilon_{(-l)i}))^2, \ l = 1,\ldots,n$$

where $\hat{f}_m(\epsilon_i)$ the predicted response value considered the m-th segment. ϵ_2 is the strain value corresponding to the model with the highest number of observations for which the MSE value is minimum. The results are shown in Figures 6.6-6.7. In Figure 6.8 the two change points and their relation with λ_1^c and texture (indicated with different symbols) is presented: the values of the change points do not differ particularly among the curves and especially λ_1^c does not seem to be related to them. The value of ϵ_1 can be interpreted as the proportionality limit, while ϵ_2 as the yield point. Moreover, given that ϵ_2 values are very close to 0.002 the relation between yield point and off-set yield is confirmed. The next step is relating the intensity value of carbides precipitates (λ_1^c) to the parameters of the model (E, n_1, n_2).

In Figure 6.9, the estimated parameters are plotted against the observed value of λ_1^c. Both

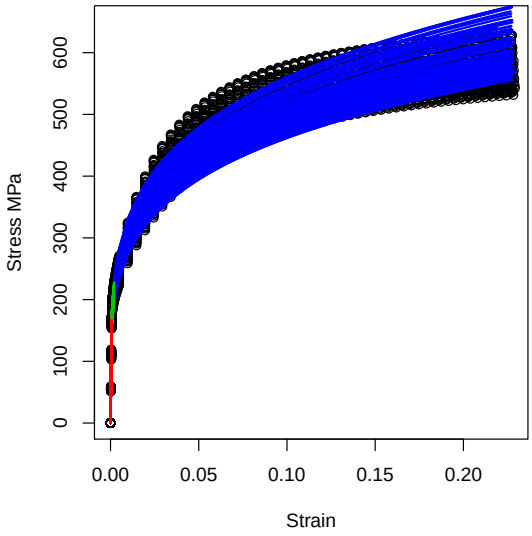


Figure 6.6: Plot of the fitted segmented function for the 70 different stress–strain curves. Different colours indicating the three different segments in Eq. (6.4.2)

λ_1^c and the texture seem to have an influence on the parameters of the model. Looking at the parameter relative to the linear part of the function (Figure 6.9), λ_1^c has a positive effect on the parameter E. Moreover, it seems to be the same for any texture, that instead acts just on the intercept of the relationship. Regarding the relation with the other model parameters, the texture seems to be less influent for n_1 (Figure 6.9 (b)), instead it plays a role for n_2 (Figure 6.9 (c)). For assessing the reasonability of these qualitative comments, 3 different models are fitted. Given that the effect of λ_1^c seems to be the same for each texture, linear mixed models with random intercepts are used [157].

Linear Mixed Model Linear Mixed Model (LMM) is a class of model used especially when the data present a clustered structure. Let $y_i = [y_{i1}, \dots, y_{in_i}]$ denote the vector of responses in the $i-$th cluster, $i = 1, \dots k$; X_i denote the matrix of explanatory variables for which fixed effect are assumed and β_i be the corresponding vector of fixed parameters; Z_i denote the matrix of explanatory variables for which random effect are assumed and α_i be the corresponding vector of random parameters. We consider a linear mixed model that assumes heterogeneity of the intercepts only. The model assumptions are:

- $y_i|(X_i, \mathbf{1}, \alpha_{0i}) \sim N_{n_i}(X_i\beta, \mathbf{1}\alpha_{0i}, \sigma^2 I_{n_i})$

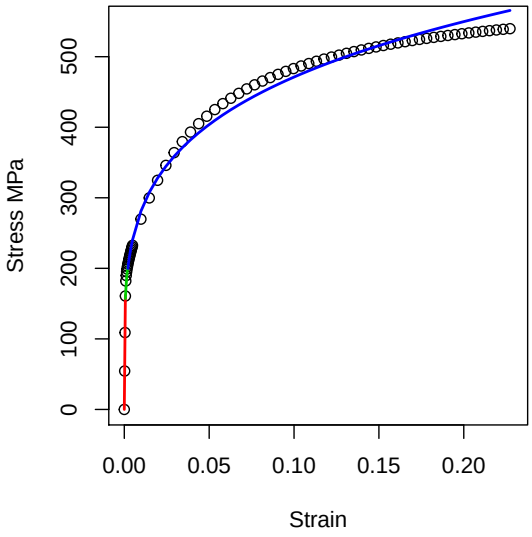
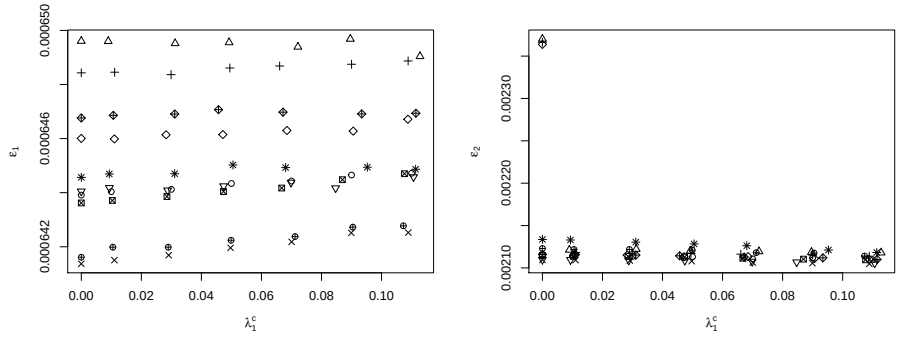
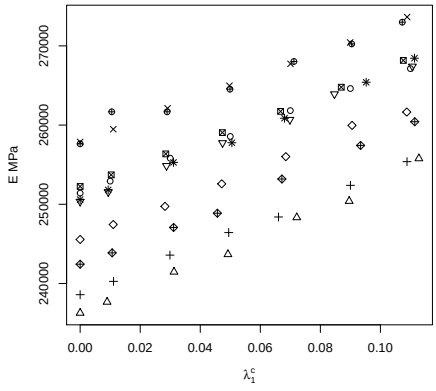


Figure 6.7: Comparison between the observed stress—strain values (black dots) and the estimated piecewise function for one of the 70 stress–strain curve.

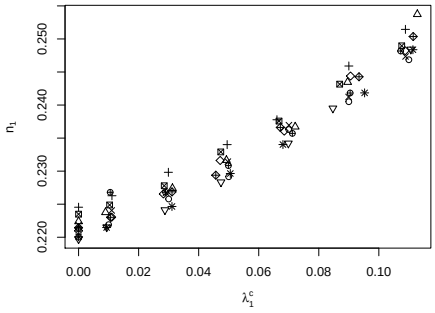


(a) (b)

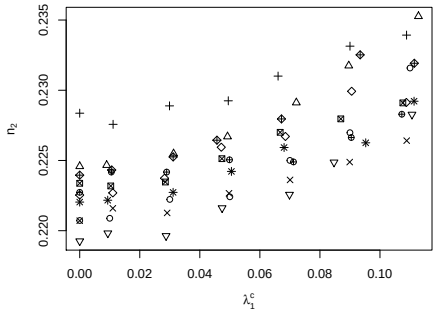
Figure 6.8: Plot of the estimated change points, ϵ_1 (a) and ϵ_2 (b), and the observed volume fraction of carbides for the 70 different microstructures (different symbols indicating different textures).



(a)



(b)



(c)

Figure 6.9: Plot of the estimated model parameters and the observed volume fraction of carbides for the 70 different microstructures (different symbols indicating different textures).

- $\alpha_{0i} \sim N(0, \sigma_\alpha^2)$,

where α_{0i} represents the vector of random intercepts. The model formula is:

$$\mu_i = \beta_0 + \alpha_{0i} + \beta_1 x_i,$$

with μ_i indicating the expected response. The three different models with responses given by the parameters values E, n_1 and n_2 and explanatory variable given by the observed volume fraction of carbides are:

- $E_i = 248286.1 + \alpha_{0j} + 151893.5\,\lambda_{1i}^c$, $\alpha_{0i} \sim N(0, 7136.176)$, $i = 1,\ldots,70$, $j = 1,\ldots,10$;
- $n_{1i} = 0.220 + \alpha_{0j} + 0.248\,\lambda_{1i}^c$, $\alpha_{0i} \sim N(0, 0.001)$, $i = 1,\ldots,70$, $j = 1,\ldots,10$;

- $n_{2i} = 0.222 + \alpha_{0j} + 0.069\,\lambda_{1i}^{c}$, $\alpha_{0i} \sim N(0, 0.002)$, $i = 1, \ldots, 70$, $j = 1, \ldots, 10$.

The estimated parameters values and visual results are reported in the Appendix B.
The approach proposed in this Section is an ad hoc easy and intuitive approach, but it presents some drawbacks.
First, the number of change points and the shape of the piecewise function should be known. Second, the speed of iterative algorithm for determining the values of the change points can be improved. Finally, for high strain values the fitting appears to be poor (Figure 6.7). For overcoming these problems, a more flexible approach based on Functional Data Analysis is proposed in the next Section 6.5.

6.5. FUNCTIONAL DATA ANALYSIS

In this Section the influence of the carbides volume fraction, λ_1^c, on the shape of the resulting stress-strain diagrams (Figure 6.3) is described in a functional context. As already mentioned in Section 6.3 an easy and univocally accepted expression that describes the full range stress–strain curve for metals does not exist. The influencfactors influencing the resulting stress–strain diagram. Treating the stress–strain data obtained from our digital experiment as functional data, we aim to find an underlying function that can describe the general shape of the curve for stainless steel and explain its variability in terms of carbide intensity. The most usual way to represent functional data consists of assuming an expansion of each sample curve in terms of a basis of functions [2]. The basis coefficients are estimated using smoothing, interpolation or as in this Section using Functional Principal Component Analysis (FPCA).
First, we briefly introduce Functional Principal Component Analysis for characterising the functional variation observed in the data. The approach followed in this Chapter is not the conventional approach of centring the functions around the observed empirical mean; the function are centred to the mean stress–strain curve one would observed in microstructures without carbides precipitates. Then, as in the previous Section, a linear mixed model with random intercept is used for relating the Functional Principal Component Scores to the carbides intensity and the texture.

FUNCTIONAL PRINCIPAL COMPONENT ANALYSIS

Principal Component analysis and its functional extension have been successfully applied in reduction of data complexity and interpretation of the underlying variability sources [115]. The idea is that a function $X_i(t)$ can be expressed in terms of the following expansion:

$$X_i(t) = \mu(t) + \sum_{k=1}^{\infty} A_{ik}\phi_k(t), \tag{6.5.1}$$

or by linear approximation

$$X_{iK}(t) \approx \mu(t) + \sum_{k=1}^{K} A_{ik}\phi_k(t), \tag{6.5.2}$$

where $\mu(t)$ is the functional mean, $\phi_k(t)$ are the orthonormal eigenfunctions and $A_{ik} = \int (X_i(t) - \mu(t))\phi_k(t)\mathrm{d}t$ are called the Functional Principal Component Scores. FPCA attempts to find the dominant modes of variation around an overall trend function [163].

In our case, we assume that the overall trend is given by the stress–strain curve for the microstructure without carbides and that the variation from the baseline function can be explained by the increasing carbide volume fractions and the different texture. A modified FPCA is proposed in this context. The difference with the classical approach is in the centring of the functions. In fact, the functions are not centred on their mean function but on the expected stress–strain curve function one would observe for a metal microstructure without carbides. The modified principal component decomposition is:

$$X_{iK}(t) \approx \mu_0(t) + \sum_{k=1}^{K} A_{ik}\phi_k(t), \tag{6.5.3}$$

and

$$A_{ik} = \int (X_i(t) - \mu_0(t))\phi_k(t)\mathrm{d}t \tag{6.5.4}$$

are the modified functional principal components scores. The scores of individual curves on the leading eigenfunctions can be used for description, clustering, classification and prediction [133]. Therefore, in this study the aim is to find an expression for them in terms of the known sources of variations, namely the different texture and the different carbides volume fractions. In some studies, FPCA is used as a method for finding a smooth representation of the data, in others instead the data are smoothed first, and then an unsmoothed functional PCA is carried out. [78]. In the next Section we show an application of the second method.

APPLICATION

The first step for the modified FPCA approach is defining the mean stress–strain curve for microstructures without carbides. Using the stress–strain values obtained for the 10 different microstructures corresponding to the 10 different textures, the expected stress–strain curve for the microstructure without carbides is defined as:

$$\hat{\sigma}_0(\epsilon) = \frac{1}{10}\sum_{j=1}^{10} \sigma_{j0}, \tag{6.5.5}$$

where σ_{j0i} is the stress–strain curve corresponding to $j-$th texture. In Figure 6.10 the 10 different stress–strain curve corresponding to the microstructures without carbides and the expected stress–strain curve (red line) are shown. Secondly the original stress–strain data are centred to the expected stress-strain curve for microstructure without carbides (Figure 6.11). Then we can perform, the modified FPCA. In Figure 6.12 the first two eigenfunctions are plotted. Looking at the behaviour of the first eigenfunction ϕ_1, for low strain levels corresponding to the elastic part of the curve the variance among the curves is low; around the yield point it reaches is maximum and then it stabilises. The interpretation of the second eigenfunction ϕ_2, is instead less intuitive. The plot of the two FPCA scores, A_1 and A_2, shows that the variable are uncorrelated as imposed in the classical FPCA. Moreover, it is possible to interpret A_1 as the effect of the different carbide intensity and A_2 as the effect of the different random textures (Figure 6.13). However, A_1 seems to gather also part of the texture effect (Figure 6.14) and given that it is the one associated with the highest variance, the analysis is reduced to just this component. For

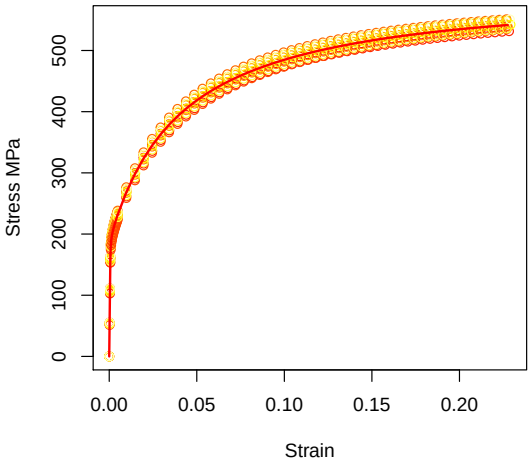


Figure 6.10: Mean stress–strain curve for microstructure without carbides (red line). Different colours indicating different textures.

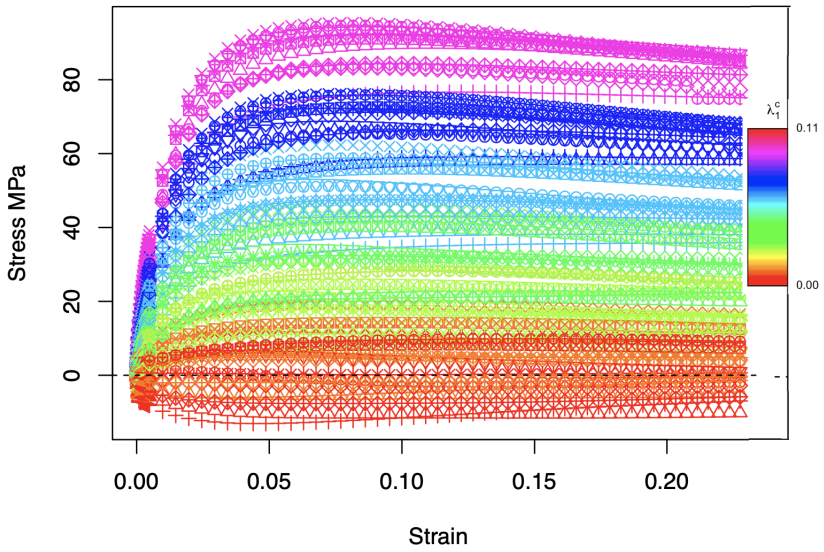


Figure 6.11: Stress–strain centred to the expected stress–strain for microstructure without carbides. Different colours indicating different values of the intensity parameter of the carbides, different symbols indicating different textures.

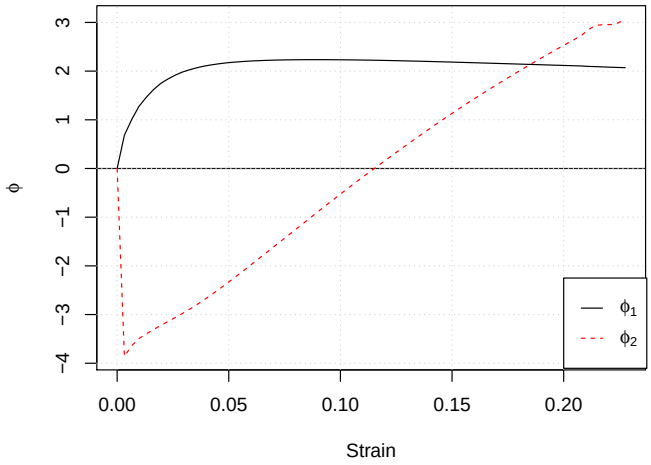


Figure 6.12: First two eigenfunctions obtained with the modified FPCA performed on the 70 stress–strain curves.

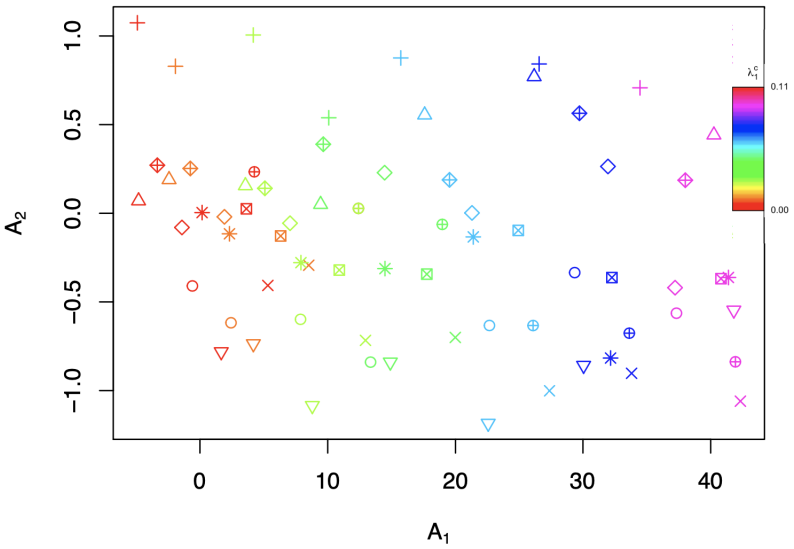


Figure 6.13: Plot of the two FPCA scores obtained for the 70 stress–strain curves. Different colours indicating different values of the intensity parameter of the carbides, different symbols indicating different textures.

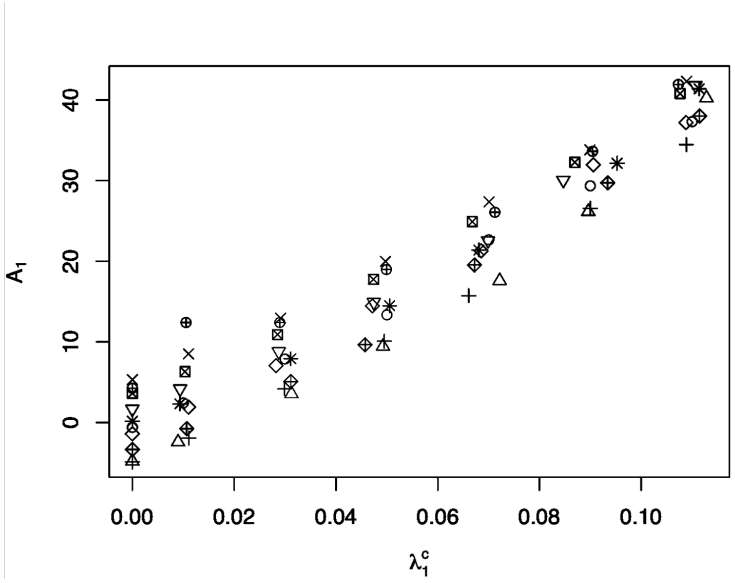


Figure 6.14: Plot of the FPCA scores correspondent to first functional principal component ϕ_1 and the observed values of carbide intensity λ_1^c for the 70 stress–strain curves.Different colours indicating different values of the intensity parameter of the carbides, different symbols indicating different textures.

giving a physical meaning to this decomposition a linear mixed model is used to relate A_1 to the texture and carbides volume fraction 6.14. The model considered is:

$$A_{1i} = -1.351 + \alpha_{0j} + 355.793\,\lambda_{1i}^c,\ \ \alpha_{0j} \sim N(0, 3.320),\ i = 1,\ldots,70,\ j = 1,\ldots,10. \quad (6.5.6)$$

In Table 6.2 the estimated value for α_j and β are reported. Figure 6.15 shows that a linear

Table 6.2: Estimated values of the parameters of the linear mixed model

(a) Texture		(b) λ_1^c
texture	$\beta_0 + \alpha_{0j}$	β
1	−2.204	355.779
2	−5.498	
3	−5.864	
4	3.043	
5	−1.914	
6	−0.170	
7	1.715	
8	−1.464	
9	−4.163	
10	2.983	

mixed model with random intercepts shows a good fitting. Combining Eq. 6.5.3 to Eq.

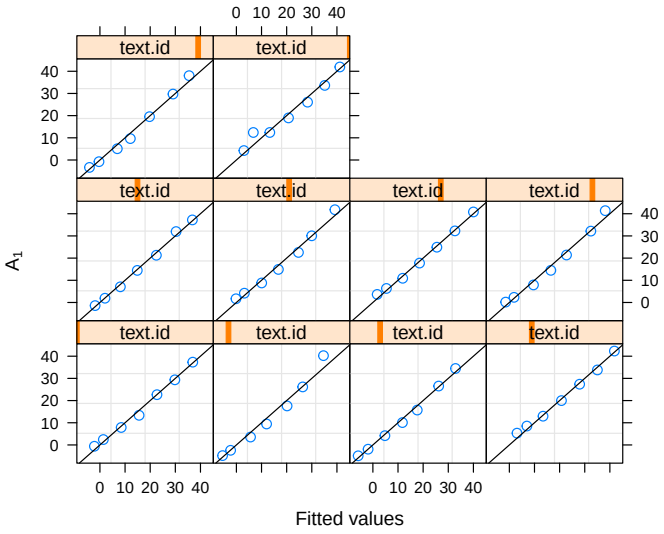


Figure 6.15: Observed first principal component scores, A_1, versus fitted values of linear mixed model (Eq. 6.5.6)

6.5.6, the final model for a generic stress–strain curve is then:

$$\hat{\sigma}_i(\epsilon) = \hat{\sigma}_0(\epsilon) + [-1.351 + \alpha_{0j} + 355.793\,\lambda_{1i}^c]\phi_1(\epsilon,) \;\; \alpha_{0j} \sim N(0, 3.320), \tag{6.5.7}$$

The main graphical model result is shown Figure 6.16. From the comparison for a small subset of the curves shown in Figure 6.17, the model 6.5.7 seems to be adequate. However, around the yield strength point for the curves with a higher value of λ_1^c over estimation seems to occur. In Figures 6.18-6.19 the effect of the different textures and of the carbides volume fractions is shown. The effect is obtained by multiplying the coefficient of the linear mixed model by the eigenfunction $\phi(\epsilon)$. The effect of the texture can be both positive or negative on the resulting stress–strain curve. However, given that the crystallographic orientation are uniformly at random the increase on the points of interest of the curve such as yield stress is moderate (Figure 6.18). The estimated effect of the carbides volume fraction is in agreement with the experimental findings previously discussed: increasing carbide volume fraction does not play a fundamental role in the elastic part of the curve, but it increases the yield strength up to 80 MPa (Figure 6.19).

6.6. CONCLUSIONS

In this Chapter, the influence of $M_{23}C_6$ carbides on the stress-strain behaviour of annealed AISI420 stainless steel is studied. A virtual experiment is set out. The first step is digitally reproducing the microstructure. Synthetic generation of SSRVEs are obtained combining experimental results coming from real experiments and previous virtual examination on an RVE. They are generated changing just two microstructural parameters:

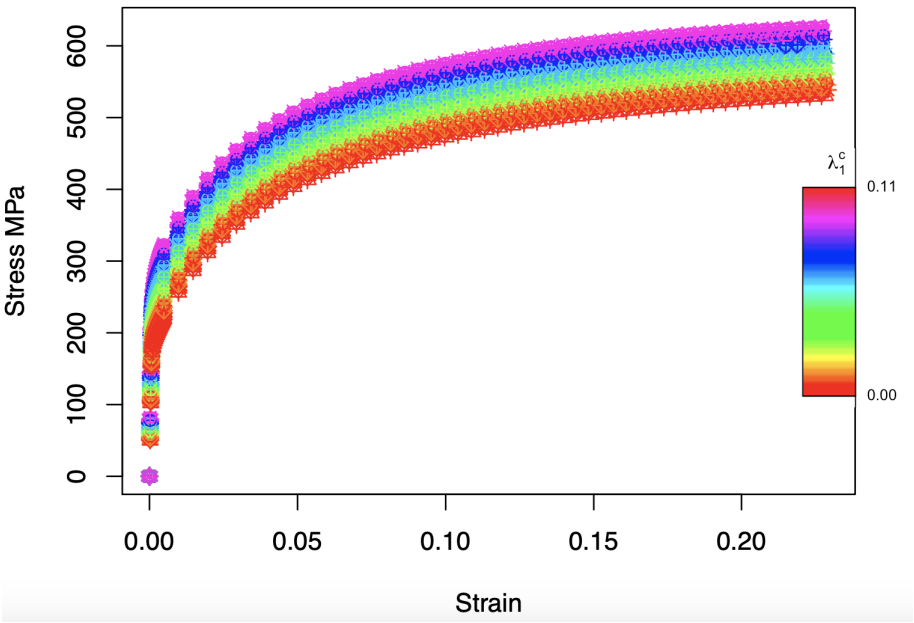


Figure 6.16: Fitted stress–strain functions using model 6.5.7. Different colours indicating different values of the intensity parameter of the carbides, different symbols indicating different textures.

the carbides intensity parameter and the texture. The algorithm used for the geometrical aggregation of multi-phase grains is the Multi-Level Poisson Voronoi tessellation. Then, the virtual tensile test is performed using a software that combine crystal plasticity model and Finite Element methods. The main output of the virtual experiment are the stress–strain curves. After having reviewed the classical mathematical models used for representing the stress–strain behaviour of (stainless) steel, two different new approaches are proposed. The first one is an ad hoc approach that combines the use of segmented function and change points detection tools. It exploits a priori knowledge on the changes in the shape of the function corresponding to the different stages of the tensile test. The second one is based on Functional Principal Component Analysis. A non standard FPCA is performed, centring the function instead of on their functional mean, on the functional stress–strain curve one would observe for a microstructure without carbides. With both approaches the main finding is that the increasing volume fraction of carbides relates to an increment in the strengthening of the material, instead the texture, even if in smaller intensity, influences especially the elastic part of the curve. Further development will include a classification of the textures based on Schmid's factors and a study on the relation between stress–strain curve and position of carbides precipitates.

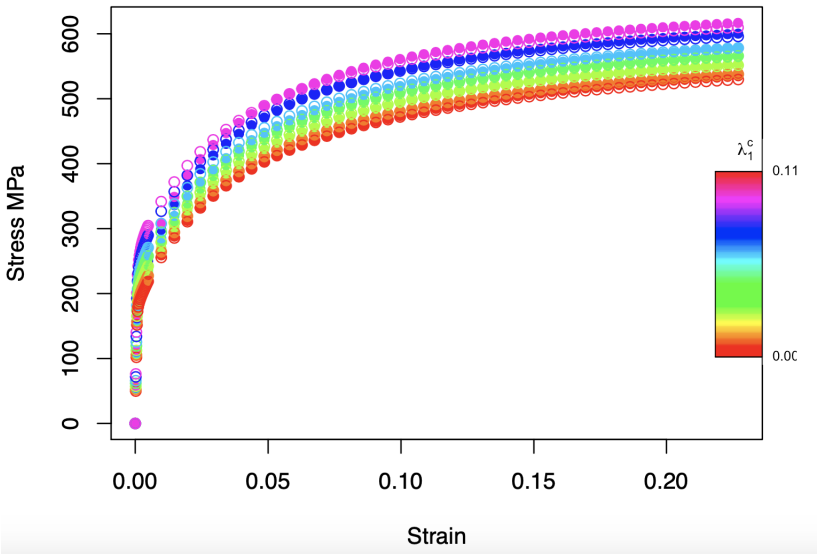


Figure 6.17: Comparison between observed (filled circles) and fitted (empty circles) stress–strain functions. Different colours indicating different values of the intensity parameter of the carbides.

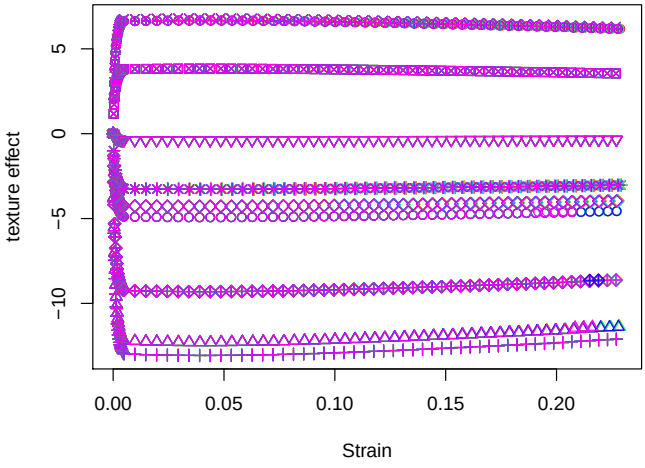


Figure 6.18: Effect of texture in the stress-strain curves.

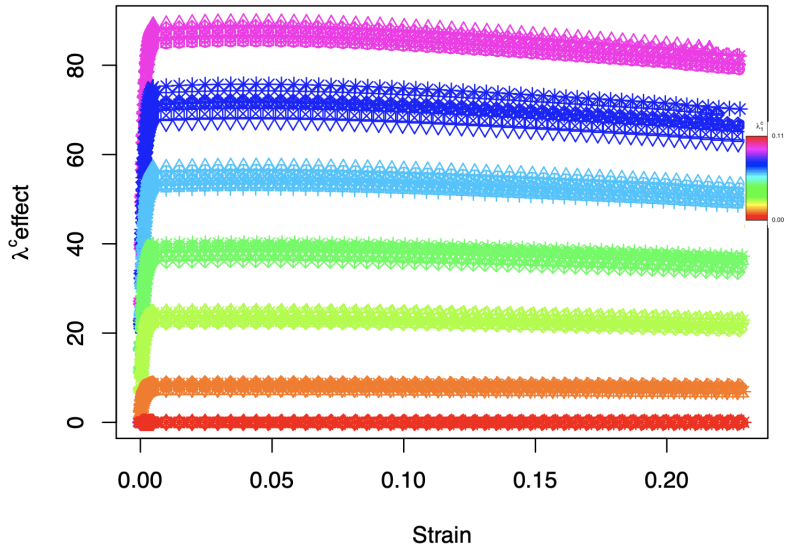


Figure 6.19: Effect of carbides volume fraction in the stress-strain curves. Different symbols indicating different textures.

7

CONCLUSIONS

This thesis aims at the development of physical relations between the intricate metallic microstructures and the mechanical properties of the material. It is part of the output of the project S41.5.14547b "MICtoMEC: Extensive quantification of microstructure features and statistical relations with mechanical behaviour –from statistical relations to physical understanding–" carried out in the framework of the Partnership Program of the Materials innovation institute M2i (www.m2i.nl) and the Technology Foundation TTW (www.stw.nl), which is part of the Netherlands Organization for Scientific Research (www.nwo.nl).
The project was initiated with the aim of studying the complex 3D features of multiphase metallic microstructures of Advanced High-Strength Steels (AHSS) and the mechanical properties of the material.
Materials such as AHSS are of great interest for high-tech applications because of their higher strengths compared to conventional steels.
In the automotive industry this higher strength enables lightweight, fuel-efficient designs, which are also safer than those using conventional materials.
In order to develop new AHSS, the steel industries make use of multi-scale microstructure modelling to predict mechanical properties from the microstructure.
The results of the present project will be directly implemented in microstructure modelling and will be directly available for researchers within the steel industry for developing new materials.
This ambitious project aim is dived into four sub-aims:

1. Statistical analysis of microstructural features;
2. Characterisation of multi-phase microstructures;
3. Microstructural modelling of mechanical behaviour;
4. Stochastic modelling of the relation between microstructural and mechanical properties.

The first two points are faced in the "MICrostructure" part, the last two in the "MEChanical properties" part of this thesis. In the next Sections, after summarising the main results of the thesis, limitations and further developments for the "MIC" and the "MEC" part are discussed.

MICROSTRUCTURE (MIC)

Metallic microstructures are of paramount importance for the properties and performance of the material. One can say that the microstructure forms the DNA of the material. Using a more specific definition, "microstructure" is: a three-dimensional arrangement of grains, phases and defects, with all their chemical and structural variety. For creating new materials with desired properties, a deep characterisation of the microstructure features is needed.
Several problems can be encountered in the study of microstructures. Scale, 2D-3D relation, sampling/sectioning are just examples of the problems one must face.
The arrangement of the grains is one of the microstructure features analysed in this thesis. In particular, the focus is on models used for describing the grain structures.
The use of Voronoi diagrams, referred as the state of the art for modelling the arrangement of the grains in a metal microstructure, is furthered studied and extended. Starting with the most basic case, Poisson-Voronoi diagrams, the main geometrical characteristics of the tessellation cells (grains) are studied. In particular, new simulation results for the grain volume-, grain surface area-, grain number of faces- distributions are obtained. Non parametric and parametric representations of the distributions are given. In the latter case, the best parametric approximation is determined using two criteria: Supremum Distance between cumulative distribution functions and Total Variation Distance. Generalized Gamma results to be the best parametric distribution but not the true underlying distribution. A measure of error is given in case of use.
Poisson-Voronoi diagrams are commonly employed for representing the microstructure of single-phase materials but for more complex microstructures their use is showed to be inadequate. A testing framework based on the comparison of 2D real microstructure section and 2D theoretical sectional diagrams is set. Two new test are proposed: the first one is a Kolmogorov-Smirnov type test based on the distance between cumulative distribution functions of the cells area; the second one exploits tools coming from the emergent area of Topological Data Analysis, in particular persistence landscapes. Two different approaches are proposed according to the use or not of periodic boundary conditions. In both cases, new simulation distributional results are obtained for the reference theoretical diagram: the 2D Sectional Poisson-Voronoi diagram. Quantiles of the distributions of the model tests are given conditionally and unconditionally on the number of observed cells in the section. From the investigation of the tests power, the two new tests result to be more powerful with respect to the one based on the coefficient of variation already proposed in the literature. In the cases in which the use of Poisson-Voronoi is not advisable, e.g for multi-phase microstructures, different alternatives have been proposed in the literature. In this thesis Multi-Level Voronoi diagrams are proposed. Two main advantages of using Multi-Level Voronoi diagrams are discussed: i) the possibility of generating non-convex grains; ii) the ease of defining multi-phase microstructures differentiating properties of the distributions (grain size distribution, precipitation posi-

tion, creation of phases islands) according to the different phases.
However, microstructures are not just about grains. Grain phases, grain orientations, grain boundaries, defects are features of paramount importance in the determination of the mechanical properties of the material. Therefore, these factors have to be studied and included in the so called digital twin microstructure. The concept of digital material representation is sketched in the thesis. The first extension and future development is taking into account all the other important micorstructure characteristics, in order to improve the prediction of the mechanical behaviour of steels.

Mechanical Properties (MEC)

Predictive modelling of mechanical behaviour of steels is possible only if all relevant aspects of the microstructure are taken into account to the required degree of complexity. Properties like hardness, yield strength, toughness, bending strength and hole expansion are desired properties one would like to study in order to get new materials. In this thesis, two different approaches for mechanical properties investigation are proposed. The first one is investigating data from 2D images of material sections. The relation between microstructure features such as different volume fractions or precipitates and the strengthening of the material can be studied for instance looking at the heterogeneous formation of dislocations in areas of the materials in which diverse particles are present. Studying the mechanical behaviour, investigating data coming from 2D images of material sections constitutes a good starting point for understanding the influence of microstructural features on the mechanical response of the material. In this context, a new method for incorporating prior physical knowledge and empirical observation into the statistical modelling of the relation between geometrically necessary dislocations and carbides volume fraction is described. Estimation and testing under order restrictions are faced in an isotonic context. Three different scenarios according to the knowledge of the variance structure are considered. New likelihood ratio tests and two bootstrap approaches (parametric and non parametric) are proposed. However, studying the relation between microstructural features and mechanical properties from 2D images makes impossible controlling all the possible influencing factor and their intrinsic correlation structures.
Therefore, a more advanced way for studying this relation is proposed: a virtual approach. Academia and steel industry are developing tools that simulate the mechanical behaviour of metallic materials in two steps: (i) the creation of virtual microstructures; (ii) the simulation of the mechanical behaviour of these microstructures. The simulation of the mechanical behaviour is based on Finite Element Modelling and Crystal Plasticity Modelling. Such simulations allow probing the influence of several microstructural features like the grain geometrical arrangement, grain-size distribution and phase fractions. Performing simulations on the mechanical behaviour of well-defined virtual microstructures allows to develop the physical basis of the relation between microstructural features and the mechanical properties. Virtual microstructures are designed in such a way that have the same microstructural features as selected real materials, but also that they obey to the same physical and phenomenological laws. The computer modelling allows to apply variations in the microstructure at a level of control that is not achievable in real experiments. This yields a strengthened insight into the relation between microstruc-

tural features, physical behaviour and mechanical properties. The valuable information and insight that one can achieve with simulation-base methods pay the cost of more rigorous and detailed experimental validation.
In this thesis, the effect of carbides on material strengthening is studied via virtual tensile tests. Two new approaches based on Change-point detection, functional data analysis are developed and applied for obtaining new insights in the investigated relation.
The main limitations of the approaches proposed in this thesis is that they consider the relation of one microstructure features on one specific mechanical property. The plan is to extend this study, including a multivariate approach that will take into account the interrelation among the explanatory variables on multiple response variables corresponding to different mechanical properties.

A

APPENDIX

CHAPTER 4

ALGORITHM 2.1

0. INITIALIZATION Let $\boldsymbol{\mu}^{(0)} = \bar{\boldsymbol{y}} = (\bar{y}_1, \dots \bar{y}_k)'$ and $\boldsymbol{w} = (w_1, \dots w_k)'$, $w_i = \frac{n_i}{c_i}$

1. QUESTION Is $\bar{y}_1 \leq \bar{y}_2 \leq \cdots \leq \bar{y}_k$?

1.1 YES $\boldsymbol{\mu}^* = \bar{\boldsymbol{y}}$ is the solution

1.2 NO $\bar{y}_i > \bar{y}_{i+1}$

Replace $\bar{y}_i$ and $\bar{y}_{i+1}$ by

$$m_{i,i+1} = \frac{w_i \bar{y}_i + w_{i+1} \bar{y}_{i+1}}{w_i + w_{i+1}} \tag{A.0.1}$$

Repeat until QUESTION 1 is satisfied.

ALGORITHM 2.2

Two steps Iterative procedure

0. INITIALIZATION Let $\boldsymbol{\mu}^{(0)} = \bar{\boldsymbol{y}} = (\bar{y}_1, \dots \bar{y}_k)'$, $\boldsymbol{\sigma}^{2(0)} = \bar{\boldsymbol{\sigma}}^2 = (\bar{\sigma}_1^2, \dots \bar{\sigma}_k^2)'$, $\bar{\sigma}_i^2 = \frac{\sum_j (y_{ij} - \bar{y}_i)^2}{n_i}$ and $\boldsymbol{w}^{(0)} = (w_1^{(0)}, \dots w_k^{(0)})'$, $w_i^{(0)} = \frac{n_i}{\sigma^{2(0)}}$

1. QUESTION Is $\bar{y}_1 \leq \bar{y}_2 \leq \cdots \leq \bar{y}_k$?

1.1 YES $\boldsymbol{\mu}^* = \boldsymbol{\mu}^{(0)} = \bar{\boldsymbol{y}}$ and $\boldsymbol{\sigma}^2 = \boldsymbol{\sigma}^{2(0)} = \bar{\boldsymbol{\sigma}}^2$ are the solutions

1.2 NO Use Step 1.2 Algorithm 2.1 to compute $\boldsymbol{\mu}^{(l)}$ with weights $\boldsymbol{w}^{(l-1)}$

1.2.1 Compute $\boldsymbol{\sigma}^{2(l)} = \boldsymbol{s}^{2(l)}$, $s_i^{2(l)} = \frac{\sum_j (y_{ij} - \mu_i^{(l)})^2}{n_i}$ and $\boldsymbol{w}^{(l)} = (w_1^{(l)}, \dots w_k^{(l)})'$, $w_i^{(l)} = \frac{n_i}{\sigma^{2(l)}}$

1.2.2 Go back to QUESTION 1 using $\boldsymbol{w}^{(l)}$.

Repeat until

$$\max_{1 \leq i \leq k} |\mu_i^{*(l-1)} - \mu_i^{*(l)}| \leq 10^{-m}$$

Alternating Iterative Method

0. INITIALIZATION Let $\boldsymbol{\nu^{(0)}} = (1/\bar{\sigma}_1^2, \dots 1/\bar{\sigma}_k^2)'$, $\bar{\sigma}_i^2 = \frac{\sum_j (y_{ij} - \bar{y}_i)^2}{n_i}$

1. FIND $\boldsymbol{\mu^{(l)}}$ the isotonic regression on D_a using weights $\boldsymbol{w^{(l-1)}} = (w_1^{(l-1)}, \dots w_k^{(l-1)})'$, $w_i^{(l-1)} = n_i \nu^{(l-1)}$;

2. FIND $\boldsymbol{\nu^{(l)}}$ maximizing the profile likelihood $L(y; \boldsymbol{\mu^{(l)}}; \boldsymbol{\nu})$ on V_0,
$V_0 = \{\nu \in \mathbb{R}^k : 0 \leq 1/\max_i(\min_{\min(\bar{y}) \leq \theta \leq \max(\bar{y})} s_i^2(\theta)) \leq \nu_1 \leq \dots \leq \nu_k \leq 1/\min_i(\min_{\min(\bar{y}) \leq \theta \leq \max(\bar{y})} s_i^2(\theta))\}$.
Repeat (1)-(2) until

$$|L(y; \boldsymbol{\mu^{(l-1)}}, \boldsymbol{\nu^{(l-1)}}) - L(y; \boldsymbol{\mu^{(l)}}, \boldsymbol{\nu^{(l)}})| \leq 10^{-m}$$

ALGORITHM 2.3

Two steps Iterative procedure

0. INITIALIZATION Let $\boldsymbol{\mu^{(0)}} = \bar{\boldsymbol{y}} = (\bar{y}_1, \dots \bar{y}_k)'$, $\boldsymbol{\sigma^{2(0)}} = \bar{\boldsymbol{\sigma}}^{\boldsymbol{2}} = (\bar{\sigma}_1^2, \dots \bar{\sigma}_k^2)'$, $\bar{\sigma}_i^2 = \frac{\sum_j (y_{ij} - \bar{y}_i)^2}{n_i}$ and and $\boldsymbol{w^{(0)}} = (w_1^{(0)}, \dots w_k^{(0)})'$, $w_i^{(0)} = \frac{n_i}{\sigma^{2(0)}}$.

1. QUESTION Is $\bar{y}_1 \leq \bar{y}_2 \leq \dots \leq \bar{y}_k$?

1.1 YES $\boldsymbol{\mu}^* = \boldsymbol{\mu^{(0)}} = \bar{\boldsymbol{y}}$ go to QUESTION 2.

1.2 NO Use Step 1.2 Algorithm 2.1 to compute $\boldsymbol{\mu^{(l)}}$ with weights $\boldsymbol{w^{(l-1)}}$

1.2.1 Compute $\boldsymbol{\sigma^{2(l)}} = \boldsymbol{s^{2(l)}}$, $s_i^{2(l)} = \frac{\sum_j (y_{ij} - \mu_i^{(l)})^2}{n_i}$ and $\boldsymbol{w^{(l)}} = (w_1^{(l)}, \dots w_k^{(l)})'$, $w_i^{(l)} = \frac{n_i}{\sigma^{2(l)}}$

2. QUESTION Is $\sigma_1^{2(l)} \geq \sigma_2^{2(l)} \geq \dots \geq \sigma_k^{2(l)}$?

2.1 YES $\boldsymbol{\mu}^* = \boldsymbol{\mu^{(l)}}$ and $\boldsymbol{\sigma^{2*}} = \boldsymbol{\sigma^{2(l)}}$ are the solutions.

2.2. NO $\sigma_i^{2(l)} < \sigma_j^{2(l)}$

Replace $\sigma_i^{2(l)}$ and $\sigma_{i+1}^{2(l)}$ by

$$\sigma_i^{2(l+1)} = \sigma_{i+1}^{2(l+1)} = \bar{s}_{i,i+1} = \frac{n_i \sigma_i^{2(l)} + n_{i+1} \sigma_{i+1}^{2(l)}}{n_i + n_{i+1}} \tag{A.0.2}$$

Repeat until QUESTION 2 is satisfied.

2.2.1 Go back to QUESTION 1 using $\boldsymbol{w^{(l)}}$.
Repeat until

$$\max_{1 \leq i \leq k} |\mu_i^{*(l-1)} - \mu_i^{*(l)}| \leq 10^{-m} \text{ and } \max_{1 \leq i \leq k} |\sigma_i^{2*(l-1)} - \sigma_i^{2*(l)}| \leq 10^{-m}$$

Alternating Iterative Method

0. INITIALIZATION Let $\boldsymbol{\nu}^{(\mathbf{0})} = (1/\bar{\sigma}_1^2, \dots 1/\bar{\sigma}_k^2)'$, $\bar{\sigma}_i^2 = \frac{\sum_j (y_{ij} - \bar{y}_i)^2}{n_i}$

1. FIND $\boldsymbol{\mu}^{(\boldsymbol{l})}$ use Step 1 AlM Algorithm 2.2;

2. FIND $\boldsymbol{\nu}^{(\boldsymbol{l})}$ the isotonic regression on V_0, $V_0 = \{\nu \in \mathbb{R}^k : 0 \leq 1/\max_i(\min_{\min(\bar{y}) \leq \theta \leq \max(\bar{y})} s_i^2(\theta)) \leq \nu_1 \leq \cdots \leq \nu_k \leq 1/\min_i(\min_{\min(\bar{y}) \leq \theta \leq \max(\bar{y})} s_i^2(\theta))\}$ with weights $\boldsymbol{N} = (n_1, \dots, n_k)'$
Repeat (1)-(2) until

$$|L(y; \boldsymbol{\mu}^{(\boldsymbol{l-1})}, \boldsymbol{\nu}^{(\boldsymbol{l-1})}) - L(y; \boldsymbol{\mu}^{(\boldsymbol{l})}, \boldsymbol{\nu}^{(\boldsymbol{l})})| \leq 10^{-m}$$

B

APPENDIX

CHAPTER 5

Table B.1: Estimated values of the parameters of the linear mixed model

(a) E

$\beta_0 + \alpha_{0j}$	β_1
251083.3	151893.5
236909.1	
238729.9	
257385.0	
245591.7	
250462.0	
251891.7	
250660.8	
242674.7	
257472.5	

(b) n_1

$\beta_0 + \alpha_{0j}$	β_1
0.220	0.248
0.223	
0.224	
0.222	
0.222	
0.220	
0.223	
0.220	
0.222	
0.222	

(c) n_2

$\beta_0 + \alpha_{0j}$	β_1
0.221	0.069
0.225	
0.227	
0.220	
0.223	
0.220	
0.223	
0.222	
0.224	
0.222	

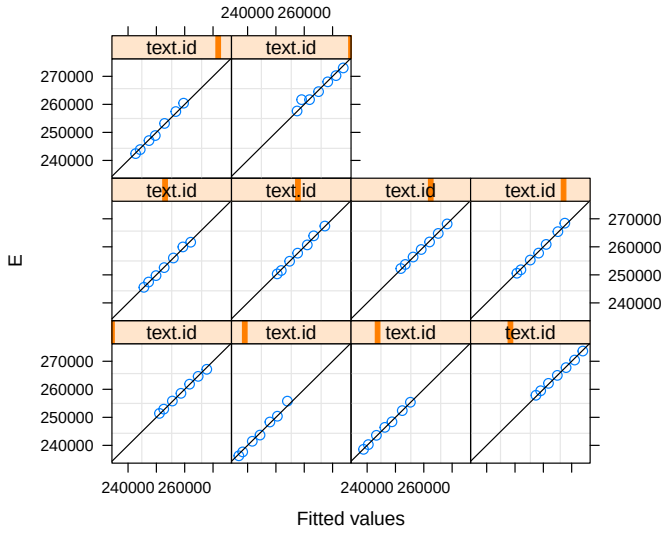


Figure B.1: Estimated E parameter of the first segment of function (6.4.1) versus fitted values of a linear mixed model with random intercepts for the different textures and explanatory variable given by the observed carbide volume fraction

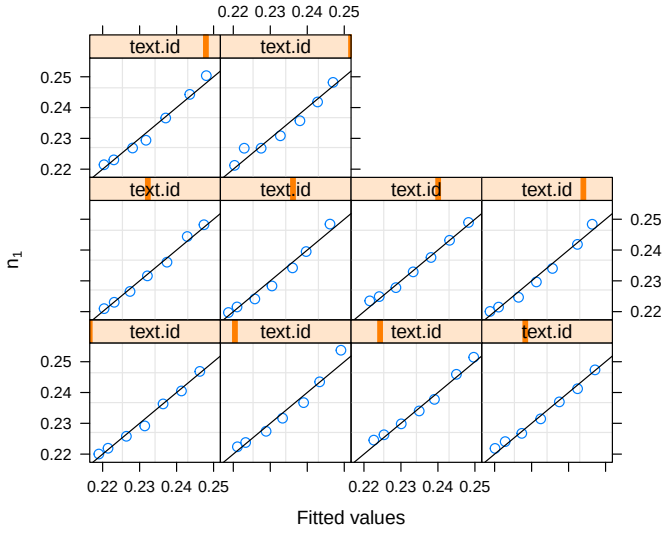


Figure B.2: Estimated n_1 parameter parameter of the second segment of function (6.4.1) versus fitted values of a linear mixed model with random intercepts for the different textures and explanatory variable given by the observed carbide volume fraction

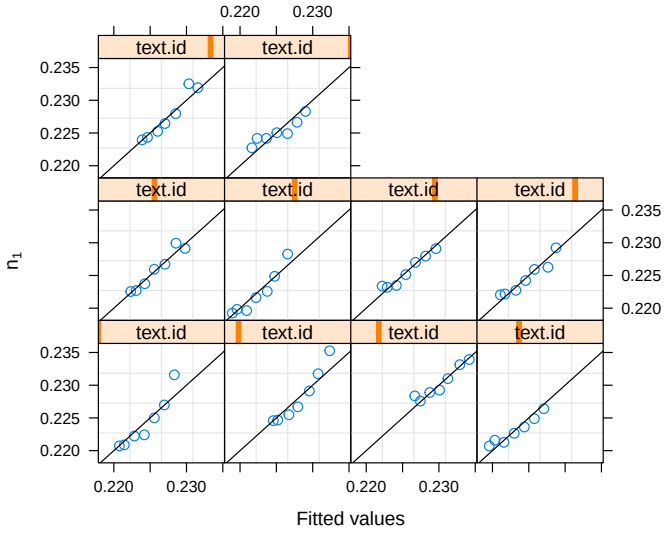


Figure B.3: Estimated n_2 parameter of the third segment of function (6.4.1) versus fitted values of a linear mixed model with random intercepts for the different textures and explanatory variable given by the observed carbide volume fraction

BIBLIOGRAPHY

[1] K. Abdella. “Inversion of a full-range stress–strain relation for stainless steel alloys”. In: *International Journal of Non-Linear Mechanics* 41.3 (2006), pp. 456–463.

[2] A. M. Aguilera and M.C. Aguilera-Morillo. “Comparative study of different B-spline approaches for functional data”. In: *Mathematical and Computer Modelling* 58.7-8 (2013), pp. 1568–1579.

[3] F. Aurenhammer. “Voronoi diagrams—a survey of a fundamental geometric data structure”. In: *ACM Computing Surveys (CSUR)* 23.3 (1991), pp. 345–405.

[4] M. Ayer et al. “An empirical distribution function for sampling with incomplete information”. In: *The annals of mathematical statistics* (1955), pp. 641–647.

[5] P. Bala, H.r Tsyrulin K.and Jaksch, and M. Stepien. “3D reconstruction and characterization of carbides in Ni-based high carbon alloy in a FIB-SEM system”. In: *International Journal of Materials Research* 106.7 (2015), pp. 764–770.

[6] D. Balzani, D. Brands, and J. Schröder. “Construction of statistically similar representative volume elements”. In: *Plasticity and Beyond*. Springer, 2014, pp. 355–412.

[7] D. Balzani et al. “Construction of two-and three-dimensional statistically similar RVEs for coupled micro-macro simulations”. In: *Computational Mechanics* 54.5 (2014), pp. 1269–1284.

[8] S. Bargmann et al. “Generation of 3D representative volume elements for heterogeneous materials: A review”. In: *Progress in Materials Science* 96 (2018), pp. 322–384.

[9] R. E. Barlow and H. D. Brunk. “The isotonic regression problem and its dual”. In: *Journal of the American Statistical Association* 67.337 (1972), pp. 140–147.

[10] S. Barragán et al. “isocir: An R package for constrained inference using isotonic regression for circular data, with an application to cell biology”. In: *Journal of Statistical Software* 54.4 (2013).

[11] A. Bazyari. “Bootstrap approach to test the homogeneity of order restricted mean vectors when the covariance matrices are unknown”. In: *Communications in Statistics-Simulation and Computation* 46.9 (2017), pp. 7194–7209.

[12] Y. Bergström and Y. Granbom. “A dislocation model for the stress-strain behavior of dual phase steels”. In: (2008).

[13] H. Bhadeshia and R. Honeycombe. *Steels: microstructure and properties*. Butterworth-Heinemann, 2017.

[14] M.W. Bird et al. “Local dislocation creep accommodation of a zirconium diboride silicon carbide composite”. In: *Acta Materialia* 84 (2015), pp. 359–367.

[15] C. A.N. Biscio and J. Møller. “The accumulated persistence function, a new useful functional summary statistic for topological data analysis, with a view to brain artery trees and spatial point process applications”. In: *Journal of Computational and Graphical Statistics* 28.3 (2019), pp. 671–681.

[16] K. A. Brakke. “Statistics of random plane Voronoi tessellations”. In: *Preprint, Dept. Math. Sciences, Susquehanna Univ* (1987).

[17] K.A. Brakke. “Plane Voronoi tessellation second order statistics”. In: *American Mathematical Society* 1 (1986), pp. 235–236.

[18] D. Brandon and W. D. Kaplan. *Microstructural characterization of materials*. John Wiley & Sons, 2013.

[19] D. Brands et al. “Computational modeling of dual-phase steels based on representative three-dimensional microstructures obtained from EBSD data”. In: *Archive of Applied Mechanics* 86.3 (2016), pp. 575–598.

[20] P. Bubenik. “Statistical topological data analysis using persistence landscapes”. In: *The Journal of Machine Learning Research* 16.1 (2015), pp. 77–102.

[21] M. Calcagnotto et al. “Orientation gradients and geometrically necessary dislocations in ultrafine grained dual-phase steels studied by 2D and 3D EBSD”. In: *Materials Science and Engineering: A* 527.10-11 (2010), pp. 2738–2746.

[22] P. Calka. “An explicit expression for the distribution of the number of sides of the typical Poisson-Voronoi cell”. In: *Advances in Applied Probability* (2003), pp. 863–870.

[23] P. Calka et al. “Precise formulae for the distributions of the principal geometric characteristics of the typical cells of a two-dimensional Poisson-Voronoi tessellation and a Poisson line process”. In: *Advances in Applied Probability* 35.3 (2003), pp. 551–562.

[24] F. Chazal et al. “Stochastic convergence of persistence landscapes and silhouettes”. In: *Proceedings of the thirtieth annual symposium on Computational geometry*. 2014, pp. 474–483.

[25] S.N. Chiu, R. Van de Weygaert, and D. Stoyan. “The sectional Poisson Voronoi tessellation is not a Voronoi tessellation”. In: *Advances in applied probability* (1996), pp. 356–376.

[26] L.Y. Dai, G.Y. Niu, and M.Z. Ma. “Microstructure Evolution and Nanotribological Properties of Different Heat-Treated AISI 420 Stainless Steels after Proton Irradiation”. In: *Materials* 12.11 (2019), p. 1736.

[27] J. R. Davis. *Tensile testing*. ASM international, 2004.

[28] E. G. Dere. “Microstructure Control of Fire-resistant, Low-alloy Steel; An in-situ 3D X-ray Diffraction and A Small-angle X-ray Scattering Study”. In: (2013).

[29] G. E. Dieter. *Mechanical metallurgy*. 1976.

[30] S.P. Donegan et al. “Extreme value analysis of tail departure from log-normality in experimental and simulated grain size distributions”. In: *Acta Materialia* 61.15 (2013), pp. 5595–5604.

[31] M. Durand-Charre. *Microstructure of steels and cast irons*. Springer Science & Business Media, 2004.

[32] R. Dykstra, T. Robertson, and F. T. Wright. *Order Restricted Statistical Inference*. New York, Wiley, 1988.

[33] H. Edelsbrunner and J. Harer. *Computational topology: an introduction*. American Mathematical Soc., 2010.

[34] Herbert Edelsbrunner, Anton Nikitenko, and Matthias Reitzner. "Expected sizes of Poisson–Delaunay mosaics and their discrete Morse functions". In: *Advances in Applied Probability* 49.3 (2017), pp. 745–767.

[35] P. Eisenlohr and F. Roters. "Selecting a set of discrete orientations for accurate texture reconstruction". In: *Computational Materials Science* 42.4 (2008), pp. 670–678.

[36] M. Escabias, A.M. Aguilera, and M.J. Valderrama. "Modeling environmental data by functional principal component logistic regression". In: *Environmetrics: The official journal of the International Environmetrics Society* 16.1 (2005), pp. 95–107.

[37] S. Falco et al. "Generation of 3D polycrystalline microstructures with a conditioned Laguerre-Voronoi tessellation technique". In: *Computational Materials Science* 136 (2017), pp. 20–28.

[38] P. Fearnhead, R. Maidstone, and A. Letchford. "Detecting Changes in Slope With an L 0 Penalty". In: *Journal of Computational and Graphical Statistics* 28.2 (2019), pp. 265–275.

[39] J.S. Ferenc and Z. Néda. "On the size distribution of Poisson Voronoi cells". In: *Physica A: Statistical Mechanics and its Applications* 385.2 (2007), pp. 518–526.

[40] M. Ferraro and L. Zaninetti. "On the statistics of area size in two-dimensional thick Voronoi diagrams". In: *Physica A: Statistical Mechanics and its Applications* 391.20 (2012), pp. 4575 –4582. ISSN: 0378-4371. DOI: http://dx.doi.org/10.1016/j.physa.2012.05.029. URL: http://www.sciencedirect.com/science/article/pii/S0378437112004001.

[41] S. Fortune. "A sweepline algorithm for Voronoi diagrams". In: *Algorithmica* 2.1-4 (1987), p. 153.

[42] D. T. Fullwood et al. "Microstructure sensitive design for performance optimization". In: *Progress in Materials Science* 55.6 (2010), pp. 477–562.

[43] E.N. Gilbert. "Random subdivisions of space into crystals". In: *The Annals of mathematical statistics* 33.3 (1962), pp. 958–972.

[44] E. Y. Gökpınar and F. Gökpınar. "A test based on the computational approach for equality of means under the unequal variance assumption". In: *Hacettepe journal of Mathematics and Statistics* 41.4 (2012), pp. 605–613.

[45] F. A. Graybill and R.B. Deal. "Combining unbiased estimators". In: *Biometrics* 15.4 (1959), pp. 543–550.

[46] M. A. Groeber and M. A Jackson. “DREAM. 3D: a digital representation environment for the analysis of microstructure in 3D”. In: *Integrating materials and manufacturing innovation* 3.1 (2014), p. 5.

[47] P. Groeneboom and G. Jongbloed. *Nonparametric estimation under shape constraints*. Vol. 38. Cambridge University Press, 2014.

[48] A. Guntuboyina, B. Sen, et al. “Nonparametric shape-restricted regression”. In: *Statistical Science* 33.4 (2018), pp. 568–594.

[49] U. Hahn and U. Lorz. “On the precision of some stereological estimators for the model parameter of the spatial Poisson-Voronoi tessellation”. In: *Acta Stereologica* (1994).

[50] U. Hahn and U. Lorz. “Stereological model tests for the spatial Poisson-Voronoi tessellation II”. In: *Acta Stereologica* 12 (1993), pp. 131–131.

[51] E.O. Hall. “The deformation and ageing of mild steel: III discussion of results”. In: *Proceedings of the Physical Society. Section B* 64.9 (1951), p. 747.

[52] H. G. Hanson. “Voronoi cell properties from simulated and real random spheres and points”. In: *Journal of Statistical Physics* 30.3 (1983), pp. 591–605. ISSN: 1572-9613. DOI: 10.1007/BF01009678. URL: http://dx.doi.org/10.1007/BF01009678.

[53] A. Hatcher. *Algebraic topology*. 2005.

[54] D. Helm et al. “Microstructure-based description of the deformation of metals: theory and application”. In: *JOM* 63.4 (2011), pp. 26–33.

[55] H. Hermann, H. Wendrock, and D. Stoyan. “Cell-area distributions of planar Voronoi mosaics”. In: *Metallography* 23.3 (1989), pp. 189–200.

[56] S. Hertelé, W. De Waele, and R. Denys. “A generic stress–strain model for metallic materials with two-stage strain hardening behaviour”. In: *International Journal of Non-Linear Mechanics* 46.3 (2011), pp. 519–531.

[57] J. G. Hicks. *Welded joint design*. Industrial Press Inc., 1999.

[58] J. Hidalgo et al. “Influence of $M_{23}C_6$ Carbides on the Heterogeneous Strain Development in Annealed 420 Stainless Steel”. In: *Available at SSRN 3558254* ().

[59] R. Hill. “Elastic properties of reinforced solids: some theoretical principles”. In: *Journal of the Mechanics and Physics of Solids* 11.5 (1963), pp. 357–372.

[60] A.L. Hinde and R.E. Miles. “Monte Carlo estimates of the distributions of the random polygons of the Voronoi tessellation with respect to a Poisson process”. In: *Journal of Statistical Computation and Simulation* 10.3-4 (1980), pp. 205–223.

[61] N. Hiroshi. “Defects in Metals”. In: *Physical Metallurgy*. Elsevier, 2014, pp. 561–637.

[62] J. H. Hollomon et al. “Tensile deformation”. In: *Aime Trans* 12.4 (1945), pp. 1–22.

[63] R. Hooke. *Lectures de potentia restitutiva, or of spring explaining the power of springing bodies*. 6. John Martyn, 1678.

[64] R. Hu et al. “Precipitation behavior of grain boundary M23C6 and its effect on tensile properties of Ni–Cr–W based superalloy”. In: *Materials Science and Engineering: A* 548 (2012), pp. 83–88.

[65] D. Hull and D. J. Bacon. *Introduction to dislocations*. Butterworth-Heinemann, 2001.

[66] A. Inoue, S. Arakawa, and T. Masumoto. “Effect of alloying elements on defect structure and hardness of M23C6 type carbides”. In: *Transactions of the Japan Institute of Metals* 20.10 (1979), pp. 585–592.

[67] M. C. Jones. “Simple boundary correction for kernel density estimation”. In: *Statistics and computing* 3.3 (1993), pp. 135–146.

[68] J. Kadkhodapour et al. “Experimental and numerical study on geometrically necessary dislocations and non-homogeneous mechanical properties of the ferrite phase in dual phase steels”. In: *Acta Materialia* 59.11 (2011), pp. 4387–4394.

[69] A. Keshvari and T. Kuosmanen. “Stochastic non-convex envelopment of data: Applying isotonic regression to frontier estimation”. In: *European Journal of Operational Research* 231.2 (2013), pp. 481–491.

[70] T. Kiang. “Random fragmentation in two and three dimensions”. In: *Zeitschrift fur Astrophysik* 64 (1966), p. 433.

[71] J.F.C. Kingman. *Poisson processes, Encyclopedia of Biostatistics*. 1993.

[72] P.J.J. Kok, W. Spanjer, and H. Vegter. “A microstructure based model for the mechanical behavior of multiphase steels”. In: *Key Engineering Materials*. Vol. 651. Trans Tech Publ. 2015, pp. 975–980.

[73] U. Krawietz R.and Lorz. “Stereological model tests for the spatial Poisson-Voronoi tessellation”. In: *Acta Stereologica* (1991).

[74] S. Kumar and S. K. Kurtz. “Monte-Carlo study of angular and edge length distributions in a three-dimensional Poisson-Voronoi tesselation”. In: *Materials characterization* 34.1 (1995), pp. 15–27.

[75] F. T. Lewis. “The correlation between cell division and the shapes and sizes of prismatic cells in the epidermis of cucumis”. In: *The anatomical record* 38.3 (1928), pp. 341–376.

[76] T. Li, J. Zheng, and Z. Chen. “Description of full-range strain hardening behavior of steels”. In: *SpringerPlus* 5.1 (2016), p. 1316.

[77] W. Li and H. Fu. “Bayesian isotonic regression dose–response model”. In: *Journal of biopharmaceutical statistics* 27.5 (2017), pp. 824–833.

[78] Z.a Lin, L. Wang, and J. Cao. “Interpretable functional principal component analysis”. In: *Biometrics* 72.3 (2016), pp. 846–854.

[79] P.D. Littlewood, T.B. Britton, and A.J. Wilkinson. “Geometrically necessary dislocation density distributions in Ti–6Al–4V deformed in tension”. In: *Acta Materialia* 59.16 (2011), pp. 6489–6500.

[80] Y. Liu et al. “Mechanical properties and electronic structures of M23C6 (M= Fe, Cr, Mn)-type multicomponent carbides”. In: *Journal of Alloys and Compounds* 648 (2015), pp. 874–880.

[81] U. Lorz. “Cell-area distributions of planar sections of spatial Voronoi mosaics”. In: *Materials characterization* 25.3 (1990), pp. 297–309.

[82] U. Lorz. “Distributions of cell characteristics of the spatial Poisson-Voronoi tessellation and plane sections”. In: *Geometrical Problems of Image Processings* 4 (1991), pp. 171–178.

[83] U. Lorz and U. Hahn. *Geometric characteristics of random spatial Voronoi tessellations and planar sections*. Dekan des Fachbereiches Mathematik, 1993.

[84] D.C. Ludwigson. “Modified stress-strain relation for FCC metals and alloys”. In: *Metallurgical Transactions* 2.10 (1971), pp. 2825–2828.

[85] P. Ludwik. *Elemente der technologischen Mechanik*. Springer-Verlag, 2013.

[86] S. Luss R.and Rosset, M. Shahar, et al. “Efficient regularized isotonic regression with application to gene–gene interaction search”. In: *The Annals of Applied Statistics* 6.1 (2012), pp. 253–283.

[87] A. Lyckegaard et al. “On the use of Laguerre tessellations for representations of 3D grain structures”. In: *Advanced Engineering Materials* 13.3 (2011), pp. 165–170.

[88] L. Madej. “Digital/virtual microstructures in application to metals engineering–A review”. In: *Archives of Civil and Mechanical Engineering* 17.4 (2017), pp. 839–854.

[89] K. W. Mahin, K. Hanson, and J.W. Morris Jr. “Comparative analysis of the cellular and Johnson-Mehl microstructures through computer simulation”. In: *Acta Metallurgica* 28.4 (1980), pp. 443–453.

[90] J. Mecke. “Parametric representation of mean values for stationary random mosaies”. In: *Series Statistics* 15.3 (1984), pp. 437–442.

[91] J.L. Meijering. “Interface area, edge length, and number of vertices in crystal aggregates with random nucleation”. In: *Philips Res. Rep.* 8 (1953), pp. 270–290.

[92] Roger Edmund Miles. “Isotropic random simplices”. In: *Advances in Applied Probability* 3.2 (1971), pp. 353–382.

[93] A. T. M. Minhajuddin et al. “Bootstrap tests for multivariate directional alternatives”. In: *Journal of statistical planning and inference* 137.7 (2007), pp. 2302–2315.

[94] N. Misra and E. C. van der Meulen. “On estimation of the common mean of k normal populations with order restricted variances”. In: *Statistics & probability letters* 36.3 (1997), pp. 261–267.

[95] J. Møller. *Lectures on random Voronoi tessellations*. Vol. 87. Springer Science & Business Media, 2012.

[96] J. Møller. “Random tessellations in Rd”. In: *Advances in Applied Probability* (1989), pp. 37–73.

[97] J. Møller and D. Stoyan. *Stochastic Geometry and Radom Tessellations*. Tech. rep. Department of Mathematical Sciences, Aalborg University, 2007.

[98] C. Moussa, M. Bernacki, and N. Besnard R.and Bozzolo. "Statistical analysis of dislocations and dislocation boundaries from EBSD data". In: *Ultramicroscopy* 179 (2017), pp. 63–72.

[99] V. M. R Muggeo. "Estimating regression models with unknown break-points". In: *Statistics in medicine* 22.19 (2003), pp. 3055–3071.

[100] H. T. Mutlu et al. "A new computational approach test for one-way ANOVA under heteroscedasticity". In: *Communications in Statistics-Theory and Methods* 46.16 (2017), pp. 8236–8256.

[101] J. Nutting and R. G. Baker. "The microstructure of metals". In: (1965).

[102] J. Ohser and F. Mücklich. *Statistical analysis of microstructures in materials science*. Wiley, 2000.

[103] A. Okabe et al. *Spatial tessellations: concepts and applications of Voronoi diagrams*. Vol. 501. John Wiley & Sons, 2009.

[104] J. O'rourke et al. *Computational geometry in C*. Cambridge university press, 1998.

[105] C.S. Pande. "On a stochastic theory of grain growth". In: *Acta Metallurgica* 35.11 (1987), pp. 2671–2678.

[106] B. Peeters et al. "Work-hardening/softening behaviour of bcc polycrystals during changing strain paths: I. An integrated model based on substructure and texture evolution, and its prediction of the stress–strain behaviour of an IF steel during two-stage strain paths". In: *Acta Materialia* 49.9 (2001), pp. 1607–1619.

[107] M. D. Perlman. "One-sided testing problems in multivariate analysis". In: *The Annals of Mathematical Statistics* 40.2 (1969), pp. 549–567.

[108] K. Perzyński et al. "Numerical investigation of influence of the martensite volume fraction on DP steels fracture behavior on the basis of digital material representation model". In: *Metallurgical and Materials Transactions A* 45.13 (2014), pp. 5852–5865.

[109] N.J. Petch. "The cleavage strength of polycrystals". In: *Journal of the Iron and Steel Institute* 174 (1953), pp. 25–28.

[110] E. Pippel et al. "Microstructure and nanochemistry of carbide precipitates in high-speed steel S 6-5-2-5". In: *Materials Characterization* 43.1 (1999), pp. 41–55.

[111] R.L. Prentice. "A log gamma model and its maximum likelihood estimation". In: *Biometrika* 61.3 (1974), pp. 539–544.

[112] M.P. Quine and D.F. Watson. "Radial generation of n-dimensional Poisson procesess". In: *Journal of Applied Probability* (1984), pp. 548–557.

[113] R Core Team. *R: A Language and Environment for Statistical Computing*. R Foundation for Statistical Computing. Vienna, Austria, 2016. URL: https://www.R-project.org/.

[114] D. Raabe et al. *Continuum scale simulation of engineering materials: fundamentals-microstructures-process applications*. John Wiley & Sons, 2004.

[115] J.O. Ramsay and B.W. Silverman. "Principal components analysis for functional data". In: *Functional data analysis* (2005), pp. 147–172.

[116] V. Randle. "Electron backscatter diffraction: Strategies for reliable data acquisition and processing". In: *Materials characterization* 60.9 (2009), pp. 913–922.

[117] K. J.R. Rasmussen. "Full-range stress–strain curves for stainless steel alloys". In: *Journal of constructional steel research* 59.1 (2003), pp. 47–61.

[118] C. Revilla, B. López, and J.M. Rodriguez-Ibabe. "Carbide size refinement by controlling the heating rate during induction tempering in a low alloy steel". In: *Materials & Design (1980-2015)* 62 (2014), pp. 296–304.

[119] N. Rivier. "Order and disorder in packings and froths". In: *Disorder and granular media* (1993), pp. 55–102.

[120] T. Robertson and F. T. Wright. "On approximation of the level probabilities and associated distributions in order restricted inference". In: *Biometrika* 70.3 (1983), pp. 597–606.

[121] V. Robins and K. Turner. "Principal component analysis of persistent homology rank functions with case studies of spatial point patterns, sphere packing and colloids". In: *Physica D: Nonlinear Phenomena* 334 (2016), pp. 99–117.

[122] F. Roters and P. Kok. "An integrated approach on microstructure, damage and texture modelling of modern steels". In: *5th International Conference on Steels in Cars and Trucks, SCT 2017*. 2017.

[123] F. Roters et al. "DAMASK–The Düsseldorf Advanced Material Simulation Kit for modeling multi-physics crystal plasticity, thermal, and damage phenomena from the single crystal up to the component scale". In: *Computational Materials Science* 158 (2019), pp. 420–478.

[124] D. Ruppert, N. Cressie, and R. J. Carroll. "A transformation/weighting model for estimating Michaelis-Menten parameters". In: *Biometrics* (1989), pp. 637–656.

[125] J. Rychlewski. "On Hooke's law". In: *Journal of Applied Mathematics and Mechanics* 48.3 (1984), pp. 303–314.

[126] H. Sahai and A. Khurshid. "Confidence intervals for the mean of a Poisson distribution: a review". In: *Biometrical Journal* 35.7 (1993), pp. 857–867.

[127] G. Salanti and K. Ulm. "Multidimensional isotonic regression and estimation of the threshold value". In: (2001).

[128] K.G. Samuel. "Limitations of Hollomon and Ludwigson stress–strain relations in assessing the strain hardening parameters". In: *Journal of Physics D: Applied Physics* 39.1 (2005), p. 203.

[129] S. Sasabuchi. "More powerful tests for homogeneity of multivariate normal mean vectors under an order restriction". In: *Sankhyā: The Indian Journal of Statistics* (2007), pp. 700–716.

[130] L. Scheunemann et al. “Design of 3D statistically similar representative volume elements based on Minkowski functionals”. In: *Mechanics of Materials* 90 (2015), pp. 185–201.

[131] J. Schwertel and H. Stamm. “Analysis and modelling of tessellations by means of image analysis methods”. In: *Journal of Microscopy* 186.2 (1997), pp. 198–209.

[132] D. A. Scott and R. Schwab. “Introduction to Metallography”. In: *Metallography in Archaeology and Art*. Springer, 2019, pp. 1–6.

[133] M.M. Segovia-Gonzalez, F.M. Guerrero, and P. Herranz. “Explaining functional principal component analysis to actuarial science with an example on vehicle insurance”. In: *Insurance: Mathematics and Economics* 45.2 (2009), pp. 278–285.

[134] M. Shafto et al. “Modeling, simulation, information technology & processing roadmap”. In: *National Aeronautics and Space Administration* (2012).

[135] P. Shanthraj et al. “A phase field model for damage in elasto-viscoplastic materials”. In: *Computer Methods in Applied Mechanics and Engineering* 312 (2016), pp. 167–185.

[136] H. Sharma, R. M. Huizenga, and S. E. Offerman. “A fast methodology to determine the characteristics of thousands of grains using three-dimensional X-ray diffraction. I. Overlapping diffraction peaks and parameters of the experimental setup”. In: *Journal of applied crystallography* 45.4 (2012), pp. 693–704.

[137] H. Sharma, R. M. Huizenga, and S. E. Offerman. “A fast methodology to determine the characteristics of thousands of grains using three-dimensional X-ray diffraction. II. Volume, centre-of-mass position, crystallographic orientation and strain state of grains”. In: *Journal of Applied Crystallography* 45.4 (2012), pp. 705–718.

[138] N. Z. Shi. “Maximum likelihood estimation of means and variances from normal populations under simultaneous order restrictions”. In: *Journal of Multivariate Analysis* 50.2 (1994), pp. 282–293.

[139] N. Z. Shi, G. R. Hu, and Q. Cui. “An alternating iterative method and its application in statistical inference”. In: *Acta Mathematica Sinica, English Series* 24.5 (2008), pp. 843–856.

[140] N. Z. Shi and H. Jiang. “Maximum likelihood estimation of isotonic normal means with unknown variances”. In: *Journal of multivariate analysis* 64.2 (1998), pp. 183–195.

[141] M. J. Silvapulle and P. K. Sen. *Constrained statistical inference: Inequality, order and shape restrictions*. John Wiley & Sons, 2005.

[142] J. E. Smith and M. L. Jordan. “Mathematical and graphical interpretation of the log-normal law for particle size distribution analysis”. In: *Journal of Colloid Science* 19.6 (1964), pp. 549–559.

[143] J. Söderlund et al. “Lognormal size distributions in particle growth processes without coagulation”. In: *Physical review letters* 80.11 (1998), p. 2386.

[144] G. Spanos and W.T. Reynolds. “Microstructure of metals and alloys”. In: *Physical Metallurgy*. Elsevier, 2014, pp. 1073–1112.

[145] E. W. Stacy and G. A. Mihram. “Parameter estimation for a generalized gamma distribution”. In: *Technometrics* 7.3 (1965), pp. 349–358.

[146] D. Stoyan, W.S. Kendall, and J. Mecke. “Stochastic geometry and its applications. 1995”. In: *Akademie-Verlag, Berlin* (1987).

[147] M. Stylianou and N. Flournoy. “Dose finding using the biased coin up-and-down design and isotonic regression”. In: *Biometrics* 58.1 (2002), pp. 171–177.

[148] S. Swaminathan, S. Ghosh, and N.J. Pagano. “Statistically equivalent representative volume elements for unidirectional composite microstructures: Part I-Without damage”. In: *Journal of Composite Materials* 40.7 (2006), pp. 583–604.

[149] M. Tanemura. “Statistical distributions of Poisson Voronoi cells in two and three dimensions”. In: *FORMA-TOKYO-* 18.4 (2003), pp. 221–247.

[150] C. C. Tasan et al. “Strain localization and damage in dual phase steels investigated by coupled in-situ deformation experiments and crystal plasticity simulations”. In: *International Journal of Plasticity* 63 (2014), pp. 198–210.

[151] H. Telley, T. M. Liebling, and A. Mocellin. “The Laguerre model of grain growth in two dimensions I. Cellular structures viewed as dynamical Laguerre tessellations”. In: *Philosophical Magazine B* 73.3 (1996), pp. 395–408.

[152] Y. Tomota et al. “Prediction of mechanical properties of multi-phase steels based on stress-strain curves”. In: *ISIJ international* 32.3 (1992), pp. 343–349.

[153] C. Van Eeden. “Note on two methods for estimating ordered parameters of probability distributions”. In: *Proc. Kon. Nederl. Akad. Wetensch. A* 60 (1957), pp. 506–512.

[154] M .F. Vaz and M.A. Fortes. “Grain size distribution: The lognormal and the gamma distribution functions”. In: *Scripta metallurgica* 22.1 (1988), pp. 35–40.

[155] M. Vaz Jr, E. R. Hulse, and M. Tomiyama. “A Note on Parameter Identification of the AISI 304 Stainless Steel Using Micromechanical-Based Phenomenological Approaches”. In: *Materials Research* 22.4 (2019).

[156] E. Werner et al. “Properties of random polycrystalline two-phase materials”. In: (1994).

[157] B. T. West, K. B. Welch, and A. T. Galecki. *Linear mixed models: a practical guide using statistical software*. CRC Press, 2014.

[158] P. Widas. “Introduction to finite element analysis”. In: *Virginia Tech Material Science and Engineering* 4 (1997).

[159] S.S. Wu, S.Y. Chen, and D. Gan. “Effects of grain boundary carbide on the stress-strain curves of type 316 stainless steel”. In: *Materials Science and Engineering: A* 127.2 (1990), pp. L1–L5.

[160] Y. Xu et al. “Study on the nucleation and growth of M23C6 carbides in a 10% Cr martensite ferritic steel after long-term aging”. In: *Materials Characterization* 111 (2016), pp. 122–127.

[161] S. Yadegari et al. “Analysis of banded microstructures in multiphase steels assisted by transformation-induced plasticity”. In: *Computational materials science* 84 (2014), pp. 339–349.

[162] H. Yang et al. “Review on cellular automata simulations of microstructure evolution during metal forming process: Grain coarsening, recrystallization and phase transformation”. In: *Science China Technological Sciences* 54.8 (2011), pp. 2107–2118.

[163] F. Yao et al. “Shrinkage estimation for functional principal component scores with application to the population kinetics of plasma folate”. In: *Biometrics* 59.3 (2003), pp. 676–685.

[164] L. Zaninetti. “Poissonian and non-Poissonian Voronoi diagrams with application to the aggregation of molecules”. In: *Physics Letters A* 373.36 (2009), pp. 3223 – 3229. ISSN: 0375-9601. DOI: http://dx.doi.org/10.1016/j.physleta.2009.07.010. URL: http://www.sciencedirect.com/science/article/pii/S0375960109008160.

[165] P. Zhang, D. Balint, and J. Lin. “Controlled Poisson Voronoi tessellation for virtual grain structure generation: a statistical evaluation”. In: *Philosophical Magazine* 91.36 (2011), pp. 4555–4573.

[166] P. Zhang et al. “A controlled Poisson Voronoi tessellation for grain and cohesive boundary generation applied to crystal plasticity analysis”. In: *Computational Materials Science* 64 (2012), pp. 84–89.

[167] H.X. Zhu, S.M. Thorpe, and A.H. Windle. “The geometrical properties of irregular two-dimensional Voronoi tessellations”. In: *Philosophical magazine A* 81.12 (2001), pp. 2765–2783.

[168] H.X. Zhu et al. “The effects of regularity on the geometrical properties of Voronoi tessellations”. In: *Physica A: Statistical Mechanics and its Applications* 406 (2014), pp. 42–58.

[169] D. Zöllner and P. Streitenberger. “Three-dimensional normal grain growth: Monte Carlo Potts model simulation and analytical mean field theory”. In: *Scripta materialia* 54.9 (2006), pp. 1697–1702.

SUMMARY

This thesis aims at the development of physical relations between the intricate 3D features of metallic microstructures and the mechanical properties of the material. For understanding which are the microstructural determinants of the resulting mechanical behaviour of metals, a deep quantitative characterisation of the microstructure is needed. The main steps of quantitative characterisation of the microstructures are: identification of the phases distribution and their chemical composition, study of the microstructure morphology (geometrical arrangement of grains, grain boundaries, grain orientations, grain size and grain shape). An accurate description of the microstructure features enriched with physical knowledge can lead to new insight into the relation between micro and macro properties. Advanced statistical tools are used to find relations between microstructural and mechanical quantities. Eventually, results coming from the statistical modelling of this relation will lead to the design of new materials with desired properties.

The thesis is divided in two parts: "Microstructure (MIC)" and "Mechanical properties (MEC)", corresponding to the acronym of the project: "MICtoMEC: Extensive quantification of microstructure features and statistical relations with mechanical behaviour –from statistical relations to physical understanding–".
In the "MIC" part, microstructure related problems are faced with a focus mainly on the representation of the geometrical arrangement of the grains.
In Chapter 2, the most basic model used for approximating steel microstructure, the Poisson-Voronoi diagram is presented. Poisson-Voronoi diagrams have interesting mathematical properties, and they are considered a reasonably good model for single-phase metals microstructure. The effect of the scaling property of the underlying Poisson process on the distribution of the main geometrical properties of a typical Poisson-Voronoi cell is studied. Moreover, a sophisticated simulation program is used to construct a close Monte Carlo based approximation for the distributions of interest. Using this, the closest approximating distributions within the mentioned frequently used parametric classes of distributions is determined. Finally a 3D volume dataset is considered and the real volume distribution is compared to what is to be expected under the Poisson-Voronoi model.
In Chapter 3, methods to formally test whether a real steel microstructure can be approximated by a specific stochastic model are presented. More specifically, a general framework for testing the Poisson-Voronoi assumption based on images of 2D sections of real metals is proposed. Following two different approaches, according to the use or not of periodic boundary conditions, three different model tests are proposed. The first two are based on the coefficient of variation and the cumulative distribution function of the cells area. The third exploits tools from Topological Data Analysis, such as persistence landscapes.
In Chapter 4, digital representation methods are discussed. Two different approaches for virtually representing microstructures are presented. The first one uses empirical data

for recreating a Representative Volume Element of the material under study. The latter is based on the statistical generation of a virtual microstructure with "similar" geometrical and physical characteristics. Moreover, the use of more "flexible" tessellations methods, such as Multi-level Voronoi diagrams, are discussed in the context of a multi-phase microstructure representation.
The second part "MEC" is dedicated to the investigation of the relation between microstructural features and mechanical properties.
In Chapter 5, an approach to study how microstructural parameters relate to the mechanical behaviour of the material based on 2D microstructure images inspection is presented. More specifically the relation between Geometrically Necessary Dislocations and density of microstructural precipitates is studied in an isotonic regression framework. Already known physics-inspired qualitative relations between 2D microstructure characteristics and 3D mechanical properties act as the starting point of the investigation. Isotonic regression allows to take into account ordering relations and leads to more efficient and accurate results when the underlying assumptions actually hold. The statistical estimation procedure is described considering three different scenarios according to the knowledge of the variances: known variance ratio, completely unknown variances, variances under order restrictions. New likelihood ratio tests are developed in the last two cases. Both parametric and non-parametric bootstrap approaches are developed for finding the distribution of the test statistics under the null hypothesis.
In Chapter 6, a completely simulation-based approach is employed. Digital twins of different microstructures with different carbides volume fractions and different textures are generated. Multi-Level Poisson-Voronoi diagram is adopted as model. The resulting virtual microstructures are used as samples for virtual tensile tests. The stress–strain curves corresponding to the different volume fractions of carbides and different textures are studied. Two different approaches are employed for understanding how the different microstructural characteristics relate to the mechanical behaviour of the material. The first is to construct a function ad hoc using a change-points based procedure that allows to incorporate a priori knowledge on the different phases observed during a tensile test. The parameters of the resulting function will be then analysed as a function of the carbides intensity and texture in a linear mixed model context. The latter treats the data as functional data and uses functional principal component analysis to describe the variation among the functions in terms of carbide intensity and texture.

SAMENVATTING

Dit proefschrift richt zich op de ontwikkeling van fysieke relaties tussen de complexe 3D kenmerken van metalen microstructuren en de mechanische eigenschappen van het materiaal. Om te begrijpen wat de microstructurele determinanten zijn van het resulterende mechanische gedrag van metalen, is een grondige kwantitatieve karakterisering van de microstructuur nodig. De belangrijkste stappen voor de kwantitatieve karakterisering van de microstructuren zijn: identificatie van de faseverdeling en hun chemische samenstelling, studie van de microstructuurmorfologie (geometrische indeling van korrels, korrelgrenzen, korreloriëntaties, korrelgrootte en korrelvorm). Een nauwkeurige beschrijving van de kenmerken van de microstructuur verrijkt met fysieke kennis kan leiden tot nieuw inzicht in de relatie tussen micro- en macro-eigenschappen. Geavanceerde statistische tools worden hier gebruikt om de relaties tussen microstructurele en mechanische grootheden te vinden. Uiteindelijk zullen resultaten die voortkomen uit de statistische modellering van deze relatie leiden tot het ontwerp van nieuwe materialen met gewenste eigenschappen. Het proefschrift bestaat uit twee delen: " Microstructuur (MIC) " en "Mechanische eigenschappen (MEC)", overeenkomend met het project acroniem: "MICtoMEC: uitgebreide kwantificering van microstructurele kenmerken en statistische relaties met mechanisch gedrag –van statistische relaties tot fysiek begrip - ". In het "MIC" gedeelte worden met name de microstructurele problemen behandeld met een focus op de weergave van de geometrische rangschikking van de korrels.
In Hoofdstuk 2 wordt het meest basaal gebruikte model voor het benaderen van staal microstructuur, het Poisson-Voronoi diagram, gepresenteerd. Poisson-Voronoi diagrammen hebben interessante wiskundige eigenschappen en ze worden beschouwd als een redelijk goed model voor enkel-fasig metalen microstructuren. Het effect van de schalingseigenschap van het onderliggende Poisson-proces op de distributie van de belangrijkste geometrische eigenschappen van een typische Poisson-Voronoi cel wordt bestudeerd. Bovendien wordt een geavanceerd simulatieprogramma gebruikt om een nauw op Monte Carlo gebaseerde benadering te construeren voor de verdelingen van belang. Hiermee wordt de dichtstbijzijnde benaderende verdelingen binnen de genoemde veel gebruikte parametrische verdelingsklassen bepaald. Ten slotte wordt een 3D volumegegevensset bekeken en wordt de werkelijke volumeverdeling vergeleken met wat onder het Poisson-Voronoi model verwacht wordt.
In Hoofdstuk 3 worden methoden gepresenteerd om formeel te testen of een echte stalen microstructuur kan worden benaderd door een specifiek stochastisch model. Specifieker, wordt een algemeen raamwerk voorgesteld om de aanname van Poisson-Voronoi te testen op basis van afbeeldingen van 2D secties van echte metalen. Volgens twee verschillende benaderingen worden, afhankelijk van het wel of niet gebruiken van periodieke randvoorwaarden, drie verschillende modeltests voorgesteld. De eerste twee zijn gebaseerd op de variatiecoëfficiënt en de cumulatieve verdelingsfunctie van de cel oppervlakte. De derde maakt gebruik van tools uit topologische gegevensanalyse, zoals

"persistence landscape".
In Hoofdstuk 4 worden digitale representatiemethoden besproken. Er worden twee verschillende benaderingen gepresenteerd om microstructuren virtueel weer te geven. De eerste gebruikt empirische gegevens voor het recreëren van een representatief volume-element van het bestudeerde materiaal. De tweede is gebaseerd op de statistische formatie van een virtuele microstructuur met 'vergelijkbare' geometrische en fysieke kenmerken. Verder wordt het gebruik van meer 'flexibele' tesselatiekmethodes, zoals multi-level Voronoi-diagrammen, besproken in de context van een meerfasige microstructuur representatie.
Het tweede deel "MEC" is gewijd aan het onderzoek tussen de relaties van microstructurele kenmerken en mechanische eigenschappen.
In Hoofdstuk 5 wordt een benadering gepresenteerd om te bestuderen hoe microstructurele parameters zich verhouden tot het mechanische gedrag van het materiaal op basis van 2D microstructuurstructuren inspectie. In het bijzonder wordt de relatie tussen Geometrisch Noodzakelijke Dislocaties en de dichtheid van microstructurele precipitaten bestudeerd in een isotoon regressiekader. Reeds bekende fysisch geïnspireerde kwalitatieve relaties tussen 2D microstructuur kenmerken en 3D mechanische eigenschappen vormen het uitgangspunt van het onderzoek. Isotone regressie maakt het mogelijk om rekening te houden met ordeningsrelaties en leidt tot efficiëntere en nauwkeurigere resultaten wanneer de onderliggende veronderstellingen daadwerkelijk gelden. De statistische schattingsprocedure wordt beschreven aan de hand van drie verschillende scenario's volgens de kennis van de varianties: bekende variantie-ratio, volledig onbekende varianties, variaties onder orderbeperkingen. In de laatste twee gevallen zijn nieuwe kans ratio tests ontwikkeld. Er zijn zowel parametrische als niet-parametrische bootstrap-benaderingen ontwikkeld voor het vinden van de verdeling van de teststatistieken onder de nulhypothese.
In Hoofdstuk 6 wordt een volledig simulatie gebaseerde benadering gebruikt. Digitale tweelingen met verschillende micro structuren met verschillende carbidevolumefracties en verschillende texturen worden gegenereerd. Multi-Level Poisson-Voronoi diagram wordt als model aangenomen. De resulterende virtuele microstructuren worden gebruikt als monsters voor virtuele trekproeven. De spanningsrekcurven die overeenkomen met de verschillende volumefracties van carbiden en verschillende texturen worden bestudeerd. Er worden twee verschillende benaderingen gebruikt om te begrijpen hoe de verschillende microstructurele kenmerken zich verhouden tot het mechanische gedrag van het materiaal. De eerste is het ad hoc construeren van een functie met behulp van een op veranderingspunten gebaseerde procedure die het mogelijk maakt a priori kennis op te nemen over de verschillende fasen die worden waargenomen tijdens een trektest. De parameters van de resulterende functie worden vervolgens geanalyseerd als een functie van de carbidenintensiteit en textuur in de context van een lineaire gemengde model. Deze laatste behandelt de gegevens als functionele data en gebruikt functionele hoofdcomponentanalyse om de variatie tussen de functies te beschrijven in termen van carbidintensiteit en textuur.

ACKNOWLEDGEMENTS

PhD is usually compared to a journey. I totally agree.
For me, PhD was a journey of discovery. I travelled from Statistics to the fascinating world of metal microstructures, unravelling everyday something new. I learned what doing research means: the frustration and the satisfaction of achieving small milestones that can contribute to progress. Sometimes, it can be tough and you can get lost but this makes the goal even more gratifying.
For me, PhD was a journey among cultures. I travelled among different countries, meeting people coming from everywhere in the world. I learned words, habits, pros and cons, typical food of Dutch, Chinese, Australian, Persian, Indian, Croatian, Albanian, German, Greek, Spanish, Hungarian, Brazilian (and many more other) cultures. It was incredibly enriching and fun to discover the differences and the similarities of all these cultures with respect to Italian (Sicilian) culture. Sicily is famous for its cultural contaminations and I am now proud to have continued its tradition.
Finally, PhD was a journey into myself. If I look behind me, I see a young girl with a big suitcase. A big suitcase full of expectations, enthusiasm and curiosity but also of fears and worries. Not everything went as I expected, but I am grateful to have been able to do this experience.
But PhD for me was not a solo travel. I couldn't have make it without help.
Therefore, I would like first to express my gratitude to whom made this journey possible.
Thanks Geurt and Jilt. Since the moment of the interview I always felt stimulated and reassured by you. Thanks for all the support that you gave me as a student and as a person. You taught me a lot, not only about Statistics and Materials Science, but also to be more confident and to look things from different prospectives. Besides all your commitments you always had time for discussions, for a word of encouragement. I always felt my back covered. Grazie mille (milione).
Thanks to all the people from M2I, in particular to Viktoria, Lima and Maria. Thanks for the amazing support and for the network that you helped me creating.
Thanks to Tata and in particular to Piet for all the calls, all the emails. Thanks for your unlimited patience and availability.
Thanks to my defence committee for the insightful comments and suggestions that improved the final version of the thesis.
Thanks to the University of Palermo and to Ornella, my first academic guide, that kept motivating me and working with me in my other love Social Statistics. Thanks, also to Fabio, Massimo and Giovanni.
A special thanks goes also to my Australian professor Vanessa, for having introduced me to Topological Data Analysis field .
Thanks to all my colleagues (ex colleagues) of the Department of Applied Mathematics.
Thanks to Alessandra, Jacob, Richard, Joris, Juan, Annoesjka, Caroline, Rik, Nestor, Frank, Wioletta, Pasquale, Dorota, Cor, Ludolf, Tina, Gioia, Moritz, Carl, Stephanie, Cecilia,

Dorotee, Cindy, Evelyn.
Thanks to all my fellow PhDs.
Thanks to Jasper (for all my no coffee mornings) and Birbal (for introducing me to the Indian world). To Dan and Lixue for all the nice moments and your sweetness, for all the dinners and for all the fights for who has to pay the bill.
To Larisa (for all your complicity looks), Andrea (ti devo ancora un corso!), to Said, Lorinc, Sebastiano, Inoni and Mark. Thanks for all the nice discussions, breaks and support.
Thanks to Fede (per tutte le girovagate) and Bruno, to Rik, Bart (for all the interesting cultural discussions), Mario, Simone (per la tua educazione e simpatia), Kailun and Leandro. I promise no more obsessions with the Christmas party.
Thanks to Andrea. Per tutte le lezioni su come essere un buon PhD e per tutte le volte che hai ascoltato i miei problemi di qualsiasi natura.
Thanks to Eni and Francesca. Noi tre, il trio inseparabile. Senza di voi, non so come avrei fatto. Eni, grazie. Grazie perché sin dal primo momento mi sei sempre stata vicina. Dalla prima cena durante un temporale, ai traslochi, al montaggio dei mobili durante la notte, sempre. Fra, grazie. Grazie per tutti i nostri discorsi presto la mattina. Grazie per avermi sempre ascoltato e consigliato al meglio. Per tutto l'aiuto che mi hai dato dentro e fuori accademia. Grazie per essere state le mie rocce durante questo PhD. Grazie ragazze, per tutte le risate, le avventure e i viaggi che abbiamo fatto e che faremo.
Thanks to all my colleagues (ex colleagues) of 3ME.
Thanks to Wei, my PhD twin.
Thanks to Javi. Your passion for this work inspired me. Thanks for all the help and the patient explanations about carbides and DAMASK.
Thanks also to Carola, for your advice and your kindness.
Thanks to Vivi. Your positivity, your comprehension, your connection, your personality enlightened every moment of this journey.
Thanks also to Konstantina, Behnam, Sudhee, Arthur, Chrysa, Richard, Emiliano, Aravind Babu (for the beautiful images of the microstructures) and Prisca.
Outside University thanks to Jackie for all the nice advise and for the best gift ever, Mia.
Thanks to the people that supported me besides kilometres of distance.
Thanks to my friends.
Thanks to Angela. Per tutti i *Buongiorno* la mattina, per essere sempre accanto a me e per capire ogni mio stato d'animo.
Thanks to Maria Chiara, Antonio, Federica, Franco e Anna, perché nonostante la distanza è sempre bello ritrovarsi in Olanda, in Sicilia o a Milano.
Thanks to my family.
Grazie a Maria Elena, per tutte le volte che mi sei venuta a trovare e per tutte le discussioni serie e meno serie. Grazie alla nonna. Grazie per aver comprato uno smartphone, per essere diventata un'esperta di video chiamate e per tutte le cose buone che mi prepari ogni volta che torno a casa.
Grazie a Mamma, Papà e Piè. Grazie per avermi concesso di seguire la mia ambizione. Grazie per avermi supportato (sopportato) e incoraggiato, anche a discapito dei vostri sentimenti. Grazie per tutti viaggi, per tutto l'amore.
Finally thanks to Zyl. Thanks for teaching me yoga, for always pushing me to strive for the best, to remember me of being compassionate and lovely towards me and the others.

Thanks for all your curiosity and for patiently listening to my PhD problems. Thanks for being always next to me. Namaste.

Grazie mille a tutti!

CURRICULUM VITÆ

Martina VITTORIETTI

21-05-1992 Born in Palermo, Italy.

EDUCATION

2010–2013 Bachelor of Science in Statistics (*cum laude*)
Università degli Studi di Palermo, Palermo, Italy

2013–2016 Master of Science in Statistics (*cum laude*)
Università degli Studi di Palermo, Palermo, Italy

2014–2015 Erasmus Project
Ludwig-Maximilians Universität, Munich, Germany

2016–2020 Ph.D in Statistics
Delft University of Technology, Delft, The Netherlands
Thesis: Statistical Analysis of the Relation between Metallic Microstructures and Mechanical Properties
Promotor: Prof. dr. ir. G. Jongbloed
Promotor: Prof. dr. ir. J. Sietsma

LIST OF PUBLICATIONS

5. Hidalgo, J., Vittorietti, M., Farahani, H., Vercruysse F. , Petrova R. & Sietsma, J. (2020). Influence of large M23C6 carbides on the heterogeneous strain development in annealed 420 stainless steel.(*submitted*).

4. Vittorietti, M., Hidalgo, J., Sietsma, J., Li, W., & Jongbloed, G. (2020). Isotonic regression for metallic microstructure data: estimation and testing under order restrictions. (*submitted*)

3. Li, W., Vittorietti, M., Jongbloed, G., & Sietsma, J. (2020). The combined influence of grain size distribution and dislocation density on hardness of interstitial free steel. *Journal of Materials Science & Technology*, 45, 35-43.

2. Vittorietti, M., Kok, P. J., Sietsma, J., Li, W., & Jongbloed, G. (2020). General framework for testing Poisson-Voronoi assumption for real microstructures. *Appl Stochastic Models Bus Ind*, 1–24.

1. Vittorietti, M., Kok, P. J., Sietsma, J., & Jongbloed, G. (2019). Accurate representation of the distributions of the 3D Poisson-Voronoi typical cell geometrical features. *Computational Materials Science*, 166, 111-118.